

## Cosmicflows 4: The Calibration of Optical and Infrared Tully-Fisher Relations

EHSAN KOURKCHI,<sup>1</sup> R. BRENT TULLY,<sup>1</sup> GAGANDEEP S. ANAND,<sup>1</sup> HÉLÈNE M. COURTOIS,<sup>2</sup>  
 ALEXANDRA DUPUY,<sup>2</sup> J. DON NEILL,<sup>3</sup> LUCA RIZZI,<sup>4</sup> AND MARK SEIBERT<sup>5</sup>

<sup>1</sup>*Institute for Astronomy, University of Hawaii, 2680 Woodlawn Drive, Honolulu, HI 96822, USA*

<sup>2</sup>*University of Lyon, UCB Lyon 1, CNRS/IN2P3, IUF, IP2I Lyon, France*

<sup>3</sup>*California Institute of Technology, 1200 East California Boulevard, MC 278-17, Pasadena, CA 91125, USA*

<sup>4</sup>*W.M. Keck Observatory, 65-1120 Mamalahoa Highway, Kamuela, HI 96743, USA*

<sup>5</sup>*The Observatories of the Carnegie Institute of Washington, 813 Santa Barbara Street, Pasadena, CA 91101, USA*

Submitted to ApJ

### ABSTRACT

This study is a part of the *Cosmicflows-4* project with the aim of measuring distances of more than  $\sim 10,000$  spiral galaxies in the local universe up to  $\sim 15,000$  km s<sup>-1</sup>. New H I linewidth information has come primarily from the Arecibo Legacy Fast ALFA Survey. Photometry of our sample galaxies has been carried out in optical (*SDSS u, g, r, i, and z*) and infrared (*WISE W1 and W2*) bands. Inclinations have been determined using an online graphical interface accessible to a collaboration of citizen scientists. Galaxy distances are measured based on the correlation between the rotation rate of spirals and their absolute luminosity, known as the Tully-Fisher Relation (TFR). In this study, we present the calibration of the TFR using a sub-sample of  $\sim 600$  spirals located in 20 galaxy clusters. Correlations among such observables as color, surface brightness, and relative H I content are explored in attempts to reduce the scatter about the TFR with the goal of obtaining more accurate distances. A preliminary determination of the Hubble Constant from the distances and velocities of the calibrator clusters is  $H_0 = 76.0 \pm 1.1(\text{stat.}) \pm 2.3(\text{sys.})$  km s<sup>-1</sup> Mpc<sup>-1</sup>.

*Keywords:* galaxies: ISM – galaxies: spiral – galaxies: photometry

### 1. INTRODUCTION

Through the *Cosmicflows* program, the dark matter distribution in the Universe is reconstructed based on the peculiar motions of galaxies in response to the underlying gravitational

field. The peculiar velocities of galaxies are calculated by subtracting the Hubble expansion rate at their position from their observed radial velocities. Therefore, the precise measurement of distances is vital in this analysis.

To date, three editions of *Cosmicflows* have been published (Tully et al. 2008, 2013, 2016). Throughout, the samples are heterogeneous in that there is input involving multiple method-

ologies and multiple sources. The scale foundations are set by the Cepheid Period–Luminosity Relation (Leavitt & Pickering 1912) and Tip of the Red Giant Branch standard candle (Lee et al. 1993) supplemented by methods that have high precision but limited applicability such as Detached Eclipsing Binaries (Pietrzynski et al. 2019) and the nuclear maser in NGC 4258 (Humphreys et al. 2013). These local calibrators constrain the scaling of methods useful at intermediate distances such as the amplitudes of Surface Brightness Fluctuations in galaxies of early-type (Tonry & Schneider 1988), the three-parameter Fundamental Plane correlation also applicable to early types (Djorgovski & Davis 1987; Dressler et al. 1987), and the luminosity–rotation rate relation found to hold for spiral galaxies (Tully & Fisher 1977). All these procedures must be shown to be consistent with each other and, in turn, with the methodology that extends to large distances founded on the predictability of the peak luminosities of supernovae of Type Ia (Phillips 1993).

*Cosmicflows-3* (CF3), the last edition reporting galaxy distances, contains information on 17,647 systems<sup>1</sup>. Roughly half the contributions in that compilation come from a single source: Fundamental Plane measures from the Six Degree Field Redshift Survey (Magoulas et al. 2012; Springob et al. 2014). This contribution is restricted to  $\delta \leq 0$ , the celestial south. As a consequence, the coverage in *Cosmicflows-3* is strongly tilted toward the south. It is a particular concern of the next addition, *Cosmicflows-4*, that this imbalance in sky coverage be redressed. This new edition will contain updates across a broad spectrum of inputs but, most of all, there will be a major enhancement in the number of spiral luminosity–rotation rate measures made avail-

able as a consequence of the large number of neutral Hydrogen line profile detections resulting from the Arecibo Legacy Fast ALFA Survey (Haynes et al. 2018) covering the declination range  $0 < \delta < +38$ . Photometry for these galaxies is available from alternatively the Sloan Digital Sky Survey (Alam et al. 2015) and the Wide-field Infrared Satellite Explorer (Wright et al. 2010). The present paper presents up-to-date calibrations of the luminosity–rotation rate correlations in the bands of these surveys.

Since its inception (Tully & Fisher 1977; Aaronson et al. 1979), the luminosity–rotation rate relation (hereafter TFR) has been refined and re-evaluated by many users. If the interest is in galaxy distances, a primary concern is the control of bias (Willick 1994). The current analysis makes use of the correlation fit with errors taken in linewidths, a procedure that has been called the “inverse” TFR (ITFR). This procedure was initially discussed as a general principle by Schechter (1980) and specifically with relevance to the TFR by Tully (1988). The issue was discussed in detail in §3 of Tully & Pierce (2000). The slope of the power law fit of the ITRFR nulls bias to a first approximation. Residual bias can be taken into account with a small correction to be discussed.

It deserves emphasis that focus on the correlation with errors taken in linewidth, the distance independent parameter, is desired if the primary goal is the measurement of distances but it is not the appropriate procedure if the interest is a physical understanding of the relationship between luminosity and rotation in spiral galaxies. In the latter case, it is more informative to make a bi-variate fit taking into account errors affecting both linewidths and magnitudes (Giovanelli et al. 1997; Masters et al. 2006; Ponomareva et al. 2017; Lelli et al. 2019).

We employ the inverse relation since our interest is the measurement of galaxy distances. Re-calibrations have been carried out in both

<sup>1</sup> The CF3 catalog updated with minor corrections is available at <http://edd.ifa.hawaii.edu>

optical and infrared bands in the course of the *Cosmicflows* program. [Tully & Courtois \(2012\)](#) calibrated the TFR at  $I$ -band using 267 spirals in 13 clusters. [Aaronson et al. \(1979\)](#) suggested the use of near-infrared bands to improve the TFR methodology, given the lesser dust obscuration in host galaxies. Furthermore, the light of old stars peaks at longer wavebands and therefore near-infrared luminosities may better represent the baryonic mass of galaxies. With such motivation of reducing the scatter about the TFR and to get more accurate distances [Sorce et al. \(2013\)](#) extended the calibration of the TFR toward the infrared using *Spitzer* 3.6  $\mu\text{m}$  *Infrared Array Camera* (IRAC) imaging for the same sample of galaxies. Using the available  $I$ -band magnitudes, they also observed a correlation between the optical-infrared color index and the deviation of galaxy magnitudes from the infrared TFR. They found a tighter TFR after adjusting [3.6] magnitudes for the effect of a  $I - [3.6]$  color term.

[Neill et al. \(2014\)](#) followed the same procedure using the *Wide-field Infrared Survey Explorer* (WISE, [Wright et al. \(2010\)](#)) and added 43 galaxies to the previous sample. They also updated the calibration of the  $I$ -band TFR using their larger sample. They studied the possibility of decreasing the scatter about the infrared TFR by taking into account the optical-infrared color terms. Moreover, they showed that adopting a quadratic form for the TFR results in slightly smaller scatter about the relation.

In our program, we have performed the multi-band photometry of  $\sim 20,000$  *Cosmicflows-4* candidate galaxies in optical (*SDSS*  $u, g, r, i$  and  $z$ ) and/or infrared *WISE*  $W1$  (3.4 $\mu\text{m}$ ) and  $W2$  (4.6 $\mu\text{m}$ ) bands. The purpose of the current study is to provide the calibration of the TFR at these wavebands to measure distances for our full sample of galaxies. To achieve our goal, we use a sample of 648 calibrator galax-

ies (roughly double that available previously) in 20 clusters (up from 13). We explore intrinsic relations between color, morphology, and other galaxy observables with deviations from the TFR at different wavebands, toward possible ways to reduce scatter and hopefully obtain more accurate distances.

We explain our sample selection criteria and present our data product in §2. In §3, we calibrate the luminosity-linewidth correlations. In §4, we explore the possibility of reducing the scatter of the calibrated relations using additional observables such as color indices, and surface brightnesses. The radial velocity of the calibrator clusters are determined in §5, and their measured distance moduli are evaluated across all passbands and calibrations in §6. We provide estimations of the Hubble constant,  $H_0$ , on the basis of the clusters in §7. Our conclusion is presented in §8.

## 2. DATA

### 2.1. *Calibrators*

To calibrate the luminosity-linewidth correlation in spirals, we follow the same methodology that was originally described by [Tully & Courtois \(2012\)](#) and further implemented by [Sorce et al. \(2013\)](#) and [Neill et al. \(2014\)](#). In this technique, the TFR calibration is carried out using spirals that reside in galaxy clusters. In a cluster, all spirals are assumed to be at the same distance and therefore the correlation of apparent luminosities with rotation rates is manifested. Weighted least squares fits assume errors in linewidths (ITFR). Considering individual clusters separately, slopes are similar but intercepts differ because clusters are at different distances. Upon deriving the TFR slopes for all individual clusters, the initial step toward a universal template is taken by shifting the galaxies of each cluster along the luminosity axis to a fiducial distance (for convenience, that set by the Virgo Cluster sample; the nearest case

and populated across the fully useful magnitude range). In this first pass, the shift for a cluster is given by the magnitude difference with respect to the fiducial at the intercept magnitude value at log linewidth equal 2.5. The tentative universal template that has been formed, treating all of the galaxies as if belonging to the same cluster and at the same distance, has a more complete magnitude coverage and reduces the uncertainty of the calibration slope. The tentative universal slope is now forced in a least squares sense onto all the individual clusters. The intercept magnitude differentials with respect to the fiducial mandate the shifts to form a new universal relation. The procedure is repeated iteratively, rapidly reaching convergence.

It is to be remarked that the universal template that is constructed is decoupled from variations in the cosmic expansion. More typically in other studies, templates are formed by assuming the constituents on average participate in the Hubble flow (Willick et al. 1996; Giovanelli et al. 1997; Springob et al. 2007, 2014). We endeavor at every step to decouple the measurement of distances from velocity information since a principal goal of our program is to identify departures from Hubble expansion.

To calibrate the zero point of the TFR, we use a subset of nearby spirals with accurate distance measurements from independent methods, such as Tip of the Red Giant Branch and/or the Cepheid Period-Luminosity Relation. In case of availability of distance measurements from both methods, we use the average value. Details are provided in §3.2. The key point to mention is that the slope applied to the zero point sample is accepted to be given by the universal cluster calibration. There is no sense of completion to any magnitude limit with the zero point calibration sample. The error-weighted least squares fit to the zero point sample transforms the universal cluster template relation to an absolute magnitude scale.

The calibrator sample of this study is a subset of our large sample of  $\sim 20,000$  candidates that we compiled to measure distances using the luminosity-linewidth method<sup>2</sup>. Galaxies of this sample are restricted to (1) have high quality H I measurements (see §2.2) (2) the morphological type Sa or later (3) spirals with inclinations greater than  $45^\circ$  from face-on.

In this program, we measured the spiral inclinations by visually comparing them with a set of spirals with known inclinations. Sorting spirals based on their inclinations was executed through an online graphical tool, *Galaxy Inclination Zoo (GIZ)*<sup>3</sup>, as a participative science project with citizens. Comparisons with inclinations derived from axial ratios (Neill et al. 2014) indicate rms uncertainties are  $\pm 4^\circ$ . In detail, uncertainties are  $\pm 3^\circ$  more edge-on than  $70^\circ$ , degrading to  $\pm 5^\circ$  by inclinations of  $50^\circ$ . Please refer to §2.5 of Kourkchi et al. (2019) (hereafter K19) for further details.

We take note that inclinations can be determined in an independent way from the projection of disk rotation with resolved velocity field information. The number of sources that have been given sufficient study are limited since observations must be made with radio interferometers. The targets must be large and H I rich and warrant the investment of resources. Nonetheless, studies that have been done provide the basis for a comparison. We draw on intersecting samples of 30 galaxies by Ponomareva et al. (2017) and 97 galaxies by Lelli et al. (2016). The kinematically determined inclinations in the two interferometric studies concur and are systematically more face on than the inclinations from images by  $3.3^\circ$  with  $4\sigma$  significance. The scatter around this offset is  $\pm 4.8^\circ$ . Hence the scatter is satisfactory, suggesting statistical uncertainties at the level of  $4^\circ$  for each method,

<sup>2</sup> This catalog will be published in a separate paper.

<sup>3</sup> <http://edd.ifa.hawaii.edu/inclination/index.php>

but revealing a systematic in at least one of the methods. The information necessary to provide kinematic inclinations is not available for the samples of thousands of galaxies in our study. A systematic offset would affect our calibrators and field targets alike. We do not detect any trend in measured distances as a function of inclination.

For our calibration, we select galaxy clusters that have substantial numbers of galaxies with the requisite linewidth and photometric information (median of 24 galaxies per cluster). General properties of clusters such as center,  $R_{2t}$ ,  $V_c$  and  $\sigma_p$  are taken from a galaxy group catalog (Tully 2015) that is built based on the *Two Micron All Sky Survey* (2MASS) Redshift Survey quasi-complete to  $K_s = 11.75$  (Huchra et al. 2012), where  $R_{2t}$  is the cluster projected second turnaround radius,  $V_c$  is the average heliocentric radial velocity of cluster, and  $\sigma_p$  is the cluster projected velocity dispersion. A galaxy is included in a calibrator cluster if it meets one of the following conditions. (1) The galaxy projected distance from the center of the cluster,  $R_p$ , is less than  $1.5R_{2t}$  and its heliocentric velocity is within  $3\sigma_p$  of  $V_c$ . (2) The projected distance is relaxed to  $1.5R_{2t} \leq R_p < 3R_{2t}$  but the heliocentric velocity is more constrained at less than  $2\sigma_p$  of  $V_c$ .

Based on experience with earlier releases of *Cosmicflows*, as many as 3% of the galaxies selected for the TFR analysis do not follow the general trend of the TFR. The outlier galaxies could not be initially rejected based on their morphology or the quality of photometry and/or H I measurements and/or other observables that we use in this study. We exclude them from our sample as  $> 3\sigma$  deviants when fitting the TFR. We label these galaxies as “*anomalous galaxies*” and distinguish them in our plots.

Our selection criteria leave us with 648 galaxies (including 13 anomalous galaxies) from our

large sample as candidate members of our 20 clusters.<sup>4</sup> We use these galaxies for the slope calibration of the TFR. For the zero point calibration, there are 94 spirals that have distance measurements from the Cepheid luminosity-period or tip of red giant branch methods.

There are a few confusing regions where clusters overlap in plane-of-sky projections. For example, in the case of the Virgo Cluster we exclude galaxies that have higher chances to be members of background galaxy groups. We include a galaxy in the Virgo Cluster within its virial radius if its heliocentric velocity satisfies either  $V_h < 600 \text{ km s}^{-1}$  or  $1200 < V_h < 1600 \text{ km s}^{-1}$  to avoid galaxies that are potentially in overlapping groups: Virgo W and Virgo M at  $V_h > 1600 \text{ km s}^{-1}$  and Virgo W' and Virgo W'' in the window  $600 < V_h < 1200 \text{ km s}^{-1}$ . See Tully et al. (2016) §6.1 for an extensive discussion of the potential confusions. In another special case, the Ursa Major entity consists of 7 smaller galaxy groups identified in Kourkchi & Tully (2017) that are almost indistinguishably at the same distance along a filament that spans  $7.5^\circ$  across the plane of sky.

## 2.2. H I linewidths

One of the criteria for our sample selection is the existence of high quality H I data. We take H I 21 cm linewidths and fluxes from various sources in the order of priority listed below.

1. The All Digital H I catalog (*ADHI*) that has been compiled in the course of the *Cosmicflows* program (Courtois et al. 2009, 2011), available at the Extragalactic Distance Database (EDD) website.<sup>5</sup> Entries in this catalog contain the H I linewidth parameter  $W_{mx}$ , the parameter

<sup>4</sup> Galaxies with H I linewidths less than  $64 \text{ km s}^{-1}$  are preemptively dropped because such galaxies will not survive our final absolute magnitude cut of  $M_i \leq -17$ .

<sup>5</sup> <http://edd.ifa.hawaii.edu>; catalog “All Digital H I”.

that encodes galaxy rotation rates at their negative and positive maximum intensities along the line-of-sight.  $W_{mx}$  is calculated from the observed  $W_{m50}$ , and is adjusted for spectral resolution and redshift.  $W_{m50}$  is the linewidth at 50% of the average H I flux within the range that covers 90% of the total H I flux. Low signal to noise, confused, or anomalous line profiles are cause for the rejection of potential candidates. We only accept *ADHI*  $W_{mx}$  values if the evaluated uncertainties are less than or equal to  $20 \text{ km s}^{-1}$ .

2. The Arecibo Legacy Fast ALFA Survey (*ALFALFA*; Haynes et al. 2011, 2018). To be compatible with the *ADHI* values, cataloged *ALFALFA* linewidths are adjusted using  $W_{mx} = W_{alf} - 6 \text{ km s}^{-1}$ , a formula derived for spirals with H I linewidth measurements in both catalogs. We require  $S/N > 10$  for linewidths taken from the *ALFALFA*, which is fairly consistent with the adopted uncertainty condition for an *ADHI* estimate.
3. The *Springob/Cornell* H I catalog (Springob et al. 2005). The  $W_{M50}$  values provided in this catalog are transformed using  $W_{m50} - W_{M50} = 1.015W_{m50} - 11 \text{ km s}^{-1}$  and are then translated into  $W_{mx}$  values using the *ADHI* standard formalism (Courtois et al. 2009).
4. The *Pre Digital H I* catalog available in EDD provides information from early analog H I line profiles (Fisher & Tully 1981; Huchtmeier & Richter 1989). Recourse to this old material is needed in some cases of nearby galaxies that are much larger than the beam-sizes of large radio telescopes. This catalog lists  $W_{20}$ , the width at 20% of the H I profile peak. We convert  $W_{20}$  to  $W_{mx}$  based on the relation described by Courtois et al. (2009).

The parameter  $W_{mx}$  is taken as a robust measure of galaxy rotation after correction for the effect of inclination. We introduce a minimum threshold for our potential candidates at  $W_{mx} > 64 \text{ km s}^{-1}$ , eliminating dwarf galaxies that, at any rate, would not survive our restriction later imposed of  $M_i < -17$ . Input from the *Springob/Cornell* and *Pre Digital H I* catalogs is not considered if a galaxy has high quality H I measurements in either of the catalogs *ADHI* (uncertainty of  $W_{mx}$  not larger than  $20 \text{ km s}^{-1}$ ) or *ALFALFA* ( $S/N > 10$ ).

We take the average values of H I flux/linewidth for galaxies that are in both *ADHI* and *ALFALFA* catalogs. If a galaxy is not tabulated in either of *ADHI* or *ALFALFA* catalogs, we extract H I measurements from either *Springob/Cornell* or *Pre Digital H I* catalogs, with *Springob/Cornell* having higher priority.

Considerable attention has been given in the past to studies of the resolved rotation characteristics of spirals toward the twin quests of reducing scatter in the TFR and gaining physical insight into causes of intrinsic scatter (Verheijen 2001; Noordermeer & Verheijen 2007; Ponomareva et al. 2016, 2017; Lelli et al. 2016, 2019). These interferometric studies identify three classes: rotation curves that fall below their maximum rate at large radii, rotation curves that roughly maintain their maximum rates at large radii, and rotation curves that are continuing to rise at large radii. Massive and relatively early types tend to manifest themselves in the first of these classes while galaxies of low intrinsic luminosity are found in the third class. Scatter in the TFR is minimized by characterizing rotation with the parameter  $V_{flat}$ , determined by the resolved rotation rate at the extremity of a galaxy (Ponomareva et al. 2017; Lelli et al. 2019). Rotation parameters constructed from the rotation rate at interior radii, such as  $V_{2.2}$ , at the radius of 2.2 scale lengths cause deterioration of the TFR. These studies

are instructive but global profiles from single-beam radio observations integrate over the H I flux of galaxies. It is encouraging that Lelli et al. (2019) found that global profile parameters perform only slightly less well than  $V_{flat}$  and significantly better than parameters representative of rotation at inner radii. It can be gathered that much of the integrated H I flux from a galaxy arises from relatively large radii.

In addition to a linewidth, we derive an H I 21 cm magnitude,  $m_{21}$ , from the H I fluxes following

$$m_{21} = -2.5 \log F_{HI} + 17.40 , \quad (1)$$

where  $F_{HI}$  is the flux within the 21 cm line profile in the units  $\text{Jy}\cdot\text{km s}^{-1}$  (Makarov et al. 2014).

### 2.3. Photometry

Photometry for the calibrator galaxies is carried out on optical and infrared images provided by SDSS DR12 and WISE surveys. The process of obtaining individual exposures, image pre-processing, and performing photometry was described in detail in §2.2 through §2.4 of K19. Our asymptotic magnitudes are calculated within the aperture radius at the point the cumulative luminosity curve of growth flattens. For comparison, we computed total magnitudes with extrapolations assuming exponential disks following Tully et al. (1996), finding agreement with scatter 0.02 mag. Uncertainties in magnitudes are 0.05 mag, dominated by the setting of the sky background.

Out of 648 candidate calibrator galaxies, 464 spirals (8 anomalous) have *SDSS* photometry at  $u$ ,  $g$ ,  $r$ ,  $i$  and  $z$  bands. For 600 (19 anomalous) galaxies, we make use of *WISE*  $W1$  and  $W2$  band coverage. There is both optical and infrared photometry coverage for 435 galaxies.

The observed apparent magnitude at each waveband,  $m_{\lambda}^{total}$ , is adjusted using the following relation:

$$m_{\lambda}^* = m_{\lambda}^{(total)} - A_b^{\lambda} - A_k^{\lambda} - A_a^{\lambda} - A_i^{\lambda} , \quad (2)$$

where  $A_b^{\lambda}$  is the Milky Way dust extinction,  $A_k^{\lambda}$  is the correction for the redshift effect on the galaxy luminosity at each passband ( $k$ -correction), and  $A_a^{\lambda}$  is the total flux aperture correction for the photometry of the extended objects when the photometry calibration was performed using point source objects (stars). There is a full discussion of the calculation of  $A_b^{\lambda}$ ,  $A_k^{\lambda}$ , and  $A_a^{\lambda}$  in §2.5 of K19.

$A_i^{\lambda}$  is the dust attenuation within the host galaxy that depends on (1) the galaxy physical properties, modelled as a function of galaxy observables, and (2) the galaxy spatial orientation with respect to the observer (K19). At each waveband  $\lambda$ ,  $A_i^{\lambda}$  is modelled as

$$A_i^{\lambda} = \gamma_{\lambda} \mathcal{F}_{\lambda}(i) , \quad (3)$$

where  $\mathcal{F}_{\lambda}(i)$  is a function of galaxy inclination,  $i$ ,<sup>6</sup> and  $\gamma_{\lambda}$  is a third degree polynomial function of the main principal component,  $P_{1,W2}$ , that is constructed from the linear combination of galaxy observables using

$$\begin{aligned} P_{1,W2} = & 0.524(\log W_{mx}^i - 2.47)/0.18 \\ & + 0.601(C_{21W2} - 1.63)/1.15 \\ & - 0.603(\langle \mu_2 \rangle_e^{(i)} - 23.35)/1.38 , \end{aligned} \quad (4)$$

where  $W_{mx}^i$  is the H I linewidth corrected for inclination following  $W_{mx}^i = W_{mx}/\sin(i)$ ,  $C_{21W2} = m_{21} - \bar{W}2$  is a pseudo-color calculated from the difference between the H I 21 cm and  $W2$  magnitudes,  $\langle \mu_2 \rangle_e^{(i)}$  is the average surface brightness of galaxy at  $W2$ -band within the effective radius that is corrected for the geometric effect of inclination given by

$$\langle \mu_2 \rangle_e^{(i)} = \langle \mu_2 \rangle_e + 0.5 \log_{10}(a/b) , \quad (5)$$

where  $a$  and  $b$  are the semi-major and semi-minor axes of the photometry aperture. Given

<sup>6</sup> Symbol  $i$  not to be confused with the photometric passband

the effective radius of a galaxy,  $R_{\lambda e}$ , its effective surface brightness is

$$\langle \mu_\lambda \rangle_e = m_\lambda^{(total)} + 2.5 \log_{10}(2\pi R_{\lambda e}^2) . \quad (6)$$

There is a full discussion in K19 regarding the calculation of  $A_i^\lambda$ .

The above formalism for calculating the dust attenuation of host galaxies relies on the existence of the infrared photometry. However, there are 29 spirals in our sample of TFR calibrators for which we lack infrared photometry. We use a prediction algorithm to estimate their internal dust attenuation,  $A_i^\lambda$ , from their optical photometry, and their 21cm linewidths/fluxes.

In concept, given the luminosity of a galaxy at optical wavebands and some other information about its physical properties such as intrinsic size and/or morphology, one can predict the galaxy luminosity at longer wavebands. One common method is to fit the spectral energy distribution (SED) over the observed magnitudes using a set of template SEDs that represent the morphology, size and physical properties of the sample galaxies (Du et al. 2020).

In this study, we use a less complicated prediction scheme. We orchestrate a random forest algorithm together with a set of distance independent observables to predict the missing infrared information. Our prediction algorithm is trained using  $\sim 2,000$  spirals with the full optical/infrared magnitude coverage. The trained algorithm is capable of predicting  $W2$  magnitudes with the root mean squared (r.m.s.) uncertainty of  $\sim 0.2$  mag. Based on the predicted  $W2$  magnitudes, the  $1\sigma$  uncertainty of the predicted  $\gamma_\lambda$  is  $\sim 0.04$  mag for the optical bands and is smaller at longer wavelengths. Then  $\gamma_\lambda$  is multiplied by  $\mathcal{F}_\lambda$  to obtain the dust attenuation  $A_i^\lambda$ .  $\mathcal{F}_\lambda$  is a monotonic increasing function of inclination that is maximal for fully edge-on galaxies between 1.5 and 1.75 for the optical wavebands and 0.75 for  $W1$  band (K19). The overall uncertainty on our predicted  $A_i^\lambda$  values

is always not worse than  $\sim 0.07$  mag. We leave further details of this procedure for a following paper (E. Kourkchi et al., in preparation).

#### 2.4. Data catalog

The measurements and the collection of parameters use in this study are collected in Table 1 for 648 cluster galaxies and 94 zero point calibrators. Column contents are (1) Principal Galaxies Catalog (PGC) number, (2) common name, (3) the measured inclination angle of the galaxy in degrees, (4) the  $\text{H I}$  linewidth in  $\text{km s}^{-1}$ , (5) the logarithm of the inclination-corrected  $\text{H I}$  linewidth, calculated from  $W_{mx}^i = W_{mx} / \sin(i)$ , where  $i$  is the inclination angle presented in column 3, (6) the  $\text{H I}$  21 cm magnitude calculated from the  $\text{H I}$  flux,  $F_{HI}$ , using  $m_{21} = -2.5 \log F_{HI} + 17.4$ , (7-11) the *SDSS*  $u, g, r, i, z$  total raw magnitudes in the AB system, (12-13) the *WISE*  $W1$  and  $W2$  total raw magnitudes in the AB system,<sup>7</sup> (14) the  $b/a$  axial ratios of the elliptical photometry apertures used for the photometry of *SDSS* images, where  $a$  and  $b$  are the semi-major and semi-minor axes of the elliptical aperture, respectively, (15) analogous to 14 but for the photometry apertures of the *WISE* images, (16-22) the semi-major axes of apertures that enclose half the total light of galaxies at optical/infrared bands in arcmin, (23) the name of the host cluster, with the 94 zero point calibrators identified as “ZP calibrator”, and with an asterisk added to the end of cluster name if a galaxy is labeled as “anomalous”; i.e., strongly deviant for no reason that is evident, (24-30) tabulate optical/infrared magnitudes corrected for Milky Way obscuration, redshift  $k$ -correction, and aperture effects, but **not** the inclination depen-

<sup>7</sup> The uncertainty on the measured  $u$ -band magnitudes are  $\sim 0.1$  mag. The uncertainties on all other measured magnitudes are not worse than 0.05 mag, which is conservatively adopted for the purpose of error propagation in this study.

dent dust attenuation, based on the corresponding raw magnitudes listed in columns (7-13), (31-37) the dust attenuation corrections at optical/infrared band, calculated from Eq.3, (38-44) the correspondence to columns (31-37) after correcting for the effect of global dust obscuration,  $m_{\lambda}^{*} = m_{\lambda}^{(total)} - A_b^{\lambda} - A_k^{\lambda} - A_a^{\lambda} - A_i^{\lambda}$ .

**Table 1.** Data Catalog<sup>\*</sup>

PGC	Name	Inc. (deg)	$W_{max}$ (km s <sup>-1</sup> )	$\log(W_{max}^i)$	$m_{21}$ (mag)	$u$ (mag)	$g$ (mag)	$r$ (mag)	$i$ (mag)	$z$ (mag)	$W1$ (mag)	$W2$ (mag)	$(b/a)_S$ (mag)	$(b/a)_W$ (mag)	$R_{eu}$ (")	$R_{eg}$ (")	$R_{er}$ (")	$R_{ei}$ (")	$R_{ez}$ (")	$R_{eW1}$ (")	$R_{eW2}$ (")
(1)	(2)	(3)	(4)	(5)	(6)	(7)	(8)	(9)	(10)	(11)	(12)	(13)	(14)	(15)	(16)	(17)	(18)	(19)	(20)	(21)	(22)
38803	IC3033	59±5	111±1	2.112±0.023	15.811±0.076	15.89	14.93	14.55	14.34	14.91	15.21	0.46	0.53	0.36	0.35	0.33	0.33	0.31	0.38	0.49	
38943	NGC4178	75±3	249±2	2.410±0.007	12.884±0.076	12.43	11.68	11.21	10.92	10.83	11.31	11.88	0.35	0.34	1.59	1.38	1.34	1.28	1.21	1.22	
38945	IC3044	73±3	125±3	2.116±0.012	14.975±0.076	15.02	14.02	13.62	13.41	13.31	14.04	14.77	0.36	0.40	0.52	0.54	0.56	0.57	0.58	0.61	0.57
39028	NGC4192	78±3	458±2	2.671±0.005	12.724±0.076	11.57	10.49	9.77	9.36	9.13	9.38	9.98	0.24	0.36	2.76	1.96	1.82	1.77	1.71	1.39	1.40
39181	IC3066	83±3	132±8	2.123±0.025	16.958±0.076	16.70	15.38	14.84	14.57	14.44	15.14	15.79	0.33	0.33	0.22	0.25	0.25	0.26	0.26	0.29	0.29
39224	NGC4212	53±4	252±1	2.499±0.023	14.734±0.076	12.71	11.51	10.90	10.57	10.39	10.67	11.20	0.70	0.74	0.59	0.59	0.58	0.58	0.56	0.56	0.56
39246	NGC4216	84±3	511±1	2.711±0.003	13.752±0.076	12.11	10.48	9.64	9.15	8.91	9.04	9.69	0.24	0.32	1.76	1.43	1.27	1.23	1.13	1.00	1.04
39256	IC3077	58±4	58±13	1.835±0.102	18.110±0.076	15.41	14.16	13.54	13.16	13.07	13.72	14.71	0.65	0.72	0.59	0.58	0.56	0.56	0.54	0.42	0.42
39308	NGC4222	90±1	220±1	2.342±0.002	14.293±0.076	14.68	13.54	12.90	12.53	12.35	12.43	12.94	0.14	0.32	0.89	0.85	0.83	0.77	0.52	0.52	0.52
39431	IC3105	84±3	83±2	1.922±0.010	15.129±0.076	15.21	14.57	14.35	14.28	14.15	15.12	16.00	0.23	0.42	0.51	0.51	0.52	0.54	0.44	0.43	0.43
			...																		

<sup>\*</sup>The complete version of this table is available online.

Table 1. Data Catalog (continued)\*

PGC	Cluster	$\bar{u}$	$\bar{g}$	$\bar{r}$	$\bar{i}$	$\bar{z}$	$\bar{W1}$	$\bar{W2}$	$A_u^{(i)}$	$A_g^{(i)}$	$A_r^{(i)}$	$A_i^{(i)}$	$A_z^{(i)}$	$A_{W1}^{(i)}$	$A_{W2}^{(i)}$	$u^*$	$g^*$	$r^*$	$i^*$	$z^*$	$W1^*$	$W2^*$
(1)	(23)	(24)	(25)	(26)	(27)	(28)	(29)	(30)	(31)	(32)	(33)	(34)	(35)	(36)	(37)	(38)	(39)	(40)	(41)	(42)	(43)	(44)
38803	Virgo	15.75	14.83	14.48	14.29	14.27	14.91	15.21	0.24	0.16	0.11	0.09	0.07	0.01	0.00	15.51	14.67	14.37	14.20	14.20	14.90	15.21
38943	Virgo	12.30	11.59	11.14	10.87	10.79	11.31	11.88	0.62	0.45	0.34	0.29	0.24	0.03	0.01	11.68	11.14	10.80	10.58	10.55	11.28	11.87
38945	Virgo	14.87	13.90	13.54	13.35	13.26	14.03	14.76	0.43	0.27	0.19	0.16	0.12	0.00	0.00	14.44	13.63	13.35	13.19	13.14	14.03	14.76
39028	Virgo	11.42	10.38	9.69	9.30	9.09	9.37	9.97	0.80	0.57	0.43	0.34	0.25	0.04	0.01	10.62	9.81	9.26	8.96	8.84	9.33	9.96
39181	Virgo	16.56	15.28	14.77	14.52	14.40	15.14	15.79	0.79	0.53	0.39	0.32	0.26	0.02	0.01	15.77	14.75	14.38	14.20	14.14	15.12	15.78
39224	Virgo	12.57	11.40	10.82	10.51	10.35	10.66	11.19	0.23	0.15	0.11	0.07	0.04	0.01	0.00	12.34	11.25	10.71	10.44	10.31	10.65	11.19
39246	Virgo	11.97	10.37	9.57	9.10	8.87	9.03	9.69	0.81	0.45	0.29	0.13	0.00	0.01	0.01	11.16	9.92	9.28	8.97	8.87	9.02	9.68
39256	Virgo	15.24	14.04	13.46	13.10	13.03	13.72	14.72	0.28	0.20	0.15	0.13	0.11	0.01	0.01	14.96	13.84	13.31	12.97	12.92	13.71	14.71
39308	Virgo	14.54	13.44	12.83	12.48	12.31	12.43	12.94	1.64	1.26	1.02	0.88	0.75	0.05	0.02	12.90	12.18	11.81	11.60	11.56	12.38	12.92
39431	Virgo	15.07	14.46	14.28	14.22	14.11	15.11	15.99	0.74	0.47	0.32	0.26	0.21	0.01	0.00	14.33	13.99	13.96	13.96	13.90	15.10	15.99
...																						

\*The complete version of this table is available online.

### 3. CALIBRATION OF THE TFR

We follow the same inverse TFR (ITFR) fitting procedure as explained in [Tully & Courtois \(2012\)](#) to calibrate the TFR for all wavebands of interest. Accordingly, the errors and residuals in H I linewidth are taken into account in the linear least square regression. Bias errors are reduced by a factor 5 with respect to a direct TFR analysis ([Willick 1994](#)), reducing corrections required to account for bias from a serious to a minor problem. The major bias with use of the direct relation arises because at a given linewidth an intrinsically brighter galaxy drawn from above the mean relation is prone to be included in a sample while an intrinsically fainter galaxy may be lost. With the inverse relation, galaxies of a given magnitude with wider and narrower linewidths are equally likely to be included. See the discussion in §1 and in [Tully & Pierce \(2000\)](#).

In this study, the errors of the measured magnitudes at all wavebands are much smaller than uncertainties in the measured linewidths. Thus, we only use linewidth errors as the input measurement error. Although the inverse relation mitigates the Malmquist selection bias, the scatter in the sample induces a residual bias which is addressed in §3.6.

#### 3.1. *The ITFR template slope*

There is the fundamental assumption in using the luminosity–rotation rate correlation as a tool for measuring distances that galaxies in diverse environments statistically follow a common relationship. This assumption can be evaluated by giving attention to meaningfully large and varied samples. Drawing upon individual galaxy clusters has the useful feature that all candidates are supposed to be at the same distance. Samples can be constructed that are quasi-complete to apparent magnitude limits, with exclusions because of face-on orientation, or confusion, or morphological anomalies that

are expected to be randomly drawn from the mean correlation. Clusters do vary in their richness and the relative proportions of early and late type systems. It can be asked if spirals in clusters have the same properties as spirals outside of clusters. There is remarkably little evidence that there are differences in ways that affect the TFR. Plausibly, gas-rich spirals in clusters of all sorts are recent arrivals that retain their pre-entry properties. The issue deserves continual scrutiny. Our 20 clusters are wide-ranging in their properties, from dense and populous to diffuse and representative of the field. As will be shown, the 20 clusters share the commonalities of correlation slopes and scatter, supportive of the proposition of universal relations between galaxy luminosities and rotation rates.

Assuming that there is a universal TFR describable by a power law, then a key property of ITFR fits allows us to combine multiple cluster samples to form a robust template. The slope of the ITFR is independent of the depth of the magnitude limit, within statistical uncertainties. By contrast, the slope of the direct TFR becomes shallower as the magnitude limit is raised. A fit that combines errors on both axes shares the same property in a lesser fashion. This unique property of the ITFR of the decoupling of the slope from the depth of coverage allows cluster samples to be slid on top of each other with simple shifts in magnitude. Nearby clusters will sample to the faintest magnitudes of applicable interest. Distant clusters will only populate the upper part of the correlation, but do so drawing from the same slope. Of course, to be useful, each individual sample must be sufficiently numerous as to allow for an independent determination of slope to judge consistence and to merge with the ensemble with meaningful statistical uncertainty.

The algorithm to calibrate the slope of the ITFR is as follows. (1) The ITFR is fit independently to each individual cluster given the

**Table 2.** The calibrated slope and zero point of the ITFRs at different *SDSS* and *WISE* passbands.

Band	TFR	Sample	Universal Slope			Zero Point			ZP-Adjustment
			Code	Ngal	Slope	rms	Ngal	ZP	$C_{zp}$
(1)	(2)	(3)	(4)	(5)	(6)	(7)	(8)	(9)	(10)
u	$TF_u$	OP	429	$-7.03 \pm 0.17$	0.59	39	$-19.27 \pm 0.13$	0.75	$-0.08 \pm 0.30$
g	$TF_g$	OP	430	$-7.37 \pm 0.13$	0.49	39	$-20.15 \pm 0.11$	0.62	$-0.11 \pm 0.18$
r	$TF_r$	OP	430	$-7.96 \pm 0.13$	0.49	39	$-20.57 \pm 0.10$	0.59	$-0.08 \pm 0.13$
i	$TF_i$	OP	430	$-8.32 \pm 0.13$	0.49	39	$-20.80 \pm 0.10$	0.59	$-0.04 \pm 0.10$
z	$TF_z$	OP	429	$-8.46 \pm 0.13$	0.50	38	$-20.89 \pm 0.10$	0.57	$-0.08 \pm 0.11$
W1	$TF_{W1}$	IR	584	$-9.47 \pm 0.14$	0.58	64	$-20.36 \pm 0.07$	0.60	
W2	$TF_{W2}$	IR	584	$-9.66 \pm 0.15$	0.62	64	$-19.76 \pm 0.08$	0.65	$0.00 \pm 0.06$

apparent magnitudes and H I linewidths of its constituent galaxies. (2) One cluster is chosen as a reference and and other clusters are moved to nominally the same distance by shifting data along the magnitude axis based on the relative estimated zero points of the individually fitted ITFRs. (3) Adopting the shifted magnitudes, the combined data of all translated clusters and the reference cluster form a tentative universal template. (4) The slope of the fitted ITFR for the combined sample of clusters (the universal slope) is fitted individually to the separate clusters. (5) We cycle back to step (2), updating iteratively following the same process until convergence. In iterations at step (4), the newly revised universal slope is adopted, and with each cycle the individual zero points quickly settle to optimal values.

The estimated relative distances from the preliminary individual zero points confirm that Virgo, Ursa Major and Fornax are the closest clusters of our sample and therefore they have the most complete magnitude coverage. To minimize the incompleteness effect in the farther clusters, we first combine Virgo, Ursa Major and Fornax clusters following the above algorithm. We adopt Virgo, the slightly nearer and most populated cluster, as the reference cluster. The universal slope is then updated iteratively by combining farther clusters in groups that are sorted based on their preliminary estimated relative distances. From closest to farthest, these cluster sets are: (1) Centaurus, Antlia and Pegasus, (2) Hydra, Abell 262, NGC410, NGC507

and Cancer, (3) NGC80, NGC70, Abell 1367, Coma, Abell 400, (4) Abell 2634/66 and Abell 539, and (5) Abell 2151 (Hercules). These groups of clusters are added step-by-step to form our ultimate universal ensemble. In each step, the ITFR slope of the composed ensemble in the previous cycle is adopted as a fixed parameter to derive the relative distances of the remaining clusters. It is shown that this procedure works because the slope of the ITFR does not vary with the level of magnitude truncation in each cluster (Tully & Courtois 2012; Sorce et al. 2013; Neill et al. 2014). This assertion is substantiated with Fig. 1. Closer clusters to the left in the plots sample to fainter magnitudes of the ITFR.

Table 2 provides the universal slopes derived at different bands. Column (1) identifies the sequence of *SDSS* and *WISE* passbands. Column (2) gives the assigned codes for the resulting relations. Throughout the paper,  $TF_\lambda$  stands for the ITFR that is constructed based on the magnitudes given by Eq. 2 and no further corrections. Columns (3) identifies the nature of the sample; *OP* and *IR* stand for the samples with optical and infrared photometry measurements, respectively. Column (4) lists the number of galaxies that are involved in the ensemble when deriving the universal slope. Fewer galaxies with optical photometry are available than infrared because of the restricted sky coverage of *SDSS*. Column (5) records the universal slope. Column (6) provides the root mean square of magnitude deviations from the fitted ITFR av-

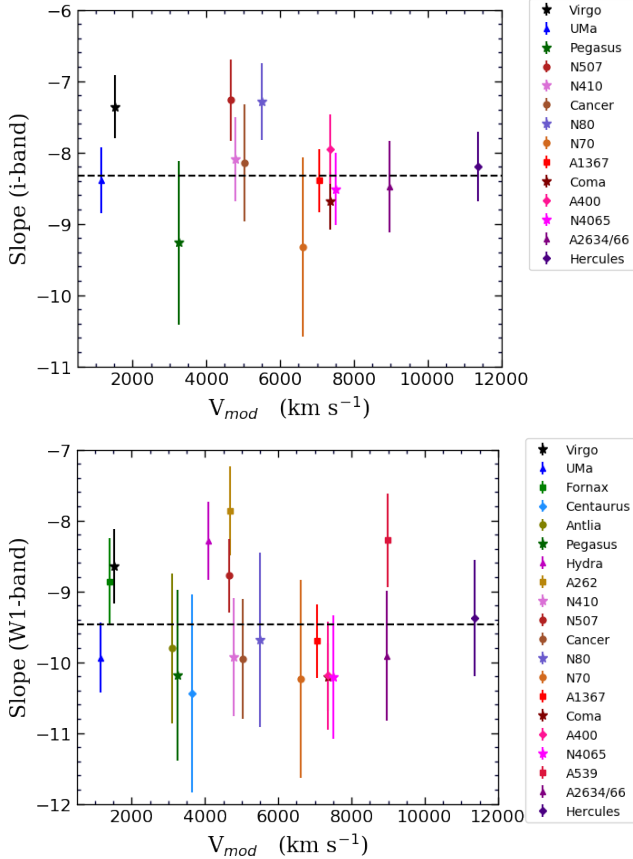


**Figure 1.** ITFR slopes with standard deviations for individual clusters vs. systemic velocity. Top panel:  $i$ -band; bottom panel:  $W1$ -band. Horizontal dashed lines are drawn at the level of the universal slopes. The legends on the right provide the clusters codes, listed in Tables 3 and 4.

eraged over the full applicable magnitude domain. In detail, scatter increases toward fainter magnitudes as discussed in §3.5. Columns (7) to (9) contain zero point information discussed in §3.2. Columns (10) lists the adjustment on the ITFR zero point discussed in §3.4.

As an example, Fig. 2 displays the apparent magnitudes versus linewidths for galaxies in the Virgo cluster at *SDSS*  $u$ ,  $g$ ,  $r$ ,  $i$ ,  $z$  and *WISE*  $W1$  and  $W2$  passbands. In each panel, the dashed line is the least square fit to the filled colored points. In the fitting process, we exclude the outlier galaxies NGC 4424 (PGC40809) and IC 3446 (PGC41440) and galaxies with absolute *SDSS*  $i$ -band magnitudes fainter than  $-17$

mag (see §3.2 regarding the absolute magnitude limit). In Fig. 2, the excluded galaxies are represented by open gray points. The universal ITFR slopes, fit with the zero point as the only free parameter, are represented by the solid lines.

There are 14 clusters in our study with optical imaging coverage (the *OP* sample). Fig. 3 illustrates the individual and universal ITFRs in  $i$ -band for these clusters. Galaxies that are considered anomalous are displayed in red and excluded from the least squares fits. The slopes of the solid lines in all panels of this figure are the same and equal to the universal slope of ITFR in  $i$ -band of  $-8.32 \pm 0.13$ . The complete information on the fitted relations are presented in Table 3.

The all sky coverage of the *WISE* imaging enables us to consider more clusters in infrared bands. One exceptional case is Abell 262 that is located at the edge of the *SDSS* survey, such that there are only 7 galaxies with *SDSS* photometry but 55 with *WISE* photometry. Fig. 4 displays ITFRs for 20 clusters studied in  $W1$ -band, and Table 4 lists the parameters of the fits.

Our resulting universal ensembles in  $i$  and  $W1$  bands are illustrated in the two panels of Fig. 5. The annotations list cluster names and the zero-point offsets relative to the Virgo Cluster. In cases of clusters with both optical and infrared coverage the magnitude offsets at  $i$  and  $W1$  bands are in reasonable agreement.

### 3.2. Zero point calibration and absolute distances

We consider 94 galaxies that have distance estimates derived from either the Cepheid Period–Luminosity Relation (CPLR) or the Tip of the Red Giant Branch (TRGB) luminosity feature. Not all of these are useful, particularly those that pertain to systems fainter than our ultimate  $M_i = 17$  cutoff, but there are many more potential zero-point calibrators than previously available. The absolute calibra-

**Table 3.** The parameters of the fitted ITFRs for individual clusters in  $i$ -band, as visualized in Fig. 3. The cluster name is listed in the first column. The cluster codes are listed in the second column. “Ngal” is the number of galaxies incorporated in the ITFR fit. “Slope” and “ZP” are the slopes and zero points of the individually fitted ITFRs (dashed lines in Fig. 3). “ZP<sub>0</sub>” is the resulting individual zero points from the linear regressions with the fixed ITFR universal slope, i.e.  $-8.32 \pm 0.13$ . The root mean square of galaxy deviations from the universal lines (solid lines in Fig. 3) along the magnitude axis are tabulated in the last column.

Cluster	Code	Ngal	Slope	ZP	ZP <sub>0</sub>	rms
Virgo	V	24	-7.36 $\pm$ 0.44	10.13 $\pm$ 0.09	10.03 $\pm$ 0.09	0.69
Ursa Major	U Ma	36	-8.39 $\pm$ 0.46	10.43 $\pm$ 0.08	10.43 $\pm$ 0.07	0.53
Pegasus	Pe	24	-9.27 $\pm$ 1.15	12.24 $\pm$ 0.23	12.40 $\pm$ 0.11	0.59
NGC507	N5	20	-7.27 $\pm$ 0.57	13.06 $\pm$ 0.10	13.06 $\pm$ 0.12	0.54
NGC410	N41	33	-8.10 $\pm$ 0.58	13.15 $\pm$ 0.08	13.14 $\pm$ 0.08	0.52
Cancer	Ca	18	-8.15 $\pm$ 0.82	13.29 $\pm$ 0.11	13.29 $\pm$ 0.11	0.48
NGC80	N8	14	-7.29 $\pm$ 0.54	13.71 $\pm$ 0.06	13.69 $\pm$ 0.07	0.41
NGC70	N7	11	-9.32 $\pm$ 1.26	13.78 $\pm$ 0.15	13.71 $\pm$ 0.10	0.35
Abell 1367	A1	68	-8.40 $\pm$ 0.44	13.91 $\pm$ 0.06	13.91 $\pm$ 0.06	0.56
Coma	Co	79	-8.68 $\pm$ 0.40	13.94 $\pm$ 0.06	13.95 $\pm$ 0.06	0.56
Abell 400	A4	21	-7.95 $\pm$ 0.48	13.99 $\pm$ 0.06	14.00 $\pm$ 0.06	0.58
NGC4065	N40	14	-8.51 $\pm$ 0.50	14.25 $\pm$ 0.09	14.26 $\pm$ 0.08	0.40
Abell 2634/66	A2	29	-8.48 $\pm$ 0.64	14.43 $\pm$ 0.09	14.42 $\pm$ 0.06	0.48
Hercules	He	39	-8.20 $\pm$ 0.49	15.06 $\pm$ 0.07	15.07 $\pm$ 0.06	0.42

**Table 4.** Same as Table 3 but for the parameters of the fitted ITFRs for individual clusters in  $W1$ -band, as visualized in Fig. 4. The universal slope at  $W1$ -band is  $9.47 \pm 0.14$ .

Cluster	Code	Ngal	Slope	ZP	ZP <sub>0</sub>	rms
Virgo	V	24	-8.64 $\pm$ 0.53	10.53 $\pm$ 0.11	10.44 $\pm$ 0.10	0.82
Ursa Major	U Ma	36	-9.94 $\pm$ 0.49	10.77 $\pm$ 0.08	10.80 $\pm$ 0.08	0.59
Fornax	F	17	-8.86 $\pm$ 0.61	10.88 $\pm$ 0.13	10.86 $\pm$ 0.14	0.78
Centaurus	Ce	22	-10.44 $\pm$ 1.27	12.27 $\pm$ 0.15	12.28 $\pm$ 0.13	0.59
Antlia	An	17	-9.80 $\pm$ 1.05	12.43 $\pm$ 0.12	12.42 $\pm$ 0.11	0.61
Pegasus	Pe	23	-10.19 $\pm$ 1.21	12.70 $\pm$ 0.24	12.81 $\pm$ 0.12	0.66
Hydra	Hy	44	-8.19 $\pm$ 0.55	13.25 $\pm$ 0.09	13.29 $\pm$ 0.10	0.89
Abell 262	A26	54	-7.86 $\pm$ 0.63	13.47 $\pm$ 0.11	13.49 $\pm$ 0.13	0.98
NGC410	N41	31	-9.93 $\pm$ 0.83	13.60 $\pm$ 0.11	13.61 $\pm$ 0.10	0.64
NGC507	N5	22	-8.78 $\pm$ 0.52	13.61 $\pm$ 0.08	13.64 $\pm$ 0.08	0.38
Cancer	Ca	17	-9.95 $\pm$ 0.84	13.80 $\pm$ 0.12	13.79 $\pm$ 0.11	0.51
NGC80	N8	13	-9.68 $\pm$ 1.23	14.09 $\pm$ 0.13	14.09 $\pm$ 0.12	0.53
NGC70	N7	11	-10.23 $\pm$ 1.40	14.22 $\pm$ 0.16	14.17 $\pm$ 0.12	0.42
Abell 1367	A1	62	-9.70 $\pm$ 0.52	14.49 $\pm$ 0.06	14.49 $\pm$ 0.06	0.59
Coma	Co	75	-10.21 $\pm$ 0.48	14.49 $\pm$ 0.07	14.50 $\pm$ 0.06	0.61
Abell 400	A4	23	-10.19 $\pm$ 0.76	14.55 $\pm$ 0.09	14.54 $\pm$ 0.08	0.69
NGC4065	N40	12	-10.21 $\pm$ 0.87	14.68 $\pm$ 0.12	14.71 $\pm$ 0.11	0.53
Abell 539	A5	22	-8.28 $\pm$ 0.66	14.77 $\pm$ 0.08	14.86 $\pm$ 0.08	0.39
Abell 2634/66	A2	26	-9.91 $\pm$ 0.92	14.97 $\pm$ 0.12	14.93 $\pm$ 0.08	0.57
Hercules	He	33	-9.38 $\pm$ 0.82	15.68 $\pm$ 0.12	15.68 $\pm$ 0.09	0.52

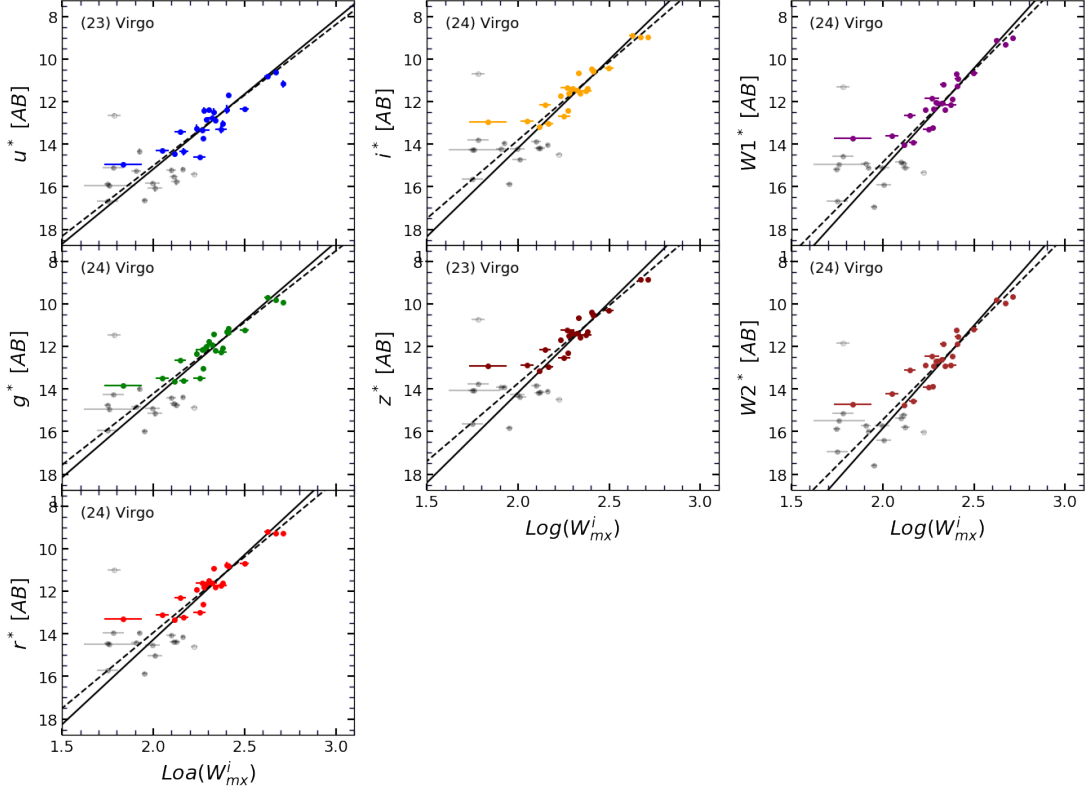


**Figure 2.** The ITFR fit for the Virgo cluster galaxies at different optical and infrared bands. Dashed line illustrates the fitted ITFR using the filled colored points, and the solid line is the fitted ITFR using the universal slope as a fixed parameter. Gray open points represent galaxies that either are outliers or their absolute *SDSS* -magnitudes, after the full calibration, are fainter than  $M_i = -17$  mag.

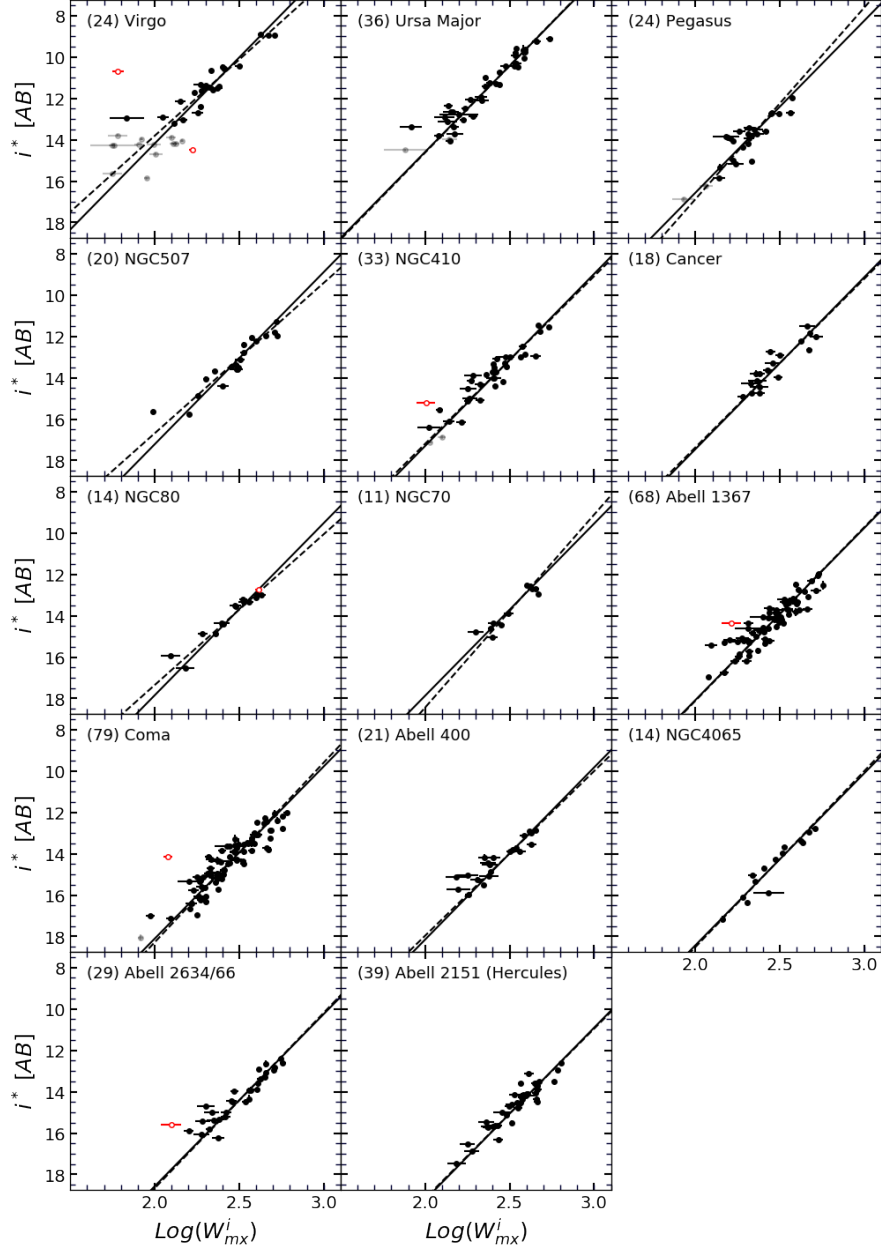


**Figure 3.** ITFR fits for 14 clusters with available *SDSS* *i*-band photometry. In each panel, the dashed line is the fit pertaining to the individual cluster and the solid line is the best universal ITFR slope fit to the cluster. Red points identify excluded outliers. Gray points are galaxies fainter than the magnitude limit of  $M_i = -17$  mag. The number of contributing galaxies in the fitting process is displayed before the cluster name at the top left corner of each panel.

tion of *Cosmicflows-3* was based on 33 galaxies; 25 CPLR, 19 TRGB, with 11 in common. Here, as in the earlier study, the CPLR and TRGB calibration distances are founded through completely separate pathways. The two resultant

scales can be compared, evaluated, and combined as deemed appropriate.

In *Cosmicflows-3*, the CPLR calibration assumed a Large Magellanic Cloud (LMC) distance modulus of 18.50. Here we adopt a small change. Our zero point scale is set to be con-

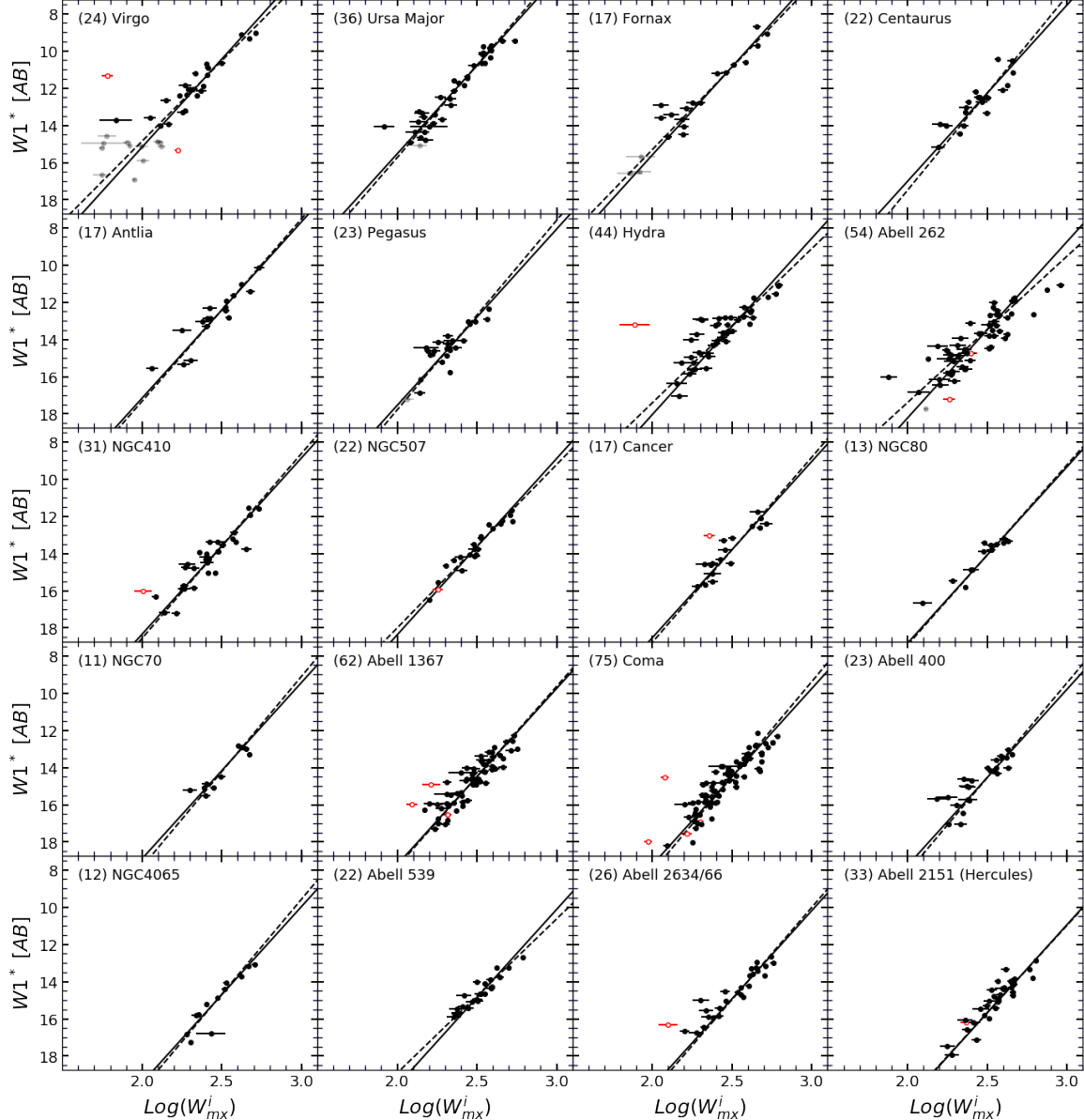


**Figure 4.** Same as Fig. 3 but for 20 clusters with available *WISE*  $W1$ -band photometry. The faint end magnitude cutoff is at  $M_{W1} = -16.1$  mag.

sistent with that of Riess et al. (2019) that combines linkages with the LMC assumed at a modulus of  $\mu_{LMC} = 18.477$  (Pietrzynski et al. 2019), the maser galaxy NGC 4258 at modulus  $\mu_{N4258} = 29.40$  (Humphreys et al. 2013), and a Milky Way based calibration. That paper argues for a small modification (a decrease in moduli of  $-0.024$  mag) of the CPLR distance moduli reported by Riess et al. (2016). In addition, three other sources of distances from the

CPLR are incorporated. Ground based observations provide measures for very nearby galaxies. We average over two sources, those by Bhardwaj et al. (2016) and by the Araucaria collaboration (Gieren et al. 2013; Zgirski et al. 2017) and related references. The two sources agree to within  $0.02$  mag ( $1\sigma$  with scatter  $\pm 0.06$  mag) and are given equal weight in averaging. Zero points tied to the LMC are re-scaled to agree with Riess et al. (2019). The other Cepheid con-

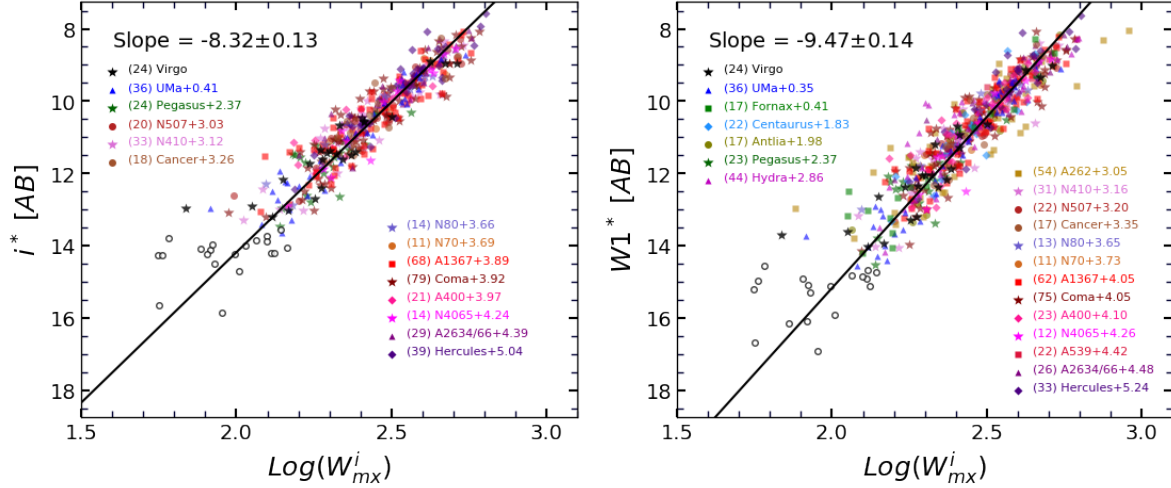


**Figure 5.** The universal template constructed from all clusters to find the slope of the ITFR. All clusters are shifted forward to the distance of the Virgo cluster by adjusting the apparent magnitude of their constituent galaxies. Galaxies in each cluster are displayed by unique symbol/color. Labels start with the number of contributed galaxies in each cluster followed by the cluster name and the magnitude offset relative to Virgo. Open circles are galaxies fainter than the faint end magnitude cutoff, i.e.  $-17$  mag at  $i$ -band and  $-16.1$  mag at  $W1$ -band.

tribution is Freedman et al. (2001). The overlap with Riess et al. (2016) is only four objects but the agreement is within 0.02 mag at the same LMC fiducial distance. Each of these inputs is re-scaled to be consistent with Riess et al. (2019).

Our primary source for TRGB distances is the CMDs/TRGB catalog in the Extragalactic Distance Database (EDD)<sup>8</sup> (Jacobs et al. 2009). The zero point in this compilation was established by Rizzi et al. (2007) based on Horizontal Branch/RR Lyrae distances to nearby dwarf spheroidals and other minor galaxies in the Local Group. The sample is expanded by the addition of three objects studied by Jang & Lee (2015, 2017).

As with the cluster samples, the zero point calibrators are subject to faint limit luminosity cuts. The cut at optical bands is set at  $i$ -band such that galaxies fainter than  $M_i = -17$  are dropped. The infrared cut is the roughly equivalent  $M_{W1} = -16.1$ . There are four galax-

ies brighter than these limits that deviate by more than  $3\sigma$  from the TFR and are considered anomalous cases and rejected: PGC5896 (NGC625), PGC44536 (NGC4861), PGC48334 (NGC5253), and PGC68535 (NGC7250). The optical bands are left with 39 calibrators: 19 CPLR, 29 TRGB, with 9 in common. There are 64 calibrators in the infrared: 29 CPLR, 52 TRGB, and 17 with both. There are fewer optical calibrators because of the restricted domain of the SDSS photometry. The WISE photometry is available across the full sky.

Zero-point calibrations are shown for the representative  $i$  and  $W1$  bands in Fig. 6. The linear fits obey the formulation

$$\mathcal{M}_\lambda^* = \text{Slope}(\log W_{mx}^i - 2.5) + ZP, \quad (7)$$

where zero-point,  $ZP$ , is the absolute luminosity of a galaxy at  $\log W_{mx}^i = 2.5$ . We adopt the convention that the ITFR predictions of absolute magnitudes are given in script. The superscript asterisks indicate that magnitudes are corrected for the effects explained following Eq. 2. In Fig. 6, the TRGB and CPLR calibrators are shown separately in the middle

<sup>8</sup> <http://edd.ifa.hawaii.edu>

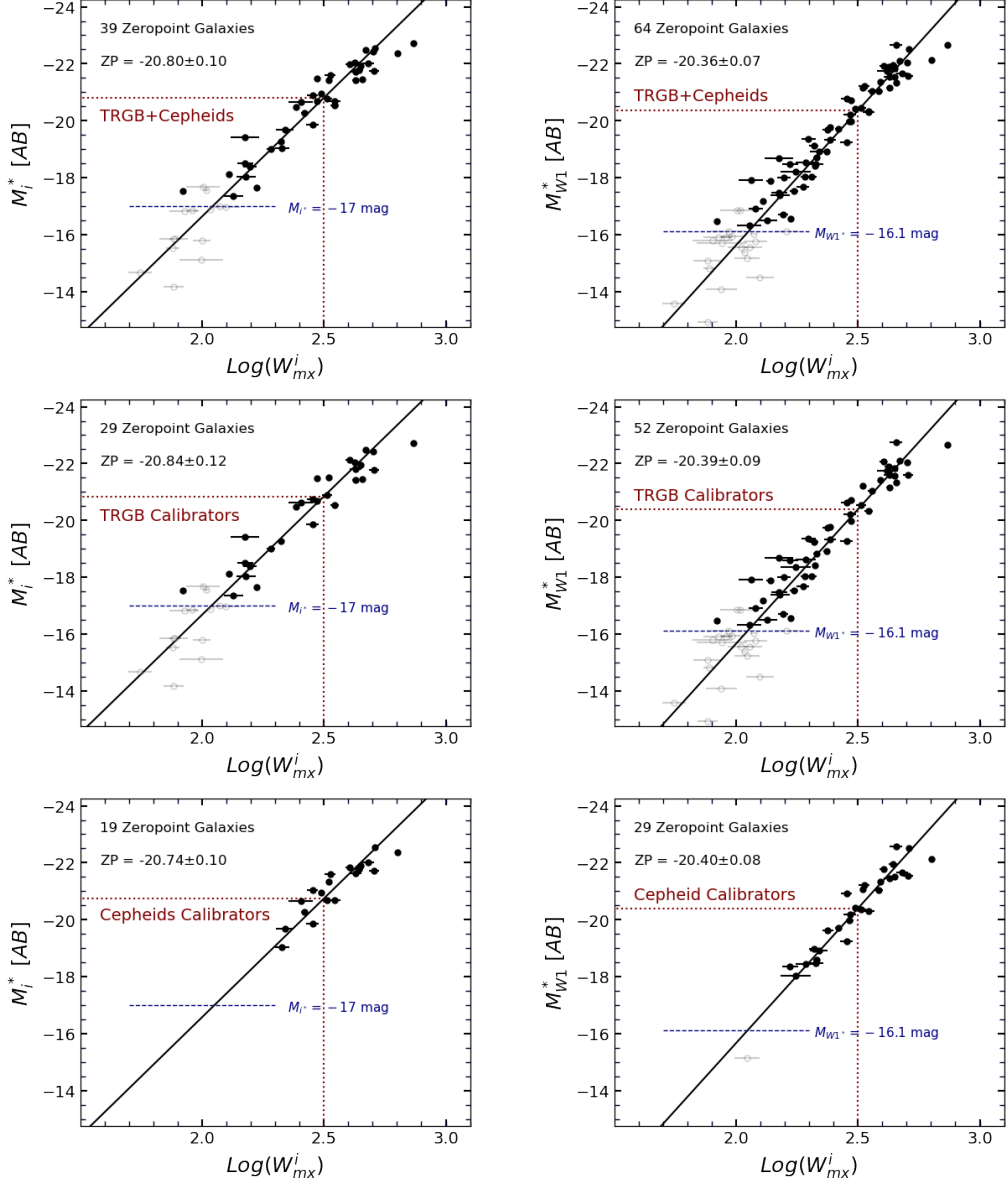


**Figure 6.** Absolute luminosity of the zero point calibrators versus H I linewidth at optical  $i$ -band (left) and infrared  $W1$ -band (right). The slopes of the solid lines are set by the cluster template. Least squares minimization of magnitudes set the zero points. Blue dashed lines mark the adopted magnitude limits. Faint and excluded zero point calibrators are displayed in gray. Maroon dotted horizontal/vertical lines mark magnitude zero points where  $\log(W^i_{mx}) = 2.5$ .

and bottom panels respectively, and the combined samples are shown in the top panels with straight averaging between TRGB and CPLR when both are available.

Slopes are set by the values determined from the cluster templates, while zero-points are established by least squares regression with the zero-point as the only free parameter. In Fig. 6

the maroon dotted lines indicate the location of the  $ZP$  on the absolute magnitude axis. In these examples,

$$\begin{aligned} \mathcal{M}_i^* = & -(20.80 \pm 0.10) \\ & -(8.32 \pm 0.13)(\log W^i_{mx} - 2.5), \end{aligned} \quad (8a)$$

$$\begin{aligned} \mathcal{M}_{W1}^* = & -(20.36 \pm 0.07) \\ & -(9.47 \pm 0.14)(\log W^i_{mx} - 2.5). \end{aligned} \quad (8b)$$

The zero-points for all wavebands are recorded in column (8) of Table 2. Column (7) of this table gives the number of zero-points calibrators used at each band and column (9) gives the root mean square scatter of calibrators about the fitted lines along the absolute luminosity axis.

The distance modulus,  $\mu_\lambda$ , of a given galaxy with the apparent magnitude  $m_\lambda^*$  is given as

$$\mu_\lambda = m_\lambda^* - \mathcal{M}_\lambda^*. \quad (9)$$

For example, the magnitude offsets between apparent magnitudes at  $\log W_{mx}^i = 2.5$  in Fig. 5 and absolute magnitudes at the same linewidth value in Fig. 6 give measures for the distance modulus of the Virgo Cluster. Moduli for the other clusters can be determined from the magnitude offsets derived in the construction of the universal clusters templates, recorded in the labelling of Fig. 5 for the cases of the  $i$  and W1 passbands.

### 3.3. Alternate Zero Point Calibration: Possible Serious Systematic

Freedman et al. (2019), hereafter F19, have recently provided a re-calibration of the TRGB zero point that has lead those authors to derive a value for the Hubble Constant  $H_0$  of  $69.8 \pm 1.9$ , significantly lower than the Riess et al. (2019) value of  $74.0 \pm 1.4$  and, anticipating the results of this study, significantly lower than we find with the calibration derived in §3.2. Given the varying degrees of tension of these values with the value of  $67.4 \pm 0.5$  derived from early universe conditions (Planck Collaboration et al. 2018) and the implications for physics beyond the standard model, we are called upon to justify why we prefer our TRGB calibration to that of F19.

We note two significant differences between the TRGB zero point calibration by F19 and our own. First, F19 base their calibration on the Large Magellanic Cloud (LMC) at a distance given by the combination of detached eclips-

ing binaries (Pietrzynski et al. 2019) and mid-infrared CPLR (Scowcroft et al. 2011; Monson et al. 2012). The LMC is too large and with the Red Giant Branch stars too bright to be easily studied with Hubble Space Telescope. F19 drew on ground based observations of the OGLE Collaboration (Ulaczyk et al. 2012) with photometry in  $V, I$  bands. Our calibration is tied to Horizontal Branch and RR Lyrae distances to the Local Group galaxies M33, IC 1613, NGC 185, Sculptor, and Fornax (Rizzi et al. 2007). The stellar photometry isolating the TRGB was with our standard filters with HST using both WF/PC2 and ACS detectors.

Second, F19 assume that the TRGB has a constant absolute magnitude of  $M_I = -4.05$  for all manner of galaxies.<sup>9</sup> The Rizzi et al. (2007) calibration that we assume incorporates a weak color dependency, in response primarily to metallicity variations and secondarily to age differences. The LMC has a relatively low metal abundance and consequently the TRGB is expected in our formulation to be somewhat brighter than is the case with most of the galaxies in the TFR zero point calibration.

These alternate procedures result in differing values for the Hubble Constant, so which better approximates reality? F19 compared their TRGB and Riess et al. (2019) CPLR distance moduli and for 10 supernova Ia systems relevant to their study they found  $\langle \mu_{TRGB} - \mu_{CPLR} \rangle = +0.06 \pm 0.17$  with  $1\sigma$  uncertainty  $\pm 0.05$ ; evidence for good agreement. We made a similar comparison of our TRGB and Riess et al. (2019) CPLR moduli with 25 galaxies and got

<sup>9</sup> Yuan et al. (2019) argue that the F19 TRGB absolute magnitude should be  $M_I = -3.97$  and the F19 calibration of  $H_0$  should be increased 3.7% to  $72.4 \text{ km s}^{-1} \text{ Mpc}^{-1}$ , primarily because, they contend, reddening is lower in the direction of the LMC fields than accepted by F19.

the disturbing difference  $\langle \mu_{TRGB} - \mu_{CPLR} \rangle = 0.13 \pm 0.10$  and  $1\sigma$  uncertainty  $\pm 0.02$ .

It could be argued that we should abandon our separate TRGB and CPLR calibrations. Instead we should force agreement averaged over instances where both measures are available. We could choose one or other of TRGB or CPLR as baseline or take some average of the two. However any such approach fails. Consider the panels of Fig. 6. Retaining the separation of TRGB and CPLR calibrations, we can reach compatible inferred  $H_0$  values for the more distant clusters in our study, as will be described culminating in §7. However, if one or other of the TRGB or CPLR scales is changed to force agreement on average between individual targets then a difference at the level of 7% is created if the zero point calibration is based solely on TRGB or on CPLR samples.

We review this unsatisfactory situation. If the F19 calibration of the TRGB is accepted then there is statistical agreement between TRGB measures and the CPLR moduli of Riess et al. (2019) but there is a disconnect between the TRGB and CPLR calibrations of the TFR that leads to inconsistent determinations of  $H_0$ . If instead the TRGB calibration of Rizzi et al. (2007) is accepted and the Riess et al. (2019) calibration of the CPLR is accepted then the TRGB and CPLR calibrations of the TFR are consistent in terms of values of  $H_0$  found using our clusters sample.

It is to be appreciated that the primary goal of the *Cosmicflows* program is to measure the peculiar velocities of galaxies, not  $H_0$ . With distances  $d_i$  we obtain peculiar velocities  $V_{pec,i} \sim cz_i - H_0 d_i$  where  $H_0 \sim \langle cz_i/d_i \rangle$ . Hence, it is important that we use a value of  $H_0$  compatible with the distance measures, not that we use the “correct”  $H_0$ . Important details of the zero point calibration remain to be resolved. The discussion in this section highlights the possibility of substantial systematics.

### 3.4. Zero point adjustments

In principle, distance moduli to a given cluster should be the same across all passbands. However, we have detected a trend in the cluster calibrator samples whereby moduli are slightly reduced at blueward bands. We trace this effect to a slight color offset between the ensemble cluster template sample and the sample with CPLR or TRGB distances that gives the zero-point calibration.

The problem is illustrated in Fig. 7. Colors with respect to the infrared band W1 are shown on the abscissa in each panel, with the clusters sample plotted as grey points and the zero-point sample in green. The ordinate positions of points are given by absolute magnitudes in the W1 band following from the calibration described in the previous sub-section. The solid black lines in these plots are fits to the clusters template sample obeying the formulation  $\lambda - W1 = m M_{W1} + b$ . The intercept  $b$  is the average  $\lambda - W1$  color of galaxies with  $M_{W1} = 0$ . The least squares minimization is carried out in the color terms to counter Malmquist-type bias.

The dashed green lines in these panels are the fits to solely the zero-point calibrators, preserving the black solid line slopes but giving freedom to the scaling parameter  $b$ . Offsets between the black and green lines are given by  $C_{zp} = b_{clusters} - b_{zp}$ . In every case between an optical bandpass and the infrared bandpass W1 the green dashed lines are offset redward of the black solid lines. Never are the offsets statistically significant. However making an adjustment for the offsets statistically eliminates the differences in distance moduli measurements as a function of passband. We make the adjustment

$$\overline{ZP} = ZP + C_{zp} . \quad (10)$$

which gives consistency with moduli determined in the W1 band. There is no assurance that reporting to the W1 band is correct. We take the amplitude of shifts at the level of 3% in dis-

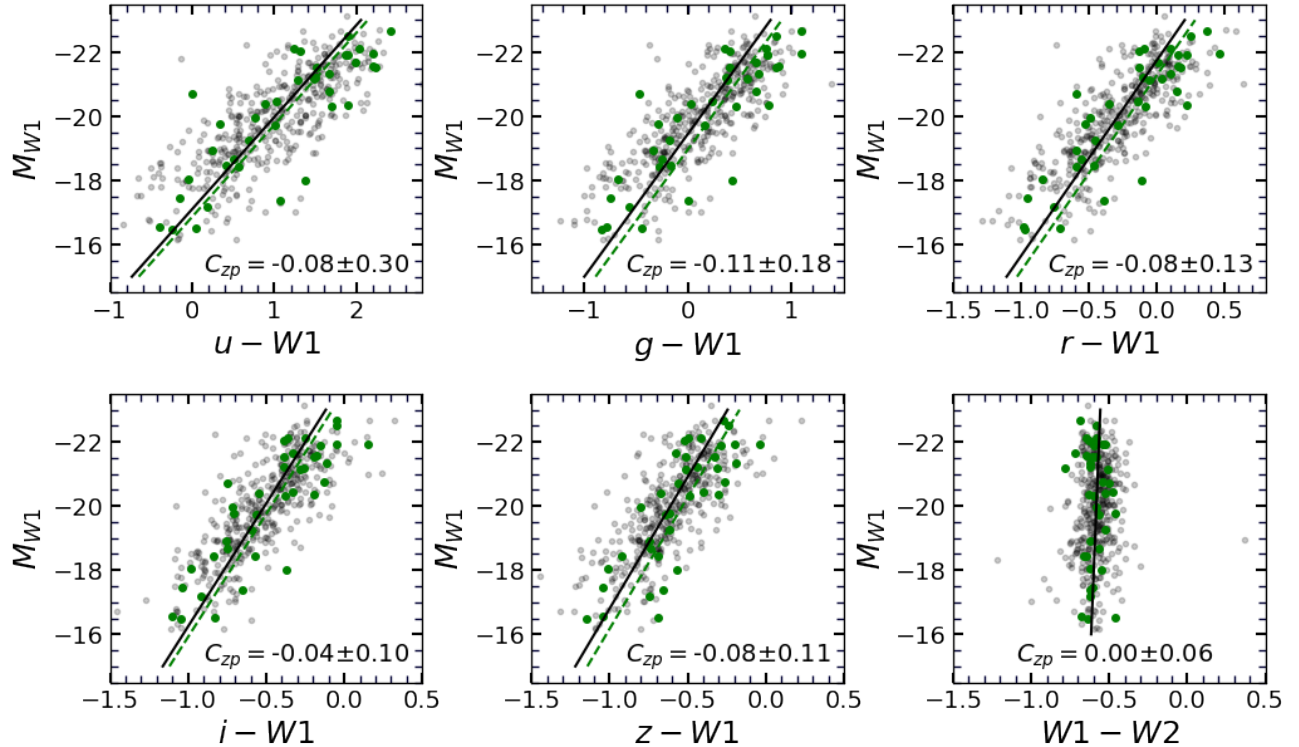


**Figure 7.** Absolute magnitudes at  $W1$ -bands versus color indices. Gray points represent cluster galaxies used for ITFR slope calibration. Green point are zero point calibrators. The fitted lines are the results of least square regression procedure that minimized the residuals along the color axis. Black solid and green dashed lines are fitted over gray and green points, respectively. The slope of the green line is the same as the black line and is fixed in the fitting process. In each panel,  $C_{zp}$  is the difference in the zero-point of the fitted lines along the horizontal axis.

tances as a quantitative estimator of systematic uncertainty.

The final linear calibrations are given in Fig. 8 for the 5 optical and two infrared bands. The points in colors represent galaxies from the clusters template brighter than our magnitude thresholds and not rejected as an outlier. The CPLR and TRGB zero-point galaxies are represented by points in black and establish the absolute magnitude scales. Information in each panel includes the numbers of contributing clusters template and zero-point galaxies, the slopes derived from the clusters template, the zero-points derived directly from the galaxies with CPLR or TRGB distances, and the adjustment parameters,  $C_{zp}$ , required to null the color offsets demonstrated in Fig. 7. Neither of the infrared band correlations receive an adjustment.

To avoid confusion, the nomenclature for the ITFR with adjusted zero-points is

$$\overline{\mathcal{M}}_{\lambda}^* = \text{Slope}(\log W_{mx}^i - 2.5) + \overline{ZP} . \quad (11)$$

### 3.5. Scatters about the ITFR

We use the root mean square (*rms*) scatter of data points about the fitted ITFRs as a measure of the statistical uncertainty of individual distance estimates. Absolute magnitude residuals from the ITFR are expressed as

$$\Delta M_{\lambda}^i = M_{\lambda}^i - \mathcal{M}_{\lambda}^* , \quad (12)$$

where  $M_{\lambda}^i$  is the absolute magnitude of a target galaxy and  $\mathcal{M}_{\lambda}^*$  is the estimated absolute magnitude at the target's linewidth from the fitted linear relation. The *rms* scatter of the ensemble of galaxies in Fig. 8 (colored clusters template sample) and zero-point calibrators (black

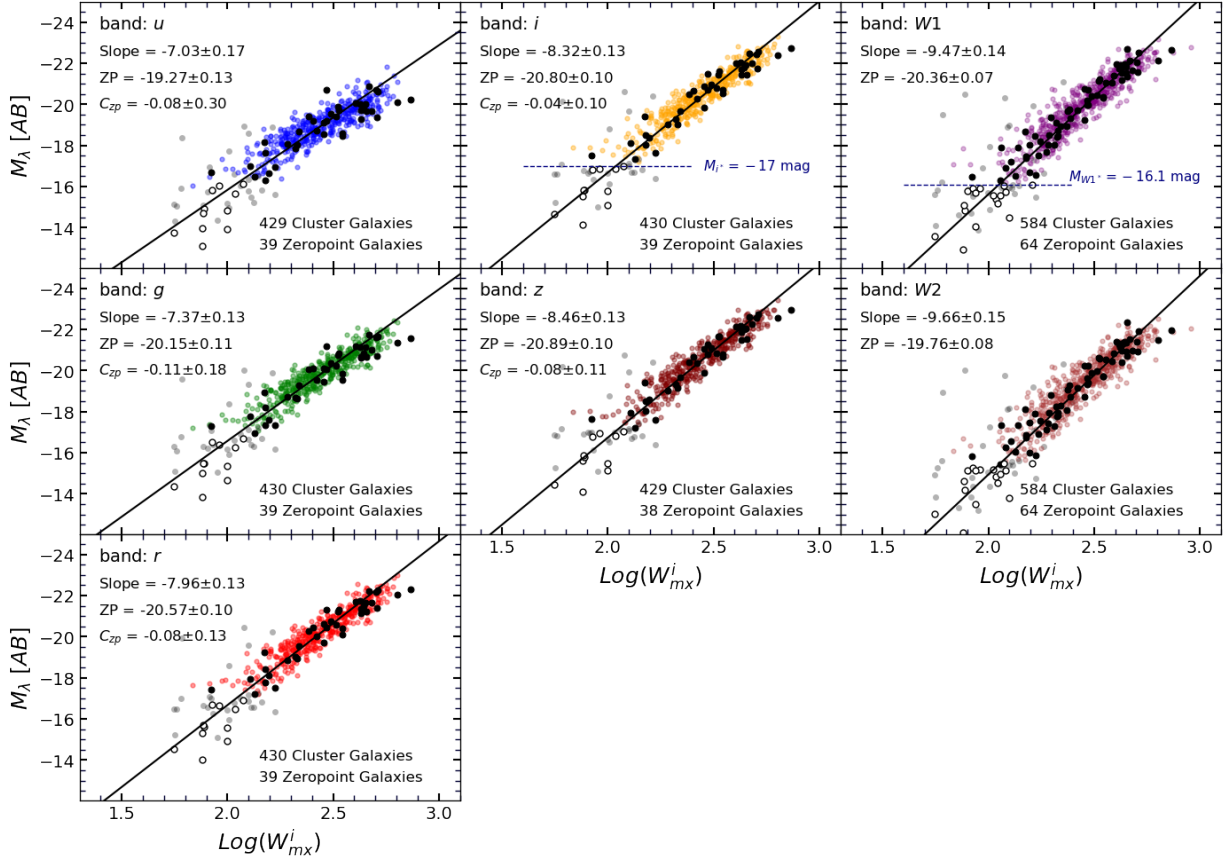


**Figure 8.** Absolute luminosity versus H I linewidth for different wavebands. Solid straight lines illustrate the fitted ITFRs with no bandpass adjustments. Colored points show cluster galaxies that are used for slope calibration. The magnitude limit  $M_i = -17$  mag is imposed in the fitting process, illustrated by the blue dashed horizontal line in the i-band panel. The dashed green line in the W1-band panel shows the equivalent magnitude limit of  $-16.1$  in the W1-band. Gray points are the faint cluster galaxies or the outliers we excluded from the ensemble in the fitting process. Black filled points are the spirals used for zero point calibration. Open circles are zero point calibrators that are fainter than the adopted magnitude limit.

points) are listed in columns (6) and (9) of Table 2, respectively. Residuals  $\Delta M_\lambda^i$  follow an approximately Gaussian distribution and therefore the  $rms$  value can be taken as the  $1\sigma$  error in estimates of target distances.

The averaged  $u$ -band scatter of 0.60 mag is greater than at longer optical wavelengths. The  $u$ -band is sensitive to young stellar populations and dust obscuration. Moreover, the quality of photometry is worst at  $u$ -band where the uncertainties of measured magnitudes are  $\sim 0.10$  mag, about double that at other SDSS bands. At  $g$ ,  $r$ ,  $i$  and  $z$  bands, the averaged  $rms$  scatter is relatively the same and equal to  $\sim 0.50$

mag. Using 267 cluster galaxies, [Tully & Courtois \(2012\)](#) reported the  $rms$  scatter of 0.41 mag for the  $I$ -band (Vega) calibration of ITFR. With an additional 34 galaxies, [Neill et al. \(2014\)](#) found a slightly larger scatter of 0.46 mag at the same waveband. Our averaged  $rms$  scatter about the  $i$ -band relation, based on 430 galaxies, is 0.49 mag. Scatter tends to increase toward the fainter end of the TFR, a domain more completely probed by our more extensive samples. The increased scatter toward fainter magnitudes is demonstrated in Fig. 9. Scatter increases from  $\sim 0.40$  for the most luminous galaxies to  $\sim 0.58$  for the faintest galaxies. It

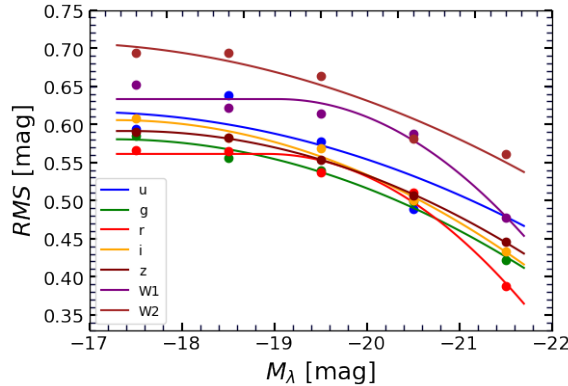


**Figure 9.** Binned RMS scatter of the template clusters galaxies about the linear ITFR at different passbands. Curves are fitted parabolic functions that are flattened after they peak at the faint end.

can be noted that the *rms* scatter for individual clusters recorded in Tables 3 and 4 tend to decrease for the more distant clusters. Progressively with increasing distance only the bright end of the TFR is probed.

Based on 584 galaxies in our sample with infrared photometry, we find that the dispersion about the  $W1$  and  $W2$  calibrations are 0.58 mag and 0.62 mag, respectively, in agreement with previous studies (Sorce et al. 2013; Neill et al. 2014). The latter reports a scatter of 0.54 mag for dispersion about their  $W1$  ITFR fit using 310 galaxies.

Overall, scatter tends to decrease toward the near infrared wavelengths where with the effects of young stellar population and metallicity are minimized, as anticipated by Aaronson et al. (1979). The subsequent substantial increase in scatter at the *WISE* bandpasses is associated with a color term that is discussed in §4.

### 3.6. Cluster distance bias

While the formalism of the ITFR effectively nulls the selection Malmquist bias, another bias remains because of the non uniform population of the luminosity function of a cluster. Here, our concern is restricted to only the gas rich spiral populations which, from compilations combining Virgo, Ursa Major, and Fornax samples, can

be described by Schechter functions (Schechter 1976) with bright end exponential cutoffs characterized by  $M_I^* = -23.0$  and  $M_{W1}^* = -22.0$  and faint end power law slopes  $\alpha = -1.0$  (Tully & Courtois 2012; Neill et al. 2014).

The bias arises when the faint limit in the sampling of a cluster approaches the exponential cutoff magnitude. In such instances, there are more fainter galaxies available to scatter upward into the sample than brighter galaxies to scatter downward out of the sample. The upward scattered systems will tend to lie above an unbiased relation, resulting in a fit to the cluster that is slightly too close. Since the Schechter faint end slope parameter  $\alpha = -1.0$  implies equal numbers per magnitude bin at fainter magnitudes, for relatively nearby clusters there is little bias because there is roughly equal probability of upward and downward scatter. See Neill et al. (2014) for further elaboration.

We determine the amplitudes of the bias in each passband with simulations. However, before discussing that detail we address another concern. Simulations can be used to study the joint effects discussed in this section and the next.

### 3.7. TFR curvature

A close look at Fig. 8 reveals that at the bright end of the TFR, almost all galaxies are below the fitted straight lines, implying that the linear TFR might not perfectly capture the general trend of data points. The departure of bright galaxies from the linear TFR is larger at longer wavelengths. Here, we treat the effect of curvature as an additional bias that is addressed together with the effect of magnitude cutoff bias.

Curvature of the near-IR TFR has been considered in previous studies using *H*-band luminosities (Aaronson et al. 1986, and references therein). Sakai et al. (2000) have used quadratic functions for the  $BVRIH_{-0.5}$  bands and showed that the curvature term increases with wavelengths, which is consistent with what we ob-

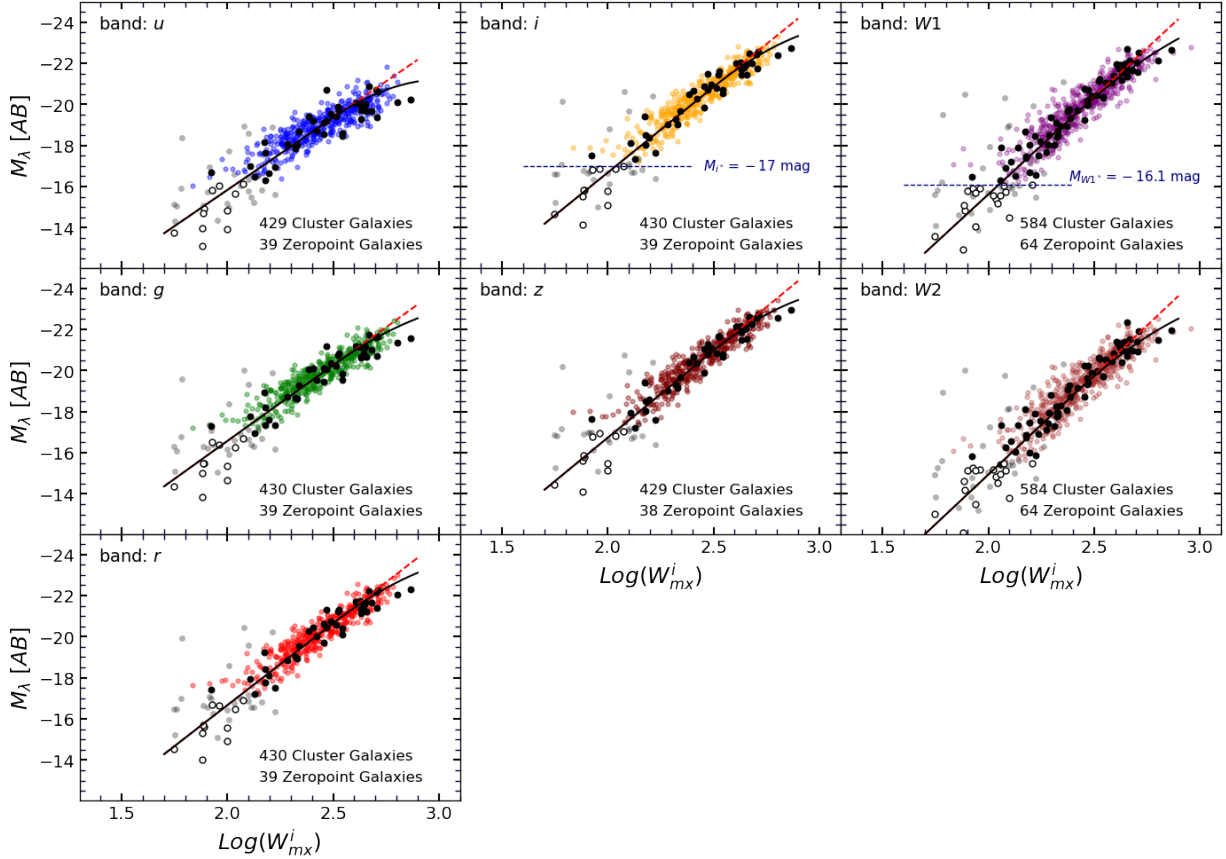


**Figure 10.** Similar to Fig 8. The linear ITFR is replaced with quadratic functions at the bright ends. At  $u$ ,  $g$ ,  $r$ ,  $i$  and  $z$  optical bands, the departure from the linear relation begins at  $\log(W_{mx}^i) = 2.5$ . At  $W1$  and  $W2$  infrared band, the break point is at  $\log(W_{mx}^i) = 2.4$ . In each panel, the dashed solid line displays the continuation of the linear ITFR.

serve in Fig. 8. Noordermeer & Verheijen (2007) describe the effect with linear fits with a break between two slopes, noting systems with declining rotation curves at large radii dominate the flatter portion at the bright end and that formulating a “baryonic” relation (McGaugh 2005) helps to minimize the change in slopes. Neill et al. (2014) account for curvature with the empirical strategy of employing quadratic functions for the TFR without adjustments of magnitudes or linewidths.

In this study, we accept the fitted ITFRs everywhere except for the bright-end where we model the deviations of data points from the linear relation using quadratic functions. Our attempt to fit an inverted quadratic relation failed due to the dramatic increase of scatter about

the resulting TFR. The same issue has been also reported by Neill et al. (2014). Here, to fit the quadratic relation we take the direct fitting approach and let the regression process minimizes residuals along the magnitude axis. To keep the Malmquist bias at a minimum when fitting the quadratic curves, we still use the same template we constructed in the slope calibration process (see §3.1). The uncertainties of magnitudes are much smaller than that of linewidths; thus we project the linewidths error bars onto the magnitude axis based on the slope of the linear TFR.

In our analysis, we examined different locations for the break-point, where there is the transition from linear to quadratic forms. At optical bands, taking the break-point as a free parameter of the fit results in unrealistic fitted

curves, with harsh deviations from the linear relation beginning at  $\log(W_{mx}^i) \sim 2.6$  and a turnover after reaching to a maximum within the range of the data. Rather, at optical bands, we empirically explored break-points to obtain a result that curves gently from the linear relations while leaving enough data points for the fitting process. We adopted  $\log(W_{mx}^i) = 2.5$  for the onset of deviation. At infrared bands by contrast, the break-point is reasonably found from minimization in the fitting process, giving  $\log(W_{mx}^i) = 2.4$ . The following quadratic relation formulates the deviation from the linear TFR after the break-point

$$\Delta M_\lambda = A_2 X^2 + A_1 X + A_0 , \quad (13)$$

where  $X = \log(W_{mx}^i) - 2.5$ . Our fitting procedure requires that the quadratic curve and the linear TFR share the same slope at the break-point, which reduces the number of independent parameters. Table 5 lists  $A_2$  and other essential parameters in the calculation of  $A_1$  and  $A_0$ . Fig. 10 displays the resulting curved relations that apply bright-ward of the break-points, with the previously determined linear ITFRs faint-ward of the break-points. The *rms* scatter of the magnitude offsets from the curved relations are reported in the last column of Table 5. Scatter is not substantially reduced compared to the linear ITFRs because the large fraction of the luminosity-linewidth correlation is still modelled linearly, the deviation of the curved region from linear is modest, and there are not that many galaxies affected by the curvature at the bright end.

### 3.8. Simulations

We follow a similar bias analysis as explained in Tully & Courtois (2012); Sorce et al. (2013), and Neill et al. (2014) with one important difference. Those earlier studies only considered the bias discussed in §3.6 while now we also consider the bias due to curvature, the topic of §3.7.

**Table 5.** Parameters of the curved TFRs. *Slope* and *ZP* are parameters of the linear TFR.

band	<i>Slope</i>	<i>ZP</i>	$\log(W_{mx}^i)$ break-point	$A_2$	rms [mag]
u	-7.03±0.17	-19.27±0.13	2.5	6.59±1.10	0.56
g	-7.37±0.13	-20.15±0.11	2.5	4.18±0.90	0.48
r	-7.96±0.13	-20.57±0.10	2.5	4.56±0.89	0.48
i	-8.32±0.13	-20.80±0.10	2.5	5.34±0.91	0.48
z	-8.46±0.13	-20.89±0.10	2.5	5.81±0.91	0.48
W1	-9.47±0.14	-20.36±0.07	2.4	3.81±0.42	0.56
W2	-9.66±0.15	-19.76±0.08	2.4	4.42±0.43	0.61

These two biases act in opposite senses and we study their effects conjointly with simulations.

We approximate the luminosity function of TFR-applicable galaxies with the Schechter function (Schechter 1976). To determine the faint end slope,  $\alpha$ , we fit to the combination of Virgo-Ursa Major-Fornax cluster samples. The bright end cutoff parameter  $M^*$  is poorly constrained by only these three clusters so, to improve statistics, we add clusters by distance groups, with  $\alpha$  fixed by the nearest three clusters and magnitude ranges for the determination of  $M^*$  increasingly constrained with distance. The fitted Schechter parameters at the different bands are given in Table 6.

The process of generating synthetic samples is given by the following recipe. (1) At each band, we generate a synthetic sample of galaxies with absolute magnitudes drawn from the Schechter luminosity function. (2) We assign a synthetic linewidth to each simulated galaxy based on the curved luminosity-linewidth correlations presented in §3.7. (3) The magnitude of each galaxy is then statistically dispersed assuming a normal distributions with standard deviations taken from the scatter models similar to that presented in Fig. 9, applied here to the curved luminosity-linewidth relations. The left panels of Fig. 11 illustrate the ensemble of 1000 simulated galaxies at *i* and *W1*-bands.

To calculate the amplitude of bias, for any given faint-end magnitude limit,  $M_{lim}$ , we draw 10,000 galaxies randomly with simulated mag-

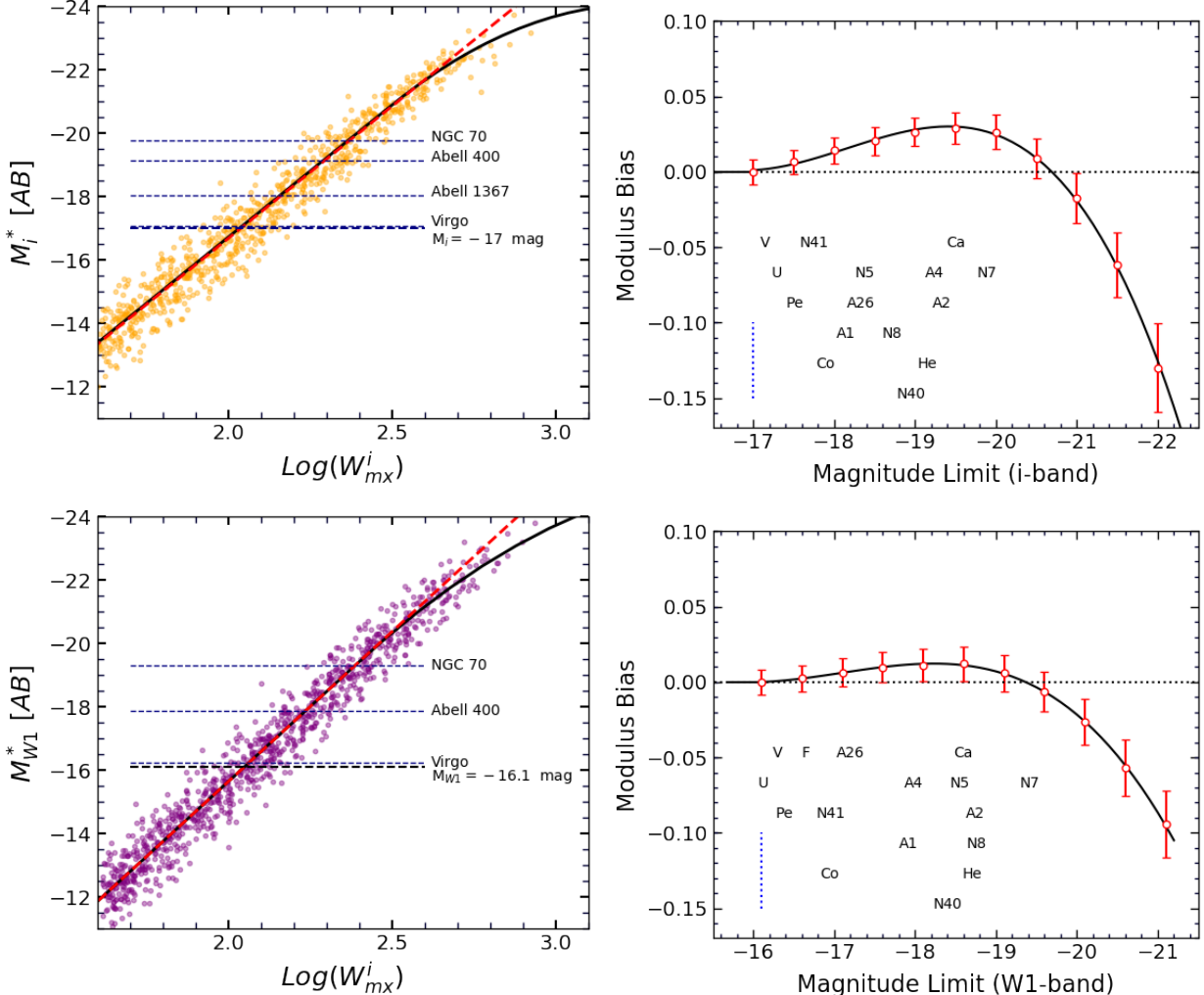


**Figure 11. Left:** 1000 simulated galaxies along the curved TFR drawing from the appropriate Schechter luminosity function and scattered along the magnitude axis based on the *rms* scatter model presented in Fig. 9. Horizontal dashed lines represent the magnitude limit of our sample at *i* and *W1*-bands. Dotted lines display the faint-end magnitude cutoffs of Virgo, Abell 1367, Abell 400 and NGC 70 clusters as examples. **Right:** Distance bias as a function of the faint-end magnitude limit of simulated TFRs. Clusters codes, placed horizontally, locate the faint end magnitude coverage of calibrator clusters. Vertical dotted lines are drawn at the location of the magnitude cutoff of our samples at  $M_i = -17$  and  $M_{W1} = -16.1$  mag.

nitudes brighter than the cutoff magnitude. In our analysis the relative distance moduli of clusters are determined through fitting the linear luminosity-linewidth correlations, therefore we follow the same recipe to measure the magnitudes of the random ensemble. The linewidths of randomly selected galaxies determine the assignments of absolute magnitudes from the model TFR. The average deviation of these

measured magnitudes from input magnitudes is the bias,  $b$ .

The right panels of Fig. 11 plot the bias as a function of magnitude limits. For each magnitude cutoff, we repeat the calculations for 100 different random ensembles and plot the averages and  $1\sigma$  standard deviations of the results. Data points are normalized to zero at the magnitude limits  $M_i = -17$  and  $M_{W1} = -16.1$  mag where bias for a complete sample goes to zero.

**Table 6.** Parameters of the third degree polynomial function,  $b = 0.01 \times \sum_{n=0}^3 B_n M_{lim}^n$ , that fits the distance modulus bias at different wavebands. The last two columns are the fitted parameters of luminosity function as described by the Schechter function.

Band	TFR	Modulus Bias Function				LF Parameters		
		Code	$B_3$	$B_2$	$B_1$	$B_0$	$M^*$	$\alpha$
u	$TF_c$		$1.08 \pm 0.19$	$3.73 \pm 0.95$	$-0.87 \pm 1.23$	$0.16 \pm 0.38$	$-19.9 \pm 0.3$	$-1.0 \pm 0.3$
g	$TF_g$		$0.41 \pm 0.03$	$1.57 \pm 0.21$	$-0.00 \pm 0.35$	$0.12 \pm 0.15$	$-21.3 \pm 0.5$	$-1.0 \pm 0.2$
r	$TF_r$		$0.48 \pm 0.04$	$1.82 \pm 0.24$	$0.37 \pm 0.43$	$0.18 \pm 0.19$	$-21.8 \pm 0.2$	$-1.0 \pm 0.1$
i	$TF_i$		$0.37 \pm 0.02$	$1.26 \pm 0.14$	$-0.28 \pm 0.25$	$0.11 \pm 0.12$	$-22.0 \pm 0.1$	$-1.0 \pm 0.1$
z	$TF_z$		$0.34 \pm 0.02$	$1.14 \pm 0.15$	$-0.30 \pm 0.26$	$0.09 \pm 0.11$	$-22.1 \pm 0.2$	$-1.0 \pm 0.1$
W1	$TF_{W1}$		$0.21 \pm 0.01$	$0.61 \pm 0.05$	$-0.21 \pm 0.10$	$0.00 \pm 0.04$	$-21.9 \pm 0.1$	$-1.0 \pm 0.1$
W2	$TF_{W2}$		$0.25 \pm 0.02$	$0.98 \pm 0.15$	$0.40 \pm 0.28$	$0.12 \pm 0.14$	$-21.3 \pm 0.2$	$-1.0 \pm 0.1$

In this plot, black solid curves are third degree polynomial functions that fit the modulus bias, of the form  $b = 0.01 \times \sum_{n=0}^3 B_n M_{lim}^n$ , where  $B_n$ 's are the coefficient of the polynomial function. Table 6 lists the coefficients of the fitted polynomials.

It is seen in Fig. 11 that the combination of the two biases, those discussed in §3.6 and §3.7 respectively, give results significantly different from that derived by Neill et al. (2014) and earlier because, while the bias due to scatter on the Schechter function is monotonically increasingly positive with distance, the curvature bias is monotonically increasingly negative with distance. With increasing distance, the former bias is initially dominant but then the latter takes over. Over the range of relevance for our calibrator clusters the bias remains positive but is subdued, reaching just  $b \sim 0.04$  at  $i$ -band and  $b \sim 0.02$  at  $W1$ -band.

#### 4. TFR WITH ADDITIONAL PARAMETERS

There have been suggestions to reduce the dispersion in TFR by including additional parameters such as type, color or H I to stellar content (Rubin et al. 1985; Giovanelli et al. 1997; Makarov et al. 2018). In this spirit, Masters et al. (2006) fit the TFR at  $I$ -band for early- and late-type spirals separately. It has been known that the TFR is steeper at longer wavelengths (Tully et al. 1982). This property *must* intro-

duce a color term that affects scatter, producing systematic differences between passbands.

Larger spirals rotate faster as manifested in larger H I linewidths. Larger galaxies are composed of older and redder stellar populations owing to their rapid star formation histories. Consequently, spirals with larger H I linewidths (bigger galaxies) are in general redder, as shown in Fig. 12, causing the fast rotating end of the TFR to rise up relative to the slow rotating end when progressing to longer wavebands. This effect is illustrated in Fig. 13. The TFR progressively steepens from the optical  $u$ -band to the infrared  $W2$ -band.

Consider two spirals that are different in color but are the same in linewidth. Toward infrared bands, the redder galaxy rises in luminosity relative to the bluer galaxy. This effect induces an intrinsic scatter about the TFR that is a function of waveband and the color distribution of the sample galaxies.

The need for a color term in the infrared was clearly documented by Sorce et al. (2013) at  $3.6 \mu m$  using *Spitzer* IRAC images and by Neill et al. (2014) in their study of the TFR at *WISE*  $W1$  and  $W2$  bands. In each of these cases the scatter at infrared bands was reduced by  $\sim 0.1$  mag by the introduction of a color adjustment term. Empirically, color terms can effectively reduce scatter in the TFR at blue-ward and infrared bands, becoming minimally applicable between the  $i$  and  $z$  bands.

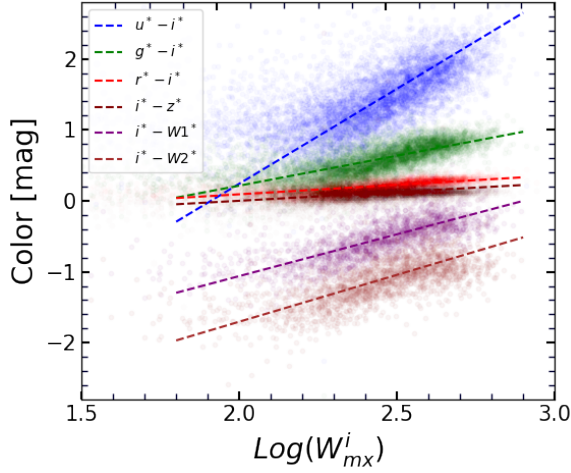


**Figure 12.** Color terms vs. H I linewidth. Each point displays a galaxy. Points are colored based on the color indices they represent. Dashed lines fit the data points of corresponding colors using the least square regression through minimizing the residuals along the vertical axis. The parameters of the fits are presented in Table 7.

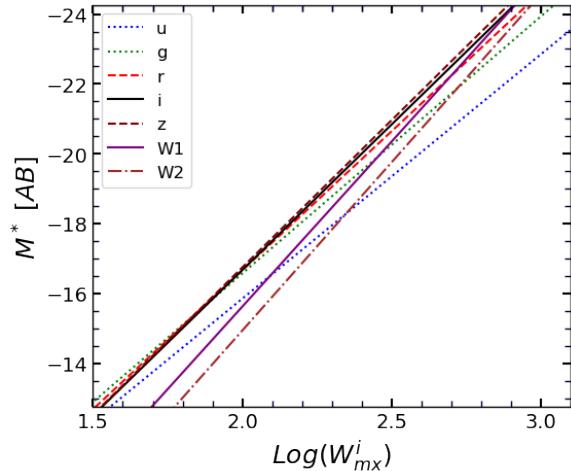


**Figure 13.** ITFR fits in different optical and infrared wavebands. The power law lines are those displayed in Fig. 8.

Here, we evaluate correlations between TFR residuals and the various distance independent observables that are available in our study. The features that we use to probe the type, morphology and other general characteristics of spirals include (1) color indices calculated from optical and infrared magnitudes, (2) mean surface

brightnesses of galaxies at different wavebands as probes of galaxy morphology, and (3) pseudo-colors derived from the difference between the H I magnitude calculated from Eq. 1 and optical/infrared magnitudes,  $C_{21\lambda} = m_{21} - m_\lambda$ , as an estimate of the ratio of the galaxy H I content to its stellar mass.

These observables are not all independent of each other. In §4.1, we explore the correlations between these observables and the H I linewidth. The ability of quantifiable features to lower the scatter about the TFR is investigated in §4.2.

#### 4.1. Distance independent observables versus H I linewidth

In this section we perform our analysis using a sample of  $\sim 10,000$  spirals with high quality photometry measurements. Distance independent characteristics are evaluated in reference to the H I linewidth, the main distance independent parameter of the TFR. We model the general relations between H I linewidth and other observable features using power laws that are formulated as

$$\Omega = \omega_0(\log W_{mx}^i - 2.5) + \omega_1 . \quad (14)$$

where  $\Omega$  can be any of the investigated features such as color terms, surface brightness, or  $C_{21\lambda}$  parameter.  $\omega_0$  and  $\omega_1$  are the slope and zero-point of the linear relations. We minimize residuals along the  $\Omega$  axis in the least square regression to fit the linear relation.

In the absence of the galaxy SED, color indices are effective substitutes that provide useful information on the type, morphology, stellar populations and the general characteristics of galaxies. Our spirals have measured magnitudes in seven different optical/infrared bands. Twenty-one color indices can be defined using these magnitudes. In this work, we only consider six independent color terms with reference to the  $i$ -band. Our choice of  $i$ -band is based on the relatively high image quality at that wave-

band; changing the reference passband does not change our conclusions.

The color terms with respect to  $i$ -band are seen in Fig. 12. Bigger spirals consist of redder/older stars and populate the larger linewidths region of the diagram. These relations steepen as the span of the wavebands that define the color term increases.

The correlations between linewidth and  $C_{21\lambda}$  at different passbands are plotted in Fig 14. Spirals with more positive  $C_{21\lambda}$  values (pseudo-redder) have less H I gas relative to their stellar content.  $C_{21\lambda}$  increases with linewidth since the efficient star formation in bigger spirals consumes larger fractions of their H I content to form stars. The linear relations steepen as the  $C_{21\lambda}$  pseudo-color is based on longer wavebands. For a given galaxy, the 21cm magnitude is a fixed parameter in the calculation of  $C_{21\lambda}$  so redder colors at larger linewidths translate to steeper  $C_{21\lambda}$  slopes toward the infrared.

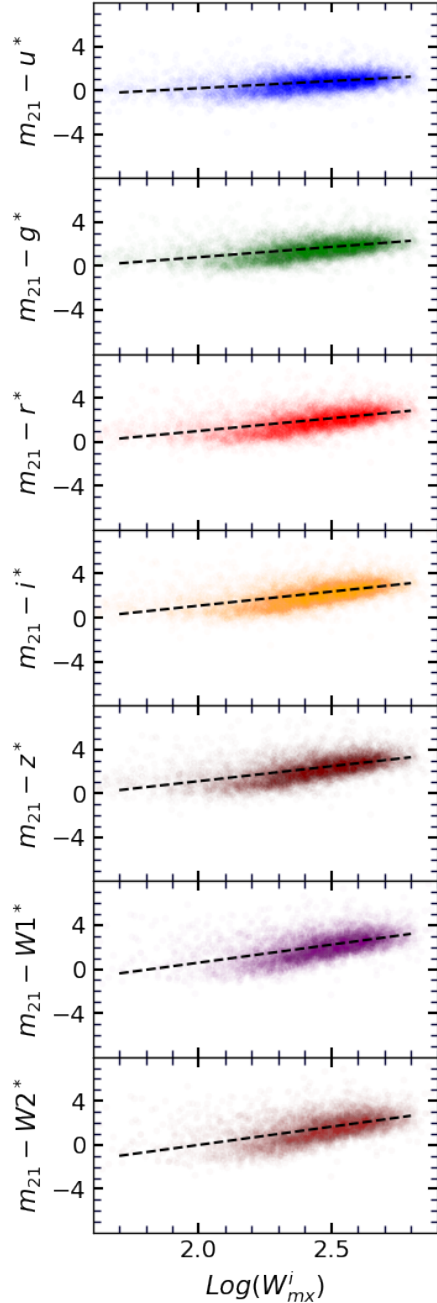
Fig. 15 plots the mean surface brightness within the half light radius versus H I linewidth. Surface brightness is corrected for the effect of inclination using Eq. 5. More massive spirals with larger H I linewidths tend toward higher surface brightness.

Table 7 contains the parameters of the linear fits that describe the correlations between various distance dependant observables and H I linewidths.

#### 4.2. Linking TFR dispersion to distance independent observables

It is shown that the scatter in the TFR can be reduced through introducing additional parameters. Sorce et al. (2013) and Neill et al. (2014) found significant correlations between deviations from the infrared TFRs and their optical-infrared color terms. In this section we explore a range of ways to reduce scatter about the TFR at different wavebands.

The deviation of a spiral galaxy in the slope calibrator sample from the ITFR is given by



**Figure 14.** Similar to Fig. 12 but for  $m_{21} - m_{\lambda}^*$  versus H I linewidth, where  $\lambda$  represents different optical/infrared bands. The unit of the vertical axis is magnitude. The parameters of the black dashed fitted lines are presented in Table 7.

Eq. 9. These residuals from the ITFR are plotted against observables and the trends of linear fits are evaluated with correlation coefficients. The strongest correlations are used to adjust

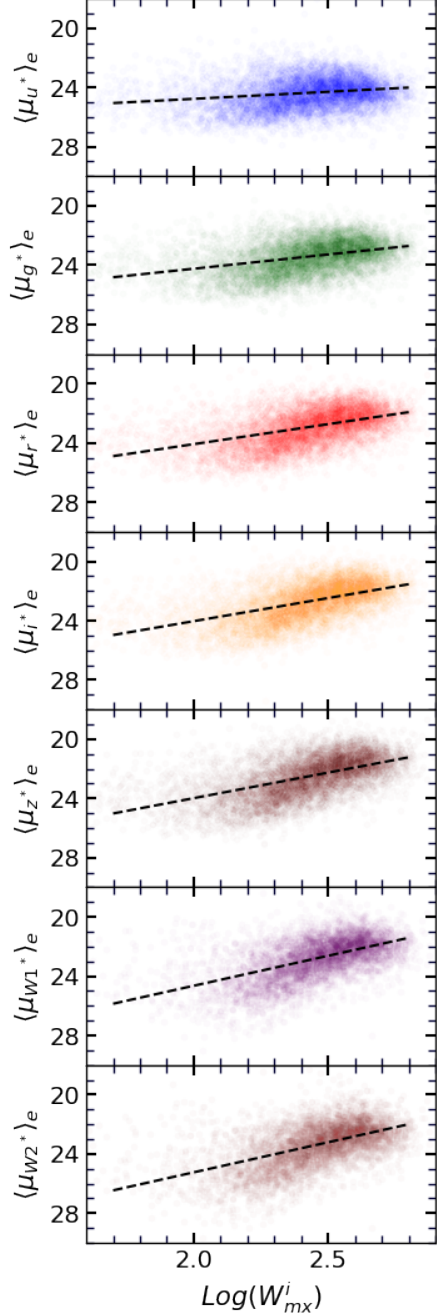


**Figure 15.** Similar to Fig. 12 but for mean effective surface brightness,  $\langle \mu_{\lambda^*} \rangle_e^{(i)}$ , versus H I linewidth at different wavebands. The unit of the vertical axis is mag  $\text{arcsec}^{-2}$ . The parameters of the black dashed fitted lines are presented in Table 7.

magnitudes, resulting in modified ITFRs with smaller scatter. In this process, we consider two groups of observables. The first group consists

**Table 7.** Parameters of the linear correlations between various distance independent observables and H I linewidths as expressed by Eq. 14. The parameter  $rms$  is the root mean square of the dispersion in data about the fitted lines along the axis of the corresponding parameter.  $C$  in the last column is the correlation coefficient and quantifies the strength of the relations.

#	$\Omega^{\dagger}$	$\omega_0$	$\omega_1$	$rms$	$C(\%)$
(1)	(2)	(3)	(4)	(5)	(6)
1	$u^* - i^*$	2.68	1.58	0.87	33
2	$g^* - i^*$	0.84	0.64	0.18	66
3	$r^* - i^*$	0.27	0.23	0.07	61
4	$i^* - z^*$	0.25	0.12	0.07	47
5	$i^* - W1^*$	1.18	-0.47	0.23	66
6	$i^* - W2^*$	1.32	-1.04	0.28	60
7	$m_{21} - u^*$	1.30	0.84	0.74	36
8	$m_{21} - g^*$	1.86	1.73	0.79	46
9	$m_{21} - r^*$	2.31	2.14	0.86	51
10	$m_{21} - i^*$	2.56	2.36	0.89	54
11	$m_{21} - z^*$	2.72	2.47	0.91	56
12	$m_{21} - W1^*$	3.27	2.22	1.00	53
13	$m_{21} - W2^*$	3.32	1.65	1.02	53
14	$\langle \mu_{u^*} \rangle_e$	-0.95	24.30	1.37	15
15	$\langle \mu_{g^*} \rangle_e$	-1.92	23.28	1.08	37
16	$\langle \mu_{r^*} \rangle_e$	-2.70	22.74	1.13	47
17	$\langle \mu_{i^*} \rangle_e$	-3.12	22.48	1.14	52
18	$\langle \mu_{z^*} \rangle_e$	-3.45	22.26	1.16	55
19	$\langle \mu_{W1^*} \rangle_e$	-4.05	22.63	1.22	54
20	$\langle \mu_{W2^*} \rangle_e$	-4.06	23.21	1.41	49

$\dagger$   $\Omega_{1-13}$  are in  $\text{mag}$ .

$\dagger$   $\Omega_{14-20}$  are in  $\text{mag arcsec}^{-2}$ .

of all 20 parameters listed in the second column of Table 7. The second group considers the residuals of the distance independent parameters from their linear relations with respect to H I linewidths

$$\Delta\Omega^i = \Omega_{obs}^i - \Omega , \quad (15)$$

where  $\Omega_{obs}^i$  represents any of the individual distance independent observed characteristics and

**Table 8.** The parameters of the linear relation between deviations of magnitudes from the unadjusted TFR as expressed in Eq. 16.  $C$  in the last column denotes the correlation strength between deviations and the corresponding observable feature,  $\Theta$ .

Deviation from TFR (1)	Correction Parameter ( $\Theta$ ) (2)	$\Phi_{Slope}$ (3)	$\Phi_{ZP}$ (4)	$C$ (%) (5)
$u^* - \text{Mean Correlation}^{\dagger}$	$u^* - i^*$	$0.76 \pm 0.05$	$-1.13 \pm 0.07$	61
	$u^* - W1^*$	$0.50 \pm 0.03$	$-0.48 \pm 0.04$	58
	$\Delta(\langle \mu_{u^*} \rangle_e)$	$-0.13 \pm 0.02$	$-0.21 \pm 0.04$	21
	$\Delta(m_{21} - u^*)$	$0.17 \pm 0.03$	$-0.29 \pm 0.05$	27
$g^* - \text{Mean Correlation}$	$g^* - i^*$	$0.73 \pm 0.09$	$-0.45 \pm 0.06$	35
	$g^* - W1^*$	$0.35 \pm 0.05$	$-0.04 \pm 0.02$	32
	$i^* - W1^*$	$0.49 \pm 0.08$	$0.26 \pm 0.05$	25
$r^* - \text{Mean Correlation}$	$g^* - i^*$	$0.44 \pm 0.09$	$-0.27 \pm 0.06$	21
	$i^* - W1^*$	$0.34 \pm 0.08$	$0.18 \pm 0.05$	16
	$\Delta(i^* - W1^*)$	$-0.14 \pm 0.11$	$0.00 \pm 0.02$	22
	$\Delta(\langle \mu_{r^*} \rangle_e)$	$0.06 \pm 0.02$	$-0.01 \pm 0.02$	23
	$\Delta(m_{21} - r^*)$	$-0.05 \pm 0.02$	$0.01 \pm 0.02$	14
$i^* - \text{Mean Correlation}$	$g^* - i^*$	$0.29 \pm 0.10$	$-0.18 \pm 0.06$	14
	$i^* - W1^*$	$0.28 \pm 0.08$	$0.14 \pm 0.05$	12
	$\Delta(g^* - i^*)$	$-0.31 \pm 0.14$	$0.00 \pm 0.02$	19
	$\Delta(i^* - W1^*)$	$-0.24 \pm 0.11$	$0.00 \pm 0.02$	26
	$\Delta(\langle \mu_{i^*} \rangle_e)$	$0.06 \pm 0.02$	$-0.02 \pm 0.02$	24
	$\Delta(m_{21} - i^*)$	$-0.06 \pm 0.02$	$0.01 \pm 0.02$	18
$z^* - \text{Mean Correlation}$	$g^* - i^*$	$0.21 \pm 0.10$	$-0.14 \pm 0.06$	11
	$i^* - W1^*$	$0.23 \pm 0.08$	$0.11 \pm 0.05$	10
	$\Delta(g^* - i^*)$	$-0.39 \pm 0.13$	$0.00 \pm 0.02$	21
	$\Delta(i^* - W1^*)$	$-0.31 \pm 0.11$	$-0.01 \pm 0.02$	29
	$\Delta(\langle \mu_{z^*} \rangle_e)$	$0.07 \pm 0.02$	$-0.02 \pm 0.02$	26
	$\Delta(m_{21} - z^*)$	$-0.08 \pm 0.02$	$0.01 \pm 0.02$	21
$W1^* - \text{Mean Correlation}$	$i^* - W1^*$	$-0.28 \pm 0.09$	$-0.15 \pm 0.05$	13
	$\Delta(i^* - W1^*)$	$-1.08 \pm 0.11$	$-0.04 \pm 0.02$	53
	$\Delta(\langle \mu_{W1^*} \rangle_e)$	$0.16 \pm 0.02$	$-0.05 \pm 0.02$	38
	$\Delta(m_{21} - W1^*)$	$-0.10 \pm 0.02$	$0.00 \pm 0.02$	28
$W2^* - \text{Mean Correlation}$	$i^* - W2^*$	$-0.39 \pm 0.08$	$-0.44 \pm 0.09$	22
	$\Delta(i^* - W2^*)$	$-1.09 \pm 0.09$	$-0.07 \pm 0.02$	59
	$\Delta(\langle \mu_{W2^*} \rangle_e)$	$0.19 \pm 0.02$	$-0.07 \pm 0.02$	40
	$\Delta(m_{21} - W2^*)$	$-0.12 \pm 0.02$	$-0.01 \pm 0.02$	29

$\dagger$  Mean correlation is given by the unadjusted ITFR at each band,  $TF_{\lambda}$ , where  $\lambda = u, g, r, i, z, W1$  and  $W2$ , as formulated by Eq. 7 with optimized parameters listed in Table 2.

$\Omega$  is calculated from linewidth following Eq. 14 and the parameters in Table 7.

We express the general correlations between deviation from the ITFR and galaxy observ-

ables using the linear relation

$$\Delta M_{\lambda}^{(\Theta)} = \Phi_{Slope} \Theta + \Phi_{ZP}, \quad (16)$$

where  $\Delta M_{\lambda}^{(\Theta)}$  is the output of the model for deviations from the ITFR at the waveband  $\lambda$ , and  $\Theta$  is any of the observable features,  $\Omega_{obs}$  or  $\Delta\Omega$ .  $\Phi_{Slope}$  and  $\Phi_{ZP}$  are the slope and zero point of the linear relation. Table 8 lists the parameters of correlations between various observables,  $\Omega_{obs}$  or  $\Delta\Omega$ , and deviations from the mean unadjusted ITFRs (see Fig. 8). To save space, this list only includes observables with the strongest correlations and a set of important features; these include mean effective surface brightness at each band,  $\langle \mu_{\lambda^*} \rangle_e$ , their deviations from the linear relations with linewidth as described by Eq. 14  $\Delta(\langle \mu_{\lambda^*} \rangle_e)$ , and the  $m_{21} - m_{\lambda}^*$  pseudo-colors.

An observable  $\Theta$  that is highly correlated to the ITFR residuals,  $\Delta M$ , offers a modified ITFR with smaller dispersion. The modified relation is constructed based on the adjusted apparent magnitudes that are given as

$$C_{\lambda}(\Theta) = m_{\lambda}^* - \Delta M_{\lambda}^{(\Theta)}, \quad (17)$$

where  $\Delta M_{\lambda}^{(\Theta)}$  is calculated based on the observable parameter,  $\Theta$ , following Eq. 16. The same algorithm as explained in §3 is pursued to determine the slope and zero-point of the revised ITFR that has the form  $\mathcal{M}_{C_{\lambda}(\Theta)}^* = Slope(\log W_{mx}^i - 2.5) + ZP$ . In Table 9, we present the parameters of our ITFR fits for unadjusted and adjusted magnitudes. In this table, the unadjusted relations are denoted by  $TF_{\lambda}$  codes. We give specific attention to interesting cases where either the rms scatter of the relation is significantly reduced after adjusting magnitudes or the correction parameter is highly correlated with the dispersion of the original relation according to Table 8. These cases are attributed unique codes for the further discussion.

Following the procedure discussed in 3.7, we fit a second degree polynomial to the bright-end of the luminosity-linewidth correlations for each of the adjusted and unadjusted cases. The last two column of Table 9 list the parameters of the fitted curves as formulated in Eq. 13.

The distance modulus of a spiral galaxy with the absolute pseudo-magnitude,  $\mathcal{M}_{C_\lambda(\Theta)}^*$ , that is given by the modified ITFR is derived as

$$\mu_{C_\lambda(\Theta)} = C_\lambda(\Theta) - \mathcal{M}_{C_\lambda(\Theta)}^* . \quad (18)$$

where  $C_\lambda(\Theta)$  is the galaxy apparent pseudo-magnitude that is determined by Eq. 17.

#### 4.3. Modified ITFRs at $u$ -band

Among the correction parameters presented in the  $u$ -band section of Table 8, the  $u^* - i^*$  and  $u^* - W1^*$  colors are highly correlated with deviations from the mean  $u$ -band ITFR with the correlation factors of 61% and 58%, respectively. These correlations are illustrated in Fig. 16 together with the best fitted linear relations described by Eq. 16. The parameters of the fitted red lines are derived following the least square optimization along the vertical axis. Our fitting procedure ignores the horizontal errors, because they are significantly smaller than the vertical uncertainties and are relatively the same for all spirals. These two linear relations are

$$\Delta M_u^{(u^* - i^*)} = -(1.13 \pm 0.07) + (0.76 \pm 0.05)(u^* - i^*) , \quad (19a)$$

$$\Delta M_u^{(u^* - W1^*)} = -(0.48 \pm 0.04) + (0.50 \pm 0.03)(u^* - W1^*) , \quad (19b)$$

where the parameter  $\Theta$  in Eq. 16 is replaced by  $(u^* - i^*)$  and  $(u^* - W1^*)$  color terms. The revised ITFR relations are then derived based on the  $u$ -band pseudo-magnitudes,  $C_u(\Theta)$ , through

$$C_u(u^* - i^*) = u^* - \Delta M_u^{(u^* - i^*)} , \quad (20a)$$

$$C_u(u^* - W1^*) = u^* - \Delta M_u^{(u^* - W1^*)} . \quad (20b)$$

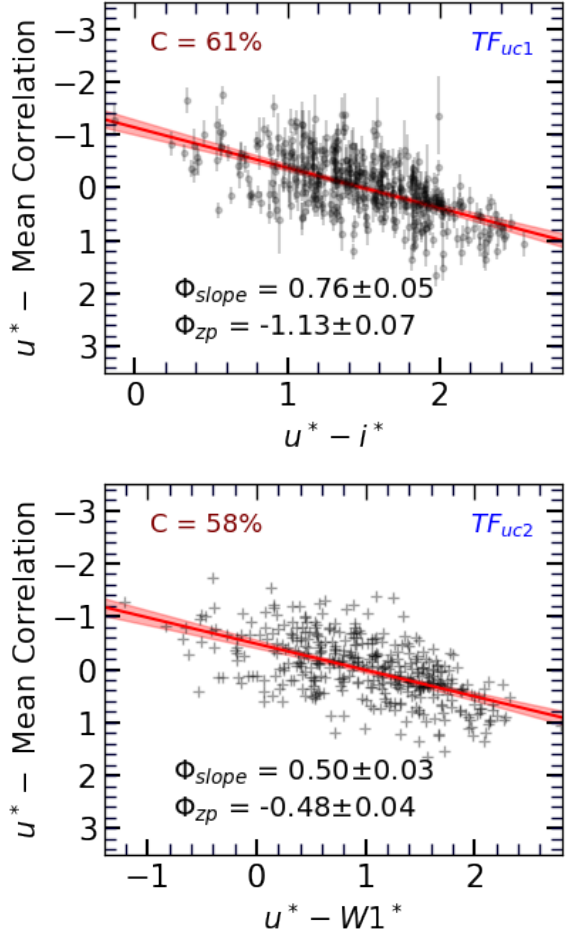


**Figure 16.** Deviations from the mean unadjusted ITFRs at  $u$ -band versus color. Each black point represents a galaxy. Dominant errors are along the vertical axis. The best linear relation is derived by least square regression incorporating the vertical uncertainties. Vertical error bars are displayed in the top panel as example. The 95% confidence envelope is displayed about each fitted line. In the top left corner of each panel,  $C$  is the correlation coefficient of the plotted parameters as listed in Table 8. In the top right corner is the code for the corresponding corrected ITFR.

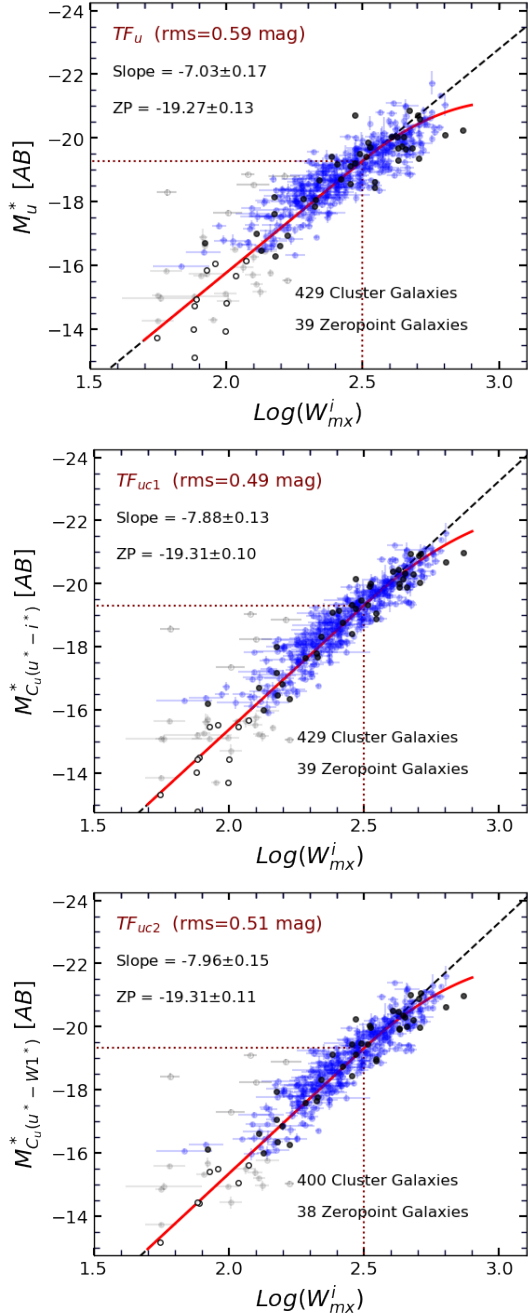


**Figure 17.** Unadjusted and revised ITFR relations. **Top:** The unadjusted ITFR at  $u$ -band ( $TF_u$ ). This panel is the same as the top-left panel of Fig. 8. The rms of vertical residuals about the relation is 0.59 mag. **Middle:** The modified ITFR after adjusting magnitudes using the  $u^* - i^*$  color ( $TF_{uc1}$ ) with the rms scatter of 0.49 mag. **Bottom:** The modified ITFR after adjusting magnitudes based on the  $u^* - W1^*$  color ( $TF_{uc2}$ ) with the rms scatter of 0.51 mag.

The corresponding modified ITFRs have the form

$$\begin{aligned} \mathcal{M}_{C_u(u^* - i^*)}^* = & - (19.31 \pm 0.10) \\ & - (7.88 \pm 0.13)(\log W_{mx}^i - 2.5), \end{aligned} \quad (21a)$$

$$\begin{aligned} \mathcal{M}_{C_u(u^* - W1^*)}^* = & - (19.31 \pm 0.11) \\ & - (7.96 \pm 0.15)(\log W_{mx}^i - 2.5). \end{aligned} \quad (21b)$$

We assign the  $TF_{uc1}$  and  $TF_{uc2}$  codes to the revised ITFRs presented in Eq. 21a and 21b, respectively. These relations are illustrated in the middle and bottom panels of Fig. 17. For comparison, the top panel of Fig. 17 shows the unadjusted ITFR constructed using  $u$  magnitudes ( $TF_u$ ). In this figure, The partially curved relations are illustrated in solid red, with the linear part below the break-point at  $\log W_{mx}^i = 2.5$  and the polynomial fits to data points brightward of the break-point. Dashed black lines are the continuations of the linear ITFRs. To evaluate the performance of the models we compare the scatters about the linear magnitude-linewidth relations. The rms of residuals from the unadjusted  $TF_u$  of 0.59 mag is significantly reduced to 0.49 mag and 0.51 mag for  $TF_{uc1}$  and  $TF_{uc2}$ , respectively. The  $TF_{uc2}$  model requires the availability of  $WISE$  photometry that is only present for 400 out of 429 galaxies with  $u$ -band photometry. However, we do not expect that the lack of 29 galaxies from the  $TF_{uc2}$  sample has a significant influence on our final conclusion.

The  $u$ -band is sensitive to populations of blue stars and star forming regions, whereas the majority of the baryonic mass in spiral galaxies resides in older stellar populations that dominate at longer wavebands. Color terms reduce scatter by providing information about older stellar populations that are sub-dominant in the  $u$ -band imaging.

#### 4.4. Modified ITFRs at $g$ -band

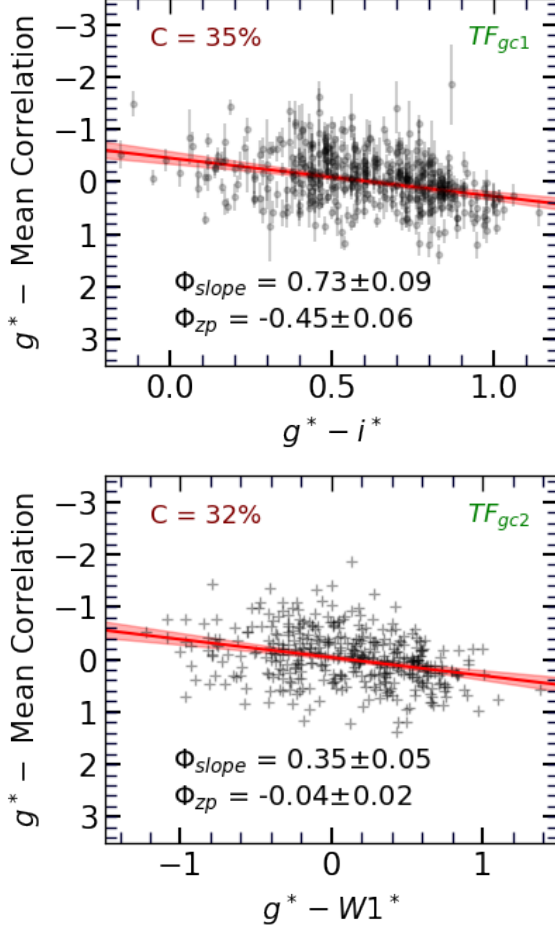


**Figure 18.** Same as Fig. 16 but for deviations from the mean unadjusted ITFRs at  $g$ -band versus color.

Resembling the  $u$ -band, it is seen in Table 8 that deviations from the mean unadjusted ITFRs at  $g$ -band are most correlated with  $g^* - i^*$  and  $g^* - W1^*$  color indices, with correlation factors of 35% and 32%, respectively. These correlations are shown in Fig. 16. The parameters of the two linear fits required to adjust the  $g$ -band magnitudes are presented in Table 8. The corresponding adjusted ITFRs based on the  $g$ -band

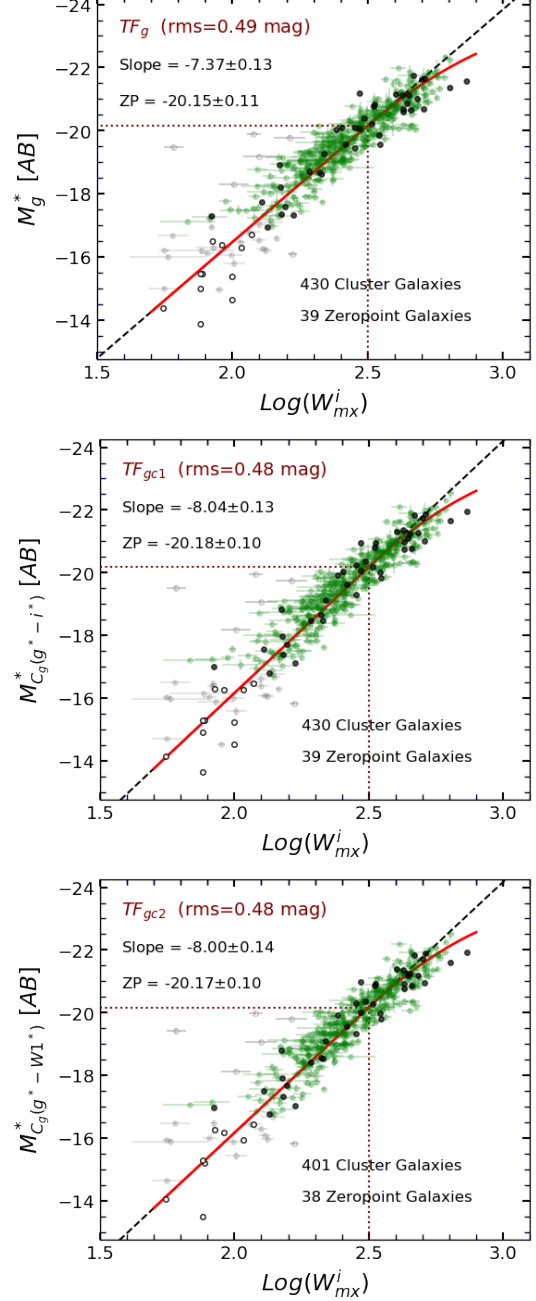


**Figure 19.** Same as Fig. 17 for  $g$ -band.

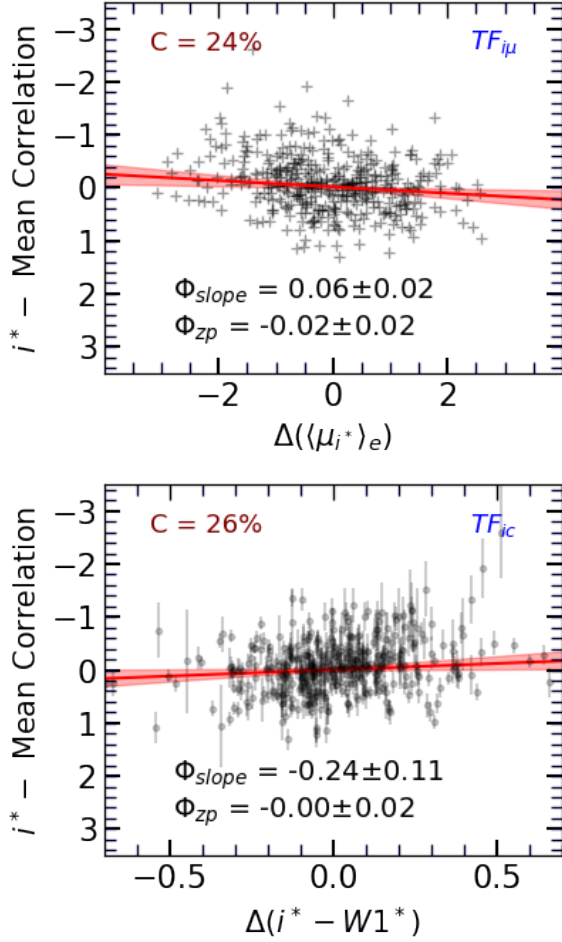


**Figure 20.** Deviations from the mean ITFR at  $i$ -band as functions of surface brightness and color.

pseudo-magnitudes are given as

$$\begin{aligned} \mathcal{M}_{C_g(g^*-i^*)}^* = & - (20.18 \pm 0.10) \\ & - (8.04 \pm 0.13)(\log W_{mx}^i - 2.5), \end{aligned} \quad (22a)$$

$$\begin{aligned} \mathcal{M}_{C_g(g^*-W1^*)}^* = & - (20.17 \pm 0.10) \\ & - (8.00 \pm 0.14)(\log W_{mx}^i - 2.5). \end{aligned} \quad (22b)$$

The modified ITFR models that are represented by Eq. 22a and 22b are labelled with  $TF_{gc1}$  and  $TF_{gc2}$  codes (also see Table 9).

#### 4.5. Modified ITFRs at $r$ , $i$ and $z$ bands

The  $rms$  scatter in unadjusted ITFRs at  $r$ ,  $i$  and  $z$  bands are similar. Exploring tables 8

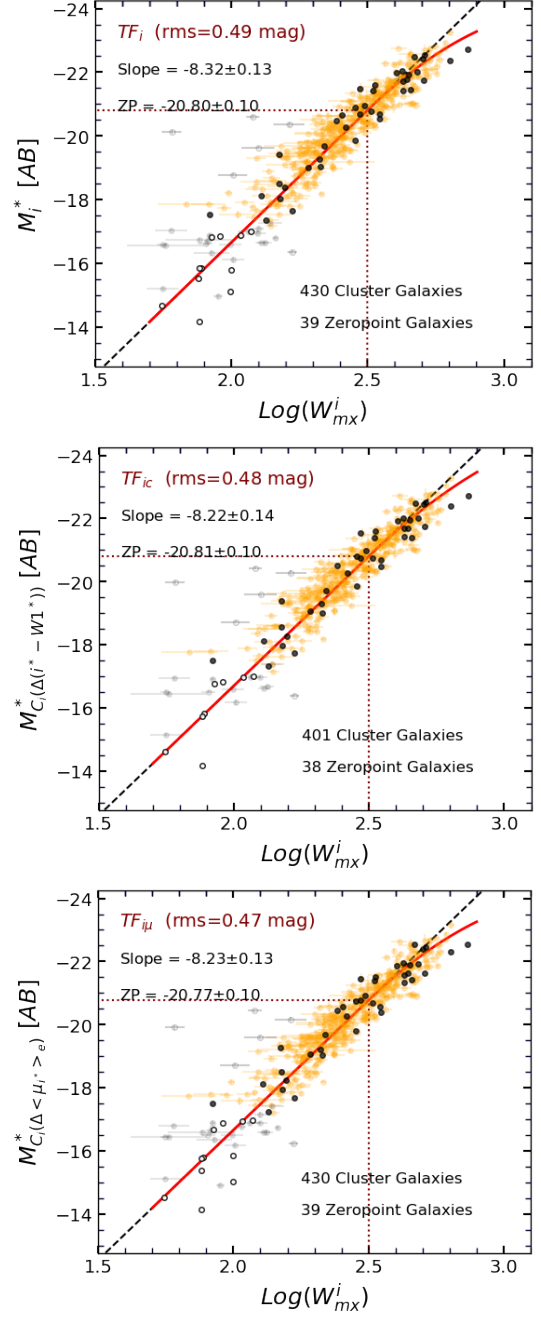


**Figure 21.** Same as Fig. 17 for  $i$ -band.

and 9 jointly reveals the observables with the most significant correlations to ITFR residuals, hence most capable of reducing the scatter in adjusted ITFR relations, to be  $\Delta(i^* - W1^*)$  and  $\Delta(\langle \mu_{\lambda^*} \rangle_e)$ . The correlations with these observables in the case of  $i$ -band are shown in Fig. 20. The adjusted ITFRs based on these models are

labeled with the codes  $TF_{\lambda c}$  and  $TF_{\lambda\mu}$ , respectively, where  $\lambda$  is replaced with  $r$  and  $i$  and  $z$ .

All the correlations at  $r$  and  $i$  and  $z$  bands are weak. Comparing the lower panels of Figs. 16, 18, and 20, the slopes of the correlations with colors  $\lambda^* - W1^*$  transition from positive to negative, flattening to zero slope between  $z$  and  $W1$  bands. Adjustments coupled to color parameters do little to improve the TFR scatter (see Table 9). Likewise, correlation coefficients related to surface brightness or H I pseudo-colors are small. We favor *not* making third parameter adjustments to the TFR at  $r$ ,  $i$  and  $z$  bands since adding parameters adds uncertainties.

#### 4.6. Modified ITFRs at infrared $W1$ and $W2$ bands

The effectiveness of the optical-infrared colors to reduce the scatters of the unadjusted ITFRs at infrared bands have been already noticed in previous studies. For example, Sorce et al. (2013) observed a significant correlation between the  $I$ –IRAC [3.6] color and deviations from the mean ITFR constructed at infrared IRAC [3.6] band. Inspired by their work, Neill et al. (2014) apply the same methodology to reduce the scatter about the WISE  $W1$  and  $W2$  ITFRs.

Giving consideration to a similar color correlation with the present data, Tables 8 lists the linear dependencies of unadjusted  $W1$  and  $W2$  ITFRs residuals on the  $i^* - W1^*$  and  $i^* - W2^*$  parameters. We find similar trends as previous studies, however the correlations are not very significant and cannot usefully reduce the scatter of the ITFR.<sup>10</sup> Instead, we consider  $\Delta(i^* - W1^*)$  and  $\Delta(i^* - W2^*)$  color terms that are in higher correlation with the ITFR residuals, with the correlation factors of 53% and 59%,

<sup>10</sup> Similarly, Ponomareva et al. (2017) found the color term in a bi-variate solution for the luminosity-linewidth relation at the IRAC [3.6] band did not rise to a level of significance.

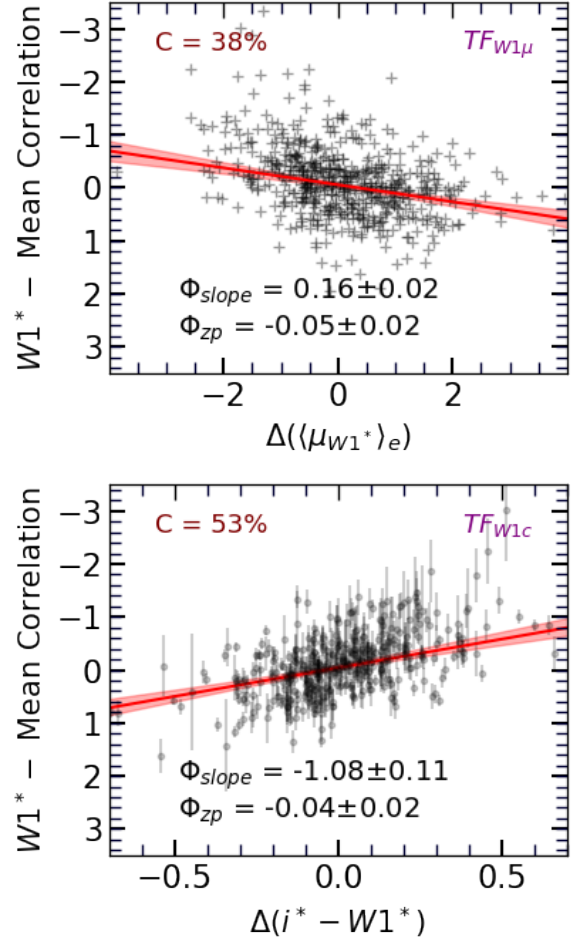


**Figure 22.** Same as Fig. 20 but for deviations from the mean ITFR at infrared  $W1$ - band.

respectively. In addition, the surface brightness seems to be capable of reducing the scatter efficiently.

Fig. 22 displays the deviations from the  $W1$  band ITFR versus  $\Delta(i^* - W1^*)$  and  $\Delta(⟨\mu_{W1^*}⟩_e)$ . In both cases, the slopes and zero-points of the fitted linear relations are significant. Analogous relations have been derived for the  $W2$  band. The middle and bottom panels of Fig. 23 plot the revised luminosity-linewidth relations after applying corrections based on the  $\Delta(i^* - W1^*)$  and  $\Delta(⟨\mu_{W1^*}⟩_e)$  parameters, labelled  $TF_{W1c}$  and  $TF_{W1\mu}$ , respectively. In addition, the adjustments using additional parameters reduce the curvature of the best fit after the breakpoint at  $\log(W_{mx}^i) = 2.4$ . This reduction is in

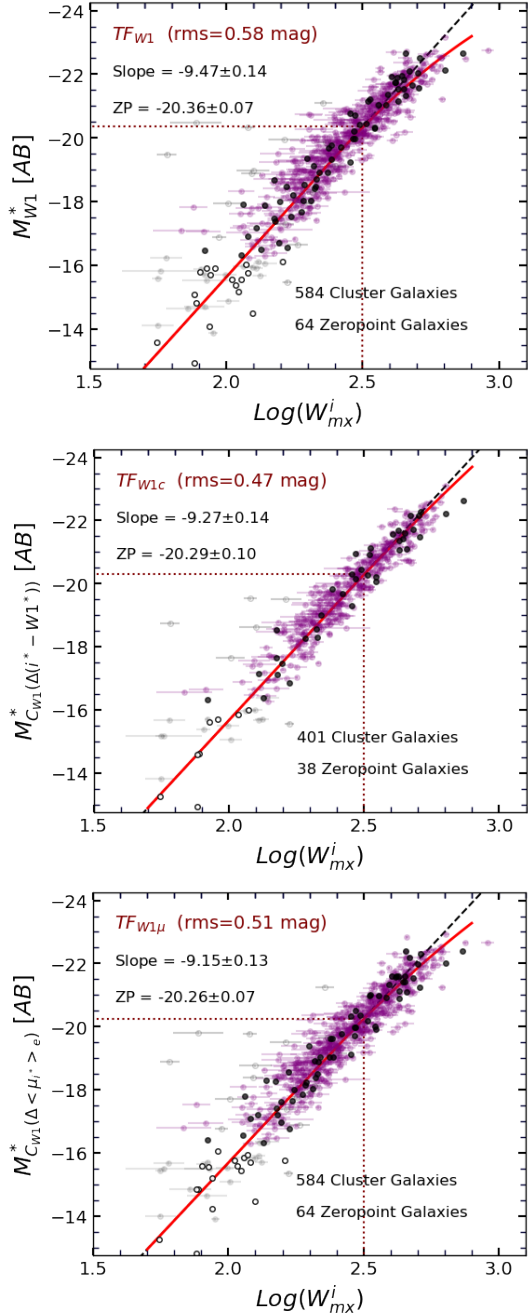


**Figure 23.** Same as Fig. 17 for  $W1$ -band. Red solid line displays the partially curved ITFRs that deviate from the linear relation for galaxies with  $H1$  linewidths larger than  $\log(W_{mx}^i) = 2.4$ .

agreement with the results of Neill et al. (2014), where no curvature for the relation of the color adjusted magnitude with linewidth is apparent. The larger correlation factor of  $\Delta(i^* - W1^*)$  (53%) compared to that of  $\Delta(\langle \mu_{W1^*} \rangle_e)$  (38%)

translates to greater reduction in the scatter about the adjusted TF model. The 0.58 mag *rms* scatter of  $TF_{W1}$  is lowered to 0.47 mag and 0.51 mag for the  $TF_{W1c}$  and  $TF_{W1\mu}$  cases, respectively.

Ever since Aaronson et al. (1979) it has been anticipated that minimal scatter in the TFR would be achieved at infrared bands. Indeed Ponomareva et al. (2017) explored correlations in 12 bands from the far ultraviolet to  $4.5\mu\text{m}$  and found the tightest fit at  $3.6\mu\text{m}$ . With extensive modeling, adjustments can be made to account for radiation from dust associated with star forming regions that can contribute 10 – 30% of light at  $3.4 – 3.6\mu\text{m}$  (Querejeta et al. 2015). In any event, the minimization in scatter found by Ponomareva et al. (2017) and similarly by Lelli et al. (2016) refer to the scatter orthogonal to mean bi-variate fits. The scatter relevant for the acquisition of distances is that in magnitudes and is aggravated by the steepening of slopes toward the infrared.

#### 4.7. The Baryonic Tully-Fisher Relation

McGaugh (2005) pointed out that progressively toward galaxies of lower stellar mass the fractional representation of interstellar gas mass increases. He suggested that luminosity be replaced by a linear combination of luminosity and the  $H1$  flux as a measure of the galactic baryon content,  $M_b$ .

$$M_b = 1.33M_{HI} + \Upsilon_* L_\lambda \quad (23)$$

where  $\Upsilon_*$  is the stellar mass-to-light ratio ( $\sim 0.5M_\odot/L_\odot$  at  $\lambda = 3.6\mu\text{m}$ ) and the multiplier 1.33 on  $M_{HI}$  accounts for the unseen contribution of Helium (Lelli et al. 2019).

The baryonic formulation tends to flatten the TFR by raising the low linewidth end relative to the high linewidth end and may somewhat mitigate curvature (Noordermeer & Verheijen 2007). Nevertheless, we have not given the baryonic TFR close attention. The neutral gas

**Table 9.** TFR parameters before and after corrections

Band	Sample	Correction Parameter	TFR Code	Universal Slope			Zero Point			Curvature	
				Ngal	Slope	rms	Ngal	Mag	rms	break-point	$A_2$
u	OP	...	TF <sub>u</sub>	429	-7.03±0.17	0.59	39	-19.27±0.13	0.75	$\log(W_{mx}^i)=2.5$	6.59±1.10
u	OP	$u^* - i^*$	TF <sub>uc1</sub>	429	-7.88±0.13	0.49	39	-19.31±0.10	0.60	2.5	5.03±0.90
u	OP+IR	$u^* - W1^*$	TF <sub>uc2</sub>	400	-7.96±0.15	0.51	38	-19.31±0.11	0.61	2.5	5.90±0.91
u	OP	$\Delta(\langle\mu_{u^*}\rangle_e)$		429	-7.35±0.16	0.59	39	-19.33±0.12	0.60	2.5	6.55±1.10
u	OP	$\Delta(m_{21} - u^*)$		435	-7.58±0.17	0.59	39	-19.43±0.13	0.75	2.5	6.58±1.12
g	OP	...	TF <sub>g</sub>	430	-7.37±0.13	0.49	39	-20.15±0.11	0.62	2.5	4.18±0.90
g	OP	$g^* - i^*$	TF <sub>gc1</sub>	430	-8.04±0.13	0.48	39	-20.18±0.10	0.59	2.5	4.91±0.89
g	OP+IR	$g^* - W1^*$	TF <sub>gc2</sub>	401	-8.00±0.14	0.48	38	-20.17±0.10	0.59	2.5	5.01±0.89
g	OP+IR	$i^* - W1^*$		401	-7.85±0.14	0.48	38	-20.17±0.11	0.61	2.5	5.12±0.88
r	OP	...	TF <sub>r</sub>	430	-7.96±0.13	0.49	39	-20.57±0.10	0.59	2.5	4.56±0.89
r	OP	$g^* - i^*$		430	-8.41±0.13	0.49	39	-20.59±0.10	0.58	2.5	5.23±0.91
r	OP+IR	$i^* - W1^*$		401	-8.28±0.14	0.49	38	-20.58±0.10	0.58	2.5	5.13±0.90
r	OP+IR	$\Delta(i^* - W1^*)$	TF <sub>rc</sub>	401	-7.89±0.14	0.48	38	-20.57±0.10	0.58	2.5	3.59±0.92
r	OP	$\Delta(\langle\mu_{r^*}\rangle_e)$	TF <sub>rμ</sub>	430	-7.89±0.13	0.47	39	-20.55±0.10	0.59	2.5	4.34±0.90
r	OP	$\Delta(m_{21} - r^*)$		430	-7.81±0.13	0.47	39	-20.53±0.10	0.59	2.5	4.35±0.87
i	OP	...	TF <sub>i</sub>	430	-8.32±0.13	0.49	39	-20.80±0.10	0.59	2.5	5.34±0.91
i	OP	$g^* - i^*$		430	-8.64±0.14	0.49	39	-20.81±0.10	0.59	2.5	5.87±0.94
i	OP+IR	$i^* - W1^*$		401	-8.58±0.14	0.49	38	-20.81±0.10	0.58	2.5	5.71±0.94
i	OP	$\Delta(g^* - i^*)$		430	-8.22±0.13	0.49	39	-20.80±0.10	0.59	2.5	4.68±0.89
i	OP+IR	$\Delta(i^* - W1^*)$	TF <sub>ic</sub>	401	-8.22±0.14	0.48	39	-20.81±0.10	0.57	2.5	3.91±0.94
i	OP	$\Delta(\langle\mu_{i^*}\rangle_e)$	TF <sub>iμ</sub>	430	-8.23±0.13	0.47	39	-20.77±0.10	0.59	2.5	5.03±0.92
i	OP	$\Delta(m_{21} - i^*)$		435	-8.13±0.13	0.48	39	-20.75±0.10	0.59	2.5	5.01±0.89
z	OP	...	TF <sub>z</sub>	429	-8.46±0.13	0.50	38	-20.89±0.10	0.57	2.5	5.81±0.91
z	OP	$g^* - i^*$		429	-8.69±0.13	0.49	38	-20.88±0.10	0.59	2.5	6.21±0.93
z	OP+IR	$i^* - W1^*$		400	-8.60±0.14	0.50	37	-20.88±0.10	0.57	2.5	5.82±0.94
z	OP	$\Delta(g^* - i^*)$		429	-8.33±0.13	0.48	38	-20.88±0.10	0.56	2.5	4.96±0.89
z	OP+IR	$\Delta(i^* - W1^*)$	TF <sub>zc</sub>	400	-8.29±0.14	0.47	37	-20.88±0.10	0.55	2.5	3.77±0.94
z	OP	$\Delta(\langle\mu_{z^*}\rangle_e)$	TF <sub>zμ</sub>	429	-8.35±0.13	0.47	38	-20.86±0.10	0.57	2.5	3.88±0.95
z	OP	$\Delta(m_{21} - z^*)$		429	-8.22±0.13	0.47	38	-20.81±0.10	0.57	2.5	5.34±0.88
W1	IR	...	TF <sub>W1</sub>	584	-9.47±0.14	0.58	64	-20.36±0.07	0.60	2.4	3.81±0.42
W1	OP+IR	$i^* - W1^*$		401	-9.21±0.15	0.54	38	-20.30±0.10	0.60	2.4	3.41±0.44
W1	OP+IR	$\Delta(i^* - W1^*)$	TF <sub>W1c</sub>	401	-9.27±0.14	0.47	38	-20.29±0.10	0.56	2.4	1.22±0.40
W1	IR	$\Delta(\langle\mu_{W1^*}\rangle_e)$	TF <sub>W1μ</sub>	584	-9.15±0.13	0.51	64	-20.26±0.07	0.57	2.4	2.55±0.40
W1	IR	$\Delta(m_{21} - W1^*)$		584	-9.12±0.13	0.53	64	-20.29±0.08	0.58	2.4	3.35±0.40
W2	IR	...	TF <sub>W2</sub>	584	-9.66±0.15	0.62	64	-19.76±0.08	0.65	2.4	4.42±0.43
W2	OP+IR	$i^* - W2^*$		401	-9.14±0.15	0.55	38	-19.70±0.11	0.63	2.4	3.47±0.43
W2	OP+IR	$\Delta(i^* - W2^*)$	TF <sub>W2c</sub>	401	-9.40±0.14	0.47	38	-19.70±0.10	0.56	2.4	1.13±0.41
W2	IR	$\Delta(\langle\mu_{W2^*}\rangle_e)$	TF <sub>W2μ</sub>	584	-9.18±0.13	0.52	64	-19.62±0.07	0.60	2.4	2.67±0.39
W2	IR	$\Delta(m_{21} - W1^*)$		584	-9.22±0.14	0.56	64	-19.67±0.08	0.62	2.4	3.79±0.41

only becomes a substantial component of the baryonic mass of a galaxy in the vicinity of our faint cutoff at  $M_i = -17$ . In particular, though, we are not confident of the reliability of the H I flux parameters in our H I catalogs at the Extragalactic Distance Database. Ponomareva et al. (2016) has noted the basis of our concerns. In the compilation of the All Digital H I catalog great care was given to the accumulation of linewidths on a coherent system but H I

fluxes have not received such attention. Contributions come from a variety of telescopes with beams of different sizes that may or may not capture most of the H I flux. Inhomogeneities in flux measurements might depend on telescope, hence portions of the sky, and on targets sizes, hence distance.

## 5. CLUSTERS RADIAL VELOCITIES

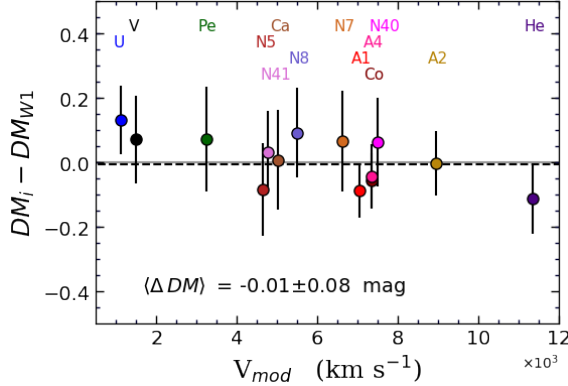


**Figure 24.** Differences between the measured cluster distance moduli at  $i$  and  $W1$  bands versus their radial velocities,  $V_{mod}$ . The cluster codes are horizontally placed based on the corresponding  $V_{mod}$  values. The horizontal axis is the cosmologically corrected radial velocity of clusters in the CMB rest frame. Dashed horizontal lines display the average of the  $DM$  offset,  $\langle \Delta DM \rangle$ , calculated by incorporating the vertical error bars.

The mean radial velocity of each cluster is determined by averaging the velocities of all known constituents (not just those with distance measurements) using the bi-weight statistics discussed in Beers et al. (1990). For clusters beyond  $3,500 \text{ km s}^{-1}$  memberships are based on the 2MASS galaxy group catalog of Tully (2015) while within  $3,500 \text{ km s}^{-1}$  we draw on the group catalog of Kourkchi & Tully (2017). The average radial velocities of clusters are then shifted to the cosmic microwave background (CMB) rest frame  $V_{cmb}$ , and further adjusted for cosmological curvature  $V_{mod} = fV_{cmb}$  where

$$f = 1 + \frac{1}{2}[1 - q_0]z - \frac{1}{6}[1 - q_0 - 3q_0^2 + j_0]z^2, \quad (24)$$

the jerk parameter  $j_0 = 1$ , and the acceleration parameter  $q_0 = \frac{1}{2}(\Omega_m - 2\Omega_\Lambda) = -0.595$  assuming  $\Omega_m = 0.27$ ,  $\Omega_m + \Omega_\Lambda = 1$ . These cosmological adjustments are negligible for the nearby clusters, reaching in the extreme 3% for Hercules Cluster. The second column of Table 10 lists these adjusted radial velocities,  $V_{mod}$ , and their uncertainties.

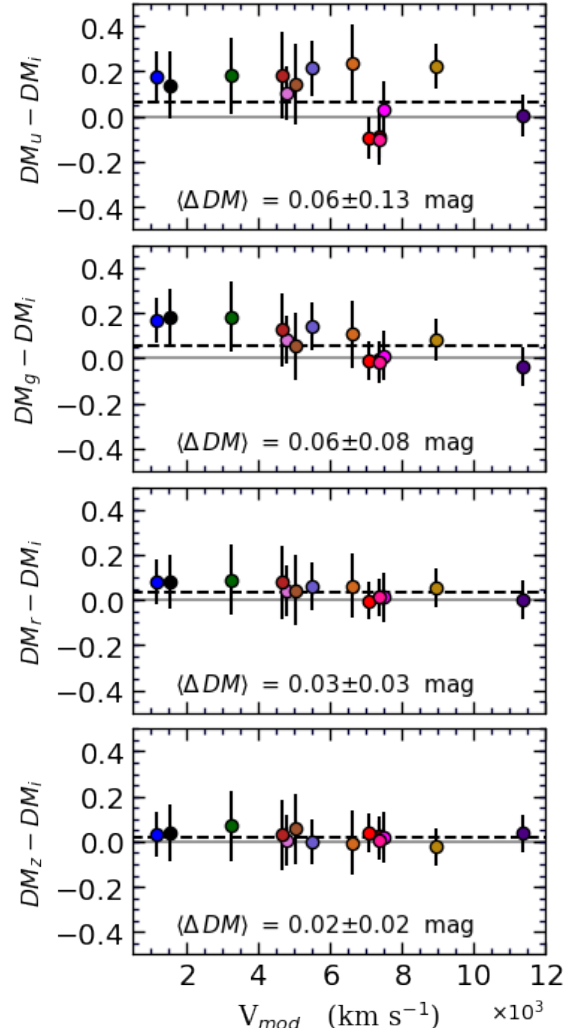


**Figure 25.** Offset of cluster distance moduli,  $DM$ , measured at the optical  $u$ ,  $g$ ,  $r$  and  $z$  bands from those measured at  $i$  band using the unadjusted TFR relations. Color scheme and other details are the same as in Fig. 24.

## 6. DISTANCES OF CLUSTERS

A product of the TFR calibration is the distance moduli of the galaxy clusters used to form the TFR template. The raw distance moduli of clusters,  $DM_o$ , are listed in column (6) of Table 10 for different TFR models listed in column (4). Column (7) contains  $b$ , the luminosity function scatter bias combined with the effect of TFR curvature that is calculated following the discussion presented in §3.6. Column (8) contains any other adjustment bias that will be dis-

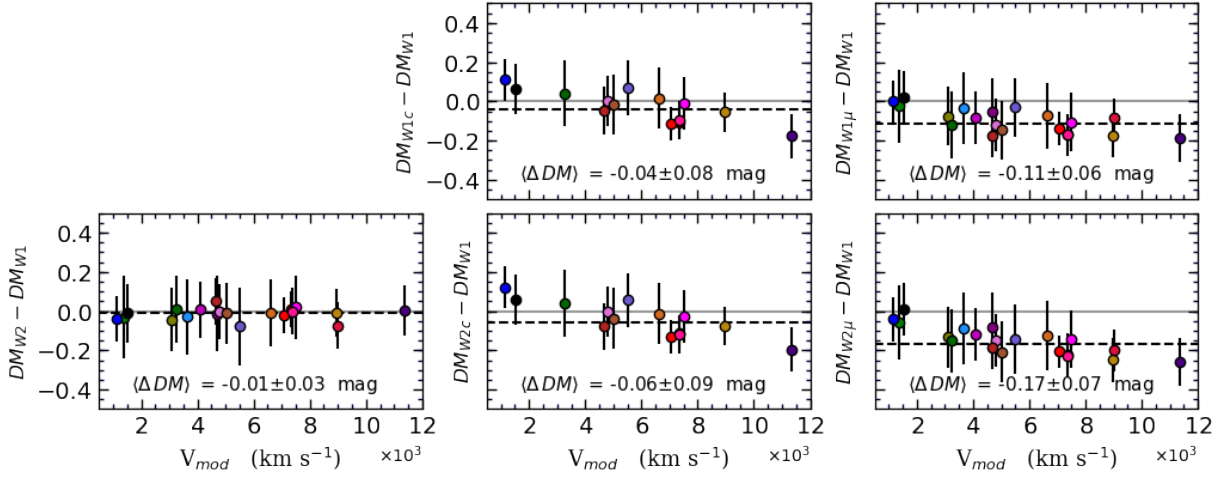


**Figure 26.** Unaltered distance moduli at  $W1$ -band are taken as the reference of comparison in all panels. The bottom panels show comparisons with  $W2$ , with the panel at left involving unaltered moduli. The middle panels give color-adjusted moduli differences with respect to unadjusted  $W1$  moduli, the  $W1$  case on top and the  $W2$  case on the bottom. The panels at the right are similar but now with surface brightness corrections. Color scheme and other details are the same as 24.

cussed later in this section,  $\Delta DM$ . Column (9) tabulates the corrected distance moduli given as  $DM_c = DM_o + b + \Delta DM$ , that are converted to distances in unit of Mpc and presented in column (10).

Initially we set  $\Delta DM = 0$  and we plot the differences of the bias corrected moduli as a function of the clusters radial velocities to test the consistency of the measurements at different passbands. At optical bands 14 galaxy clusters contributed in our calibration process while in the infrared 20 clusters are available. First we check the consistency of our distance measurements between optical and infrared bands using the  $i$  and  $W1$  bands as proxy, and then we evaluate the agreements within optical and infrared bands separately.

Fig. 24 plots the differences of the distance moduli measured at  $i$  and  $W1$  band for the 14 clusters in common. No significant offset is apparent. We notice positive offsets for the nearest three clusters Virgo, Ursa Major and Fornax and a negative offset for the most distant Hercules cluster. After further exploration, we find that the Virgo galaxies are slightly redder and the Hercules galaxies are bluer, compared

to the average color distribution of the template galaxies used in the calibration process. Redder galaxies appear to be more luminous at longer wavelengths, and therefore they are located at smaller distances. The opposite effect is true for galaxies that are in general bluer than average. This subtle effect has been seen earlier (Tully & Pierce 2000; Neill et al. 2014) with the very nearby clusters, in the first case with entirely distinct optical and infrared photometry and in the second case with distinct optical photometry.

We look for offsets of the cluster moduli, measured using the unadjusted TFRs ( $TF_\lambda$  models), at optical passbands relative to that at the  $i$ -band in Fig. 25. It is seen that systematic differences in moduli are highest for the  $u$  band and decrease toward longer wavelengths. These offsets are not statistically significant, nonetheless we offer adjustments at  $u$  and  $g$  bands so moduli in these bands are on the same scale as the  $i$ -band. In our final analyses, though, we do *not* make use of  $u$  and  $g$  moduli. By contrast, we see in Fig. 25 that moduli at  $r$ ,  $i$  and  $z$  are in close agreement without any modifications. *Going forward, we only use the  $r$ ,  $i$  and  $z$  re-*

lations without relative bandpass adjustments to measure distances with optical photometry.

For evaluation of the infrared distances, we choose the  $W1$  band as reference. In order to measure distances at this infrared band, we apply the adjusted ITFRs that have smaller scatters. As discussed in §4.5, both  $\Delta(i^* - W1^*)$  and  $\Delta(\langle\mu_{W1^*}\rangle_e)$  parameters are capable of reducing the scatter. However it is more practical for our purpose to use the corrections based on the  $W1$  surface brightness because sometimes we lack optical photometry.

Fig. 26 displays the differences of the clusters moduli at adjusted and unadjusted infrared bands with reference to the  $W1$  band. The left panel of this plot shows an excellent consistency between  $W1$  and  $W2$  results. The middle panels of Fig. 26 show that the color adjusted models,  $TF_{W1c}$  and  $TF_{W2c}$ , result in slightly smaller distance moduli compared to that measured using the unadjusted models. The right panels of Fig. 26 reveal more significant offsets for the  $TF_{W1\mu}$  and  $TF_{W2\mu}$  moduli, calling for adjustments to distance moduli of  $DM_{W1\mu} + 0.11$  and  $DM_{W2\mu} + 0.17$ . These offsets are listed as  $\Delta DM$  in column (8) of Table 10 and are included to form the adjusted moduli,  $DM_c$ .

These discrepancies arise from the still modest size of the zero point calibrator sample that does not fairly representing the global distribution of galaxies. The bias is evaluated with improved statistics using the field galaxies of the impending *Cosmicflows-4* distance compilation. We take as a baseline  $DM_i$  rather than  $DM_{W1}$  because, as shown in Fig. 24, cluster distance moduli measured at  $i$  and  $W1$  bands are reasonably consistent and with this choice we can test for other discrepancies between measured moduli at optical and infrared passbands.

The top panels of Fig. 27 and Fig. 28 plot  $DM_{W1\mu} - DM_i$  of the field galaxies versus their linewidths and  $i^* - W1^*$  colors, respectively. It would be preferable to use the  $i^* - W1^*$  color

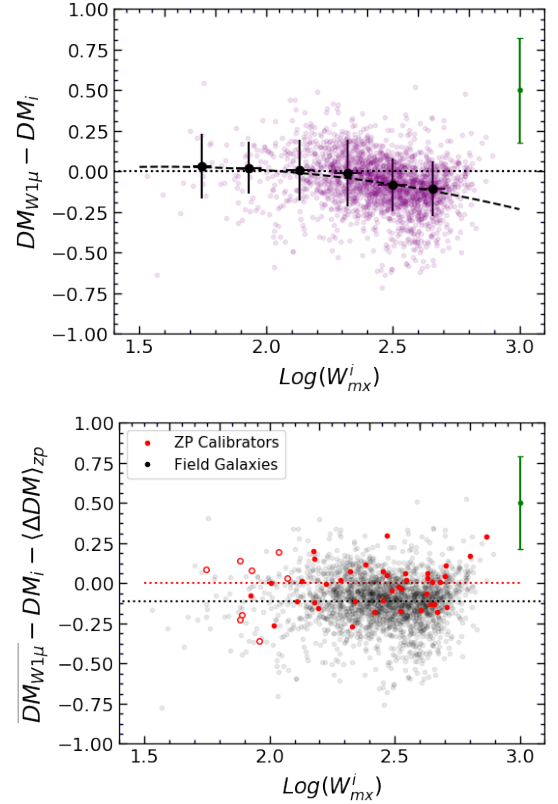


**Figure 27.** **Top:** Differences in distance moduli of field galaxies,  $DM$ , between  $TF_{W1\mu}$  and  $TF_i$  cases. Each purple point represents a galaxy, with black points showing averages in horizontal bins of 0.2. Black dashed line is the best quadratic fitted function on all data points, minimizing vertical residuals, with expression  $DM_{W1\mu} - DM_i = (-0.13 \pm 0.06)X^2 + (0.42 \pm 0.28)X + (-0.31 \pm 0.33)$ , where  $X = \log W_{mx}^i$ . **bottom:** Offset of distance moduli after correcting  $DM_{W1\mu}$  for the linewidth dependent bias presented in top panel,  $DM_{W1\mu} - DM_i$ . The zero point of the plot is set at  $\langle \Delta DM \rangle_{zp} = 0.11$  mag, the average of the moduli differences of the zero point calibrators, displayed as red filled points. Gray points represent field galaxies, while red open circles are rejected faint calibrators. Black dotted line at  $-0.11$  is at the average moduli offset of field galaxies. Green error bars at top right give typical differences for field galaxies.

term to redress the observed trends because the ITFR already uses linewidths to measure distances. However, the  $i^* - W1^*$  color does not

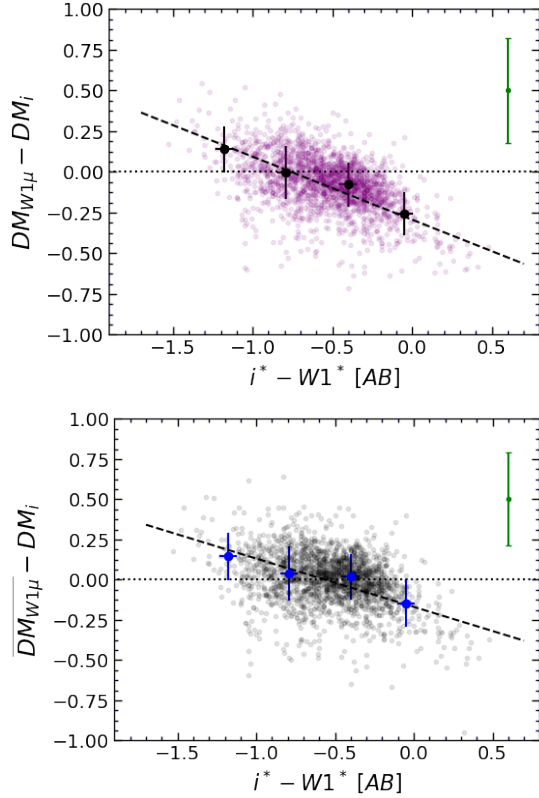


**Figure 28.** **Top:** The distance moduli offset of the field galaxies versus  $i^* - W1^*$  color. Other details are the same as the top panel of Fig. 27. **Bottom:** Same as the top panel but with the bias corrected  $\overline{DM}_{W1\mu}$ .

provide a practical solution if optical photometry is missing. The correlation between color terms and linewidth shown in Fig. 12, provides a route to the bias correction that is available for all our samples.

The black dashed curve in the top panel of Fig. 27 shows our best fit to the offsets of moduli as a quadratic function of linewidth, shifting the  $DM_{W1\mu}$  values to the same level as  $DM_i$ . The offsets of the modified distance moduli,  $\overline{DM}_{W1\mu} - DM_i$ , are plotted in the bottom panels of Fig. 27 and Fig. 28.

In the bottom panel of Fig. 27 the filled red points represent the zero-point calibrators after adjustments following the description in the caption for the top panel of this figure. The gray points illustrate the related adjusted values for

the full field sample. On average the field sample manifests a vertical drift of  $0.11 \pm 0.08$  mag in the negative direction. The value of this net offset is in agreement with the moduli offset in the top right panel of Fig. 26. Evidently, the pattern of surface brightness corrections imposed on the zero-point calibrators does not tightly follow that of the field galaxies. It is expected that this discrepancy would be neutralized by adopting a larger/fairer sample of zero point calibrators.

Comparing the two panels of Fig. 27, we infer that our quadratic formulation based on linewidth significantly but imperfectly improves the consistency of the distance measurements between  $TF_{W1\mu}$  and  $TF_i$  alternatives. In this paper our focus is on galaxy clusters that contain spirals with a variety of properties such that, on average, wavelength discrepancies are expected to be moderate. In applications to the full field sample, discussed in a follow-up paper, concerns for bias in distances to individual galaxies due to wavelength dependent color variations will require attention.

## 7. $H_0$ FROM CLUSTERS

For each cluster,  $j$ , the Hubble parameter is calculated as  $H_j = V_{mod,j}/D_j$ . The values of the Hubble parameters based on different TFR models are listed in column (11) of Table 10. Fig. 29 provides plots of the resulting  $H_j$  given the distance moduli measured at  $i$  and  $W1$ -bands using unadjusted TFR fits. Large scatters are observed for cluster within  $4,000$  km s $^{-1}$  due to substantial peculiar motions within our host supercluster complex. In Fig. 29, dotted lines show an error envelope of  $\pm 200$  km s $^{-1}$  to illustrate how the Hubble parameter is influenced by peculiar velocities as a function of distance. We find the Hubble constant of  $H_0 = 75.9 \pm 1.3$  km s $^{-1}$  Mpc $^{-1}$  based on the unadjusted TFR analysis at  $i$ -band with the rms scatter of  $3.9$  km s $^{-1}$  Mpc $^{-1}$ . For unadjusted TFR at  $W1$ -band,  $H_0 =$

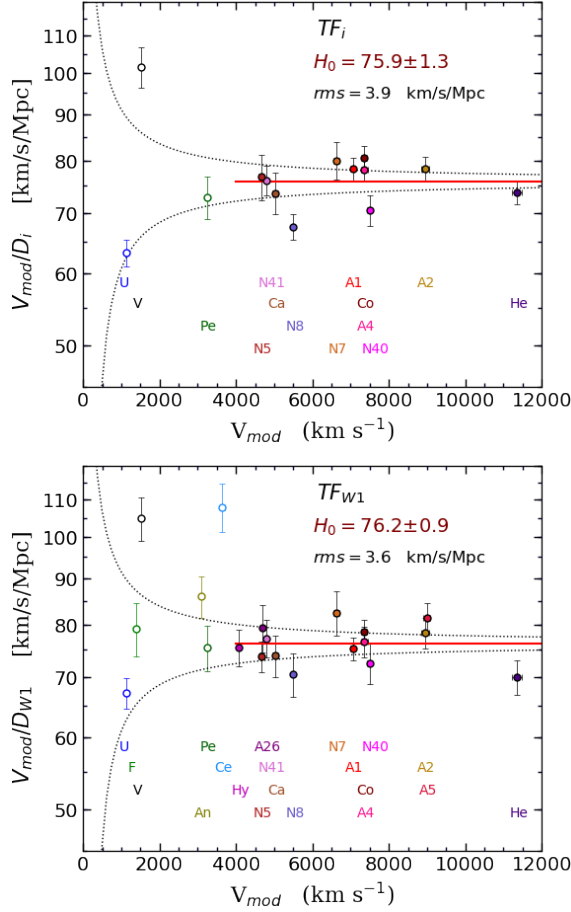


**Figure 29.** Hubble parameter as a function of systemic velocity at *SDSS i* (top) and *WISE W1*-band (bottom). Dotted curves display a  $\pm 200$  km  $s^{-1}$  envelope in velocities. Red horizontal line lies at the log average of the Hubble parameter of clusters beyond  $4000$  km  $s^{-1}$ , those represented by filled circles. Corresponding codes are horizontally placed by velocity. Clusters that do not contribute in the averaging process are denoted by open circles.

$76.2 \pm 0.9$  km  $s^{-1}$  Mpc $^{-1}$  with the rms scatter of  $3.6$  km  $s^{-1}$  Mpc $^{-1}$ .

Fig. 30 and 31 present Hubble parameter derivations from selected formulations labelled in the 4<sup>th</sup> column of Table 9. The cluster moduli determined at optical bands are in good agreement with each other, hence there is no motivation for adjustments to cluster moduli measured at optical passbands. However, the cluster moduli derived from the adjusted models at infrared bands,  $DM_{W1c}$ ,  $DM_{W2c}$ ,  $DM_{W1\mu}$  and  $DM_{W2\mu}$ ,

must receive offsets to be on the same scale as the measured moduli at optical bands. We apply the offset values shown in Fig. 26 to the moduli prior to the calculation of the Hubble parameters.

The Hubble Constant values given in Fig. 30 and 31 are consistent within the claimed statistical uncertainties. The *rms* scatter of the Hubble parameters is larger than the statistical uncertainties owing to clusters peculiar velocities. It may well be that our calibration clusters do not extend to distances such that peculiar velocities are negligible. In addition, any systematic errors in the distances of the zero-point calibrators systematically affect our measurements of  $H_0$ . The main purpose of this study is not to determine the absolute value of  $H_0$  but rather to provide calibrations of the TFR methodology for measuring relative galaxy distances that are consistent across passbands and parameterizations.

## 8. CONCLUSIONS

Every bit of information used in the calibration of luminosity-linewidth relations of spirals might introduce biases and uncertainties in the final derived relations. The main purpose of this calibration program is to determine the peculiar flow of galaxies, thus any unaccounted biases might generate artificial flows suggesting unrealistic cosmological structures. In this program, our main focus is to obtain distances at multiple passbands that are in good agreement with each other and are on the same scale.

The quality of photometry data, the  $\text{H}\alpha$  linewidths, and measurements of inclinations are all important inputs. Corrections for dust extinction can be important toward blueward bands and our formalism to measure dust attenuation (Kourkchi et al. 2019) has been constructed based on the same catalog of spirals used for current study.

The TFR calibrating process has two major steps: definition of slopes at each passband and

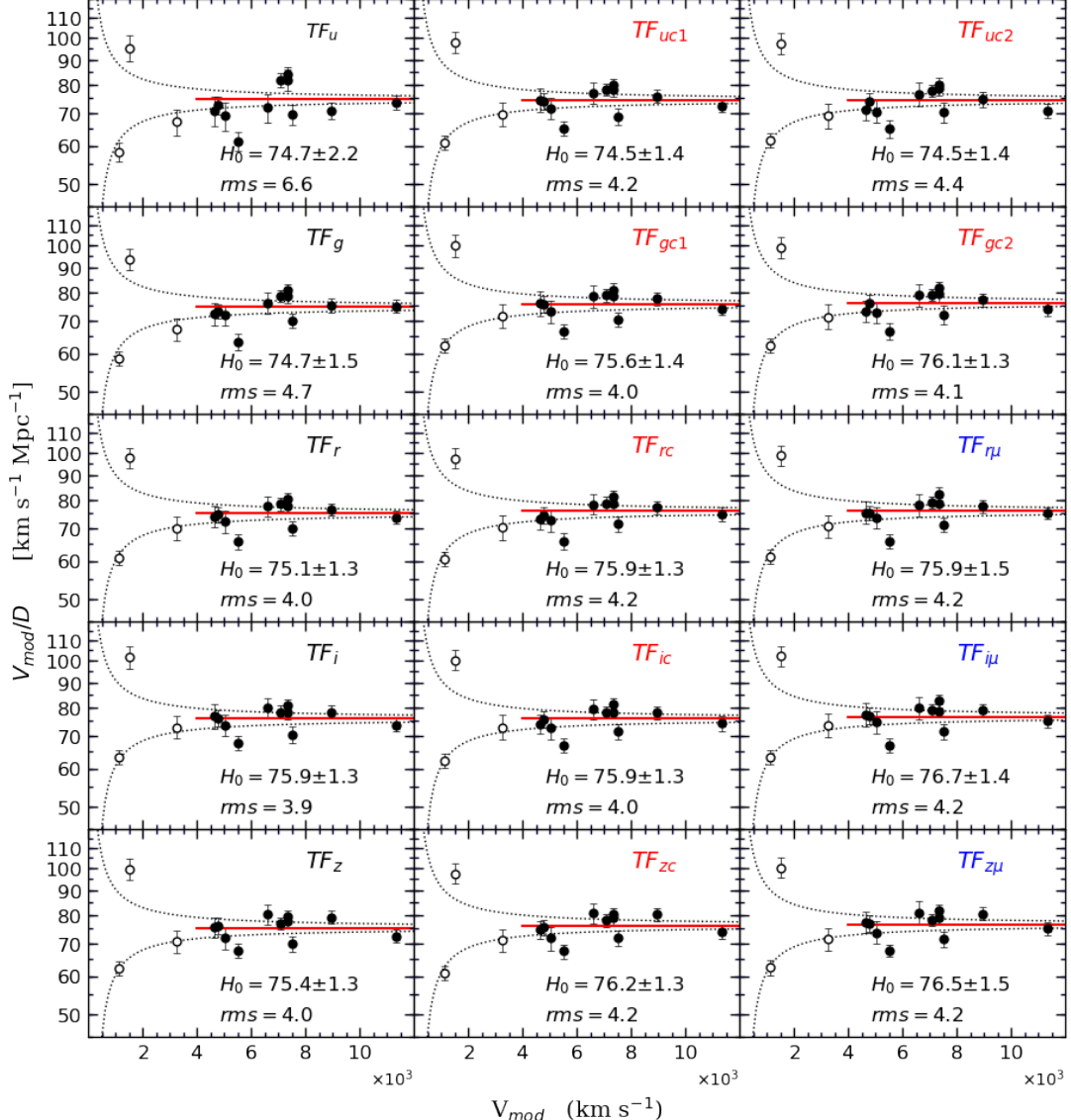


**Figure 30.** Same as Fig. 29 for the optical TFR models presented in Table 9. The code of each model is displayed on the top right corner of each panel.

then establishment of zero-points. The derivations of slopes of the TFR from an ensemble of cluster galaxies is a robust process, but small variations in the properties of galaxies in each cluster influences that cluster’s measured distance relative to the other clusters in the ensemble. For instance, clusters with on average redder galaxies are located at farther distances at redward bands.

Zero point calibrators are the foundation of our calibration process and any systematic in their distances propagates through the entire

process. We separately examined the applicability of two sets of distance calibrators, one using Population I Cepheid variables and the other using Population II Red Giant Branch stars. We find consistency of scales between the two calibrations as manifested in implied values of  $H_0$  using the scale for Cepheids given by Riess et al. (2019) and the scale for Tip of the Red Giant Branch luminosities given by Rizzi et al. (2007). The TRGB scale advocated by Freedman et al. (2019) gives inconsistency with the Cepheid scale. This alternate scaling does cau-

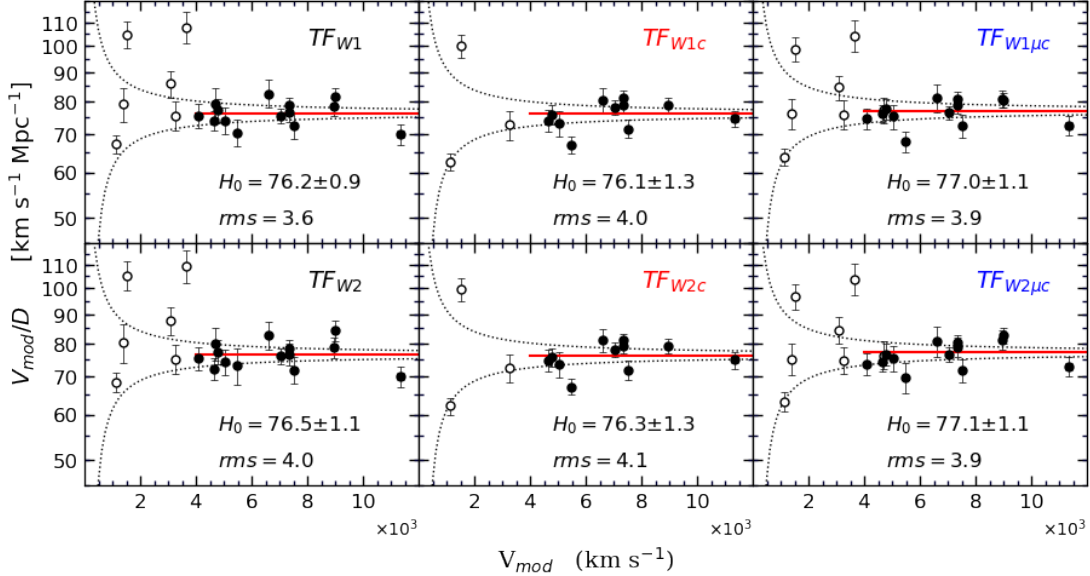


**Figure 31.** Same as Fig. 30 for the infrared ITFR models.

tion us to the plausible existence of zero point systematics at the level of 3%.

We find good agreement in TFR distances measured at *SDSS*  $r$ ,  $i$ , and  $z$  bands and *WISE*  $W1$  and  $W2$  bands. *SDSS*  $u$  and  $g$  bands are less useful for determining TFR distances but the broad span of wavelength coverage they provide provides insight into obscuration and color term issues. Color or surface brightness correlations do not significantly reduced TFR scatter at the optical bands so are not used. However infrared TFR scatter can be substantially reduced with either optical to infrared color or surface brightness terms. The color correlations are strongest but practically are not so useful since the availability of optical information negates the need for an infrared-based measurement. A surface brightness adjustment can be constructed with only infrared photometric information. However, the surface brightness adjusted TFR at  $W1$  and  $W2$  bands must be compensated for offsets due evidently to statistical differences between the surface brightness properties of the zero point calibrators and the full field sample. The offset at the level of 5% is a cautionary example of possible systematics.

The TFR scatter varies with luminosity, such that it is smaller at the bright end and increases toward fainter galaxies. The scatter at the slow rotating, faint end of the TFR can be reduced by accounting for substantial contributions of dark baryons in the form of neutral gas (McGaugh et al. 2000). We have not explored this added complexity. In the redshift regime  $3,000 - 10,000 \text{ km s}^{-1}$  where the numbers in our field sample peak our multi-band measurements will typically render distance with 20% accuracy.

There is slight curvature at the bright end of the TFR, an effect that has been noticed by others. The departure from linearity in the relation between magnitude and log linewidth results in a small bias. Another bias results from asymmetric scatter due to magnitude uncertainties in the regime of the Schechter function exponential cutoff. These two biases act in opposite senses and simulations demonstrate that they roughly but not entirely cancel.

Measurements of distances of clusters at  $V_{mod} > 4000 \text{ km s}^{-1}$  give a preliminary determination of the Hubble constant,  $H_0$ . The sample is small, 11 optical and 14 infrared, and peculiar velocities may not be negligible. In any event,

our measures of  $H_0$  at all passbands based on the adjusted and unadjusted TFR models are consistent. We find  $H_0 = 75.9 \pm 1.3 \text{ km s}^{-1} \text{ Mpc}^{-1}$  and  $H_0 = 76.2 \pm 0.9 \text{ km s}^{-1} \text{ Mpc}^{-1}$  for the unadjusted TFR at  $i$  and  $W1$  bands. With these values, a 3% systematic offset in the distance zero point translates to  $\pm 2.3 \text{ km s}^{-1} \text{ Mpc}^{-1}$  systematic error in the estimated Hubble constant.

In this study, we only considered biases in the distance measures of the clusters, where constituent galaxies are treated as an ensemble. There can be additional biases in measuring the distances of individual field galaxies. This issue is important, especially if different passbands are utilized in different parts of the sky. Even if color terms do not lower the scatter of the calibrated relations at  $r$ ,  $i$  and  $z$  bands, they might still help cancel systematics with application to field galaxies. In a subsequent study, we will investigate the possible ways to reduce biases in the distance measures of field spirals and present formulations for getting consistent distances at optical and infrared bands based on the calibrations provided in this paper.

## ACKNOWLEDGMENTS

We are pleased to acknowledge the citizen participation in scientific research of undergraduate students at the University of Hawaii, members of amateurs astronomy clubs in France at the Planétarium de Vaulx-en-Velin, Association Clair d'étoiles et Brin d'jardin, Société astronomique de Lyon, Club d'astronomie Lyon Ampère, Club d'astronomie des monts du lyonnais, Club d'astronomie de Dijon, and friends who helped us with measuring inclinations of spiral galaxies in our sample.

Support for EK and RBT was provided by NASA through grant number 88NSSC18K0424 and for GA and RBT through grants from the Space Telescope Science Institute. HC acknowl-

edges support from Institut Universitaire de France.

This research has made use of the NASA/IPAC Extragalactic Database<sup>11</sup> which is operated by the Jet Propulsion Laboratory, California Institute of Technology, under contract with the National Aeronautics and Space Administration.

<sup>11</sup> <http://ned.ipac.caltech.edu/>

**Table 10.** Cluster Distances and  $H_0$  Data

Cluster	$V_{mod}$ km s $^{-1}$	TFR	TFR	Ngal	DM $_o$	Bias	$\Delta DM$	DM $_c$	D	$V_{mod}/D$ km s $^{-1}$ Mpc $^{-1}$
(1)	(2)	Band	Model	(3)	mag	mag	mag	mag	Mpc	(11)
		(4)	(5)	(6)	(7)	(8)	(9)	(10)		
Virgo	1516 $\pm$ 45	u	TF $_u$	23	31.01	0.000		31.01 $\pm$ 0.12	15.92 $\pm$ 0.88	95.21 $\pm$ 5.97
		u	TF $_{uc1}$	23	30.95	0.000		30.95 $\pm$ 0.09	15.49 $\pm$ 0.64	97.88 $\pm$ 4.99
		u	TF $_{uc2}$	23	30.96	0.000		30.96 $\pm$ 0.09	15.56 $\pm$ 0.64	97.43 $\pm$ 4.97
		g	TF $_g$	24	31.05	0.001		31.05 $\pm$ 0.09	16.23 $\pm$ 0.67	93.42 $\pm$ 4.76
		g	TF $_{gc1}$	24	30.98	0.000		30.98 $\pm$ 0.09	15.70 $\pm$ 0.65	96.54 $\pm$ 4.92
		g	TF $_{gc2}$	24	31.00	0.000		31.00 $\pm$ 0.09	15.85 $\pm$ 0.66	95.65 $\pm$ 4.88
		r	TF $_r$	24	30.95	0.002		30.95 $\pm$ 0.08	15.50 $\pm$ 0.57	97.81 $\pm$ 4.63
		r	TF $_{rc}$	24	30.96	0.001		30.96 $\pm$ 0.08	15.56 $\pm$ 0.57	97.41 $\pm$ 4.61
		r	TF $_{r\mu}$	24	30.93	0.001		30.93 $\pm$ 0.08	15.35 $\pm$ 0.57	98.75 $\pm$ 4.67
		i	TF $_i$	24	30.87	0.001		30.87 $\pm$ 0.09	14.94 $\pm$ 0.62	101.49 $\pm$ 5.17
		i	TF $_{ic}$	24	30.90	0.001		30.90 $\pm$ 0.08	15.14 $\pm$ 0.56	100.11 $\pm$ 4.74
		i	TF $_{i\mu}$	24	30.86	0.001		30.86 $\pm$ 0.08	14.87 $\pm$ 0.55	101.97 $\pm$ 4.82
		z	TF $_z$	23	30.91	0.002		30.91 $\pm$ 0.09	15.22 $\pm$ 0.63	99.63 $\pm$ 5.08
		z	TF $_{zc}$	23	30.96	0.001		30.96 $\pm$ 0.08	15.57 $\pm$ 0.57	97.40 $\pm$ 4.61
		z	TF $_{z\mu}$	23	30.90	0.000		30.90 $\pm$ 0.08	15.14 $\pm$ 0.56	100.15 $\pm$ 4.74
		W1	TF $_{W1}$	24	30.80	0.000		30.80 $\pm$ 0.10	14.46 $\pm$ 0.67	104.86 $\pm$ 5.75
		W1	TF $_{W1c}$	24	30.86	0.001	0.04	30.90 $\pm$ 0.08	15.14 $\pm$ 0.56	100.11 $\pm$ 4.74
		W1	TF $_{W1\mu}$	24	30.82	-0.001	0.11	30.93 $\pm$ 0.09	15.34 $\pm$ 0.64	98.83 $\pm$ 5.04
		W2	TF $_{W2}$	24	30.79	0.001		30.79 $\pm$ 0.11	14.39 $\pm$ 0.73	105.33 $\pm$ 6.18
		W2	TF $_{W2c}$	24	30.86	0.000	0.06	30.92 $\pm$ 0.08	15.28 $\pm$ 0.56	99.23 $\pm$ 4.69
		W2	TF $_{W2\mu}$	24	30.81	-0.001	0.17	30.98 $\pm$ 0.09	15.70 $\pm$ 0.65	96.58 $\pm$ 4.92
Ursa Major	1141 $\pm$ 13	u	TF $_u$	36	31.46	0.000		31.46 $\pm$ 0.09	19.59 $\pm$ 0.81	58.25 $\pm$ 2.50
		u	TF $_{uc1}$	36	31.36	0.000		31.36 $\pm$ 0.07	18.71 $\pm$ 0.60	60.99 $\pm$ 2.09
		u	TF $_{uc2}$	36	31.34	0.000		31.34 $\pm$ 0.07	18.54 $\pm$ 0.60	61.56 $\pm$ 2.10
		g	TF $_g$	36	31.45	0.003		31.45 $\pm$ 0.07	19.52 $\pm$ 0.63	58.45 $\pm$ 2.00
		g	TF $_{gc1}$	36	31.38	0.002		31.38 $\pm$ 0.07	18.90 $\pm$ 0.61	60.37 $\pm$ 2.06
		g	TF $_{gc2}$	36	31.38	0.001		31.38 $\pm$ 0.07	18.89 $\pm$ 0.61	60.40 $\pm$ 2.07
		r	TF $_r$	36	31.36	0.002		31.36 $\pm$ 0.07	18.73 $\pm$ 0.60	60.93 $\pm$ 2.08
		r	TF $_{rc}$	36	31.38	-0.001		31.38 $\pm$ 0.07	18.88 $\pm$ 0.61	60.45 $\pm$ 2.07
		r	TF $_{r\mu}$	36	31.35	0.000		31.35 $\pm$ 0.07	18.62 $\pm$ 0.60	61.27 $\pm$ 2.09
		i	TF $_i$	36	31.28	0.002		31.28 $\pm$ 0.07	18.05 $\pm$ 0.58	63.21 $\pm$ 2.16
		i	TF $_{ic}$	36	31.31	0.003		31.31 $\pm$ 0.07	18.30 $\pm$ 0.59	62.33 $\pm$ 2.13
		i	TF $_{i\mu}$	36	31.28	0.002		31.28 $\pm$ 0.07	18.05 $\pm$ 0.58	63.23 $\pm$ 2.16
		z	TF $_z$	36	31.31	0.003		31.31 $\pm$ 0.07	18.31 $\pm$ 0.59	62.31 $\pm$ 2.13
		z	TF $_{zc}$	36	31.36	0.002		31.36 $\pm$ 0.07	18.72 $\pm$ 0.60	60.95 $\pm$ 2.08
		z	TF $_{z\mu}$	36	31.31	-0.002		31.31 $\pm$ 0.07	18.26 $\pm$ 0.59	62.48 $\pm$ 2.14
		W1	TF $_{W1}$	36	31.15	0.000		31.15 $\pm$ 0.08	16.98 $\pm$ 0.63	67.19 $\pm$ 2.59
		W1	TF $_{W1c}$	36	31.26	0.000	0.04	31.30 $\pm$ 0.07	18.20 $\pm$ 0.59	62.69 $\pm$ 2.14
		W1	TF $_{W1\mu}$	36	31.15	0.000	0.11	31.26 $\pm$ 0.07	17.86 $\pm$ 0.58	63.87 $\pm$ 2.18
		W2	TF $_{W2}$	36	31.11	0.001		31.11 $\pm$ 0.08	16.68 $\pm$ 0.61	68.41 $\pm$ 2.64
		W2	TF $_{W2c}$	36	31.27	0.000	0.06	31.33 $\pm$ 0.07	18.45 $\pm$ 0.59	61.83 $\pm$ 2.11
		W2	TF $_{W2\mu}$	36	31.11	-0.000	0.17	31.28 $\pm$ 0.08	18.03 $\pm$ 0.66	63.30 $\pm$ 2.44

*Table 10 continued*

Table 10 (continued)

Cluster	$V_{mod}$ km s $^{-1}$	TFR	TFR	Ngal	DM $_o$ mag	Bias mag	$\Delta DM$ mag	DM $_c$ mag	D Mpc	V $_{mod}/D$ km s $^{-1}$ Mpc $^{-1}$
(1)	(2)	Band	Model	(5)	(6)	(7)	(8)	(9)	(10)	(11)
Fornax	1383 $\pm$ 32	W1	TF $_{W1}$	17	31.21	0.002		31.21 $\pm$ 0.14	17.48 $\pm$ 1.13	79.13 $\pm$ 5.42
		W1	TF $_{W1\mu}$	17	31.19	-0.003	0.11	31.30 $\pm$ 0.12	18.17 $\pm$ 1.00	76.11 $\pm$ 4.56
		W2	TF $_{W2}$	17	31.18	0.001		31.18 $\pm$ 0.16	17.23 $\pm$ 1.27	80.27 $\pm$ 6.20
		W2	TF $_{W2\mu}$	17	31.16	-0.005	0.17	31.32 $\pm$ 0.13	18.40 $\pm$ 1.10	75.15 $\pm$ 4.82
Pegasus	3249 $\pm$ 61	u	TF $_u$	24	33.42	0.005		33.42 $\pm$ 0.13	48.41 $\pm$ 2.90	67.12 $\pm$ 4.21
		u	TF $_{uc1}$	24	33.34	0.003		33.34 $\pm$ 0.11	46.62 $\pm$ 2.36	69.69 $\pm$ 3.77
		u	TF $_{uc2}$	22	33.36	0.003		33.36 $\pm$ 0.12	47.06 $\pm$ 2.60	69.03 $\pm$ 4.03
		g	TF $_g$	24	33.42	0.005		33.43 $\pm$ 0.11	48.42 $\pm$ 2.45	67.10 $\pm$ 3.63
		g	TF $_{gc1}$	24	33.35	0.005		33.36 $\pm$ 0.11	46.89 $\pm$ 2.38	69.29 $\pm$ 3.74
		g	TF $_{gc2}$	22	33.36	0.003		33.36 $\pm$ 0.12	47.06 $\pm$ 2.60	69.04 $\pm$ 4.03
		r	TF $_r$	24	33.33	0.003		33.33 $\pm$ 0.11	46.42 $\pm$ 2.35	69.99 $\pm$ 3.78
		r	TF $_{rc}$	22	33.32	-0.001		33.32 $\pm$ 0.12	46.12 $\pm$ 2.55	70.45 $\pm$ 4.11
		r	TF $_{r\mu}$	24	33.31	0.000		33.31 $\pm$ 0.11	45.93 $\pm$ 2.33	70.74 $\pm$ 3.82
		i	TF $_i$	24	33.24	0.004		33.24 $\pm$ 0.11	44.54 $\pm$ 2.26	72.94 $\pm$ 3.94
		i	TF $_{ic}$	22	33.24	0.005		33.24 $\pm$ 0.12	44.56 $\pm$ 2.46	72.91 $\pm$ 4.26
		i	TF $_{i\mu}$	24	33.22	0.003		33.22 $\pm$ 0.11	44.12 $\pm$ 2.24	73.64 $\pm$ 3.98
		z	TF $_z$	24	33.31	0.005		33.31 $\pm$ 0.11	46.02 $\pm$ 2.33	70.59 $\pm$ 3.81
		z	TF $_{zc}$	22	33.30	0.002		33.30 $\pm$ 0.11	45.75 $\pm$ 2.32	71.02 $\pm$ 3.84
		z	TF $_{z\mu}$	24	33.29	-0.003		33.29 $\pm$ 0.11	45.44 $\pm$ 2.30	71.50 $\pm$ 3.86
		W1	TF $_{W1}$	23	33.17	0.001		33.17 $\pm$ 0.12	43.06 $\pm$ 2.38	75.45 $\pm$ 4.40
		W1	TF $_{W1c}$	22	33.21	0.001	0.04	33.25 $\pm$ 0.12	44.69 $\pm$ 2.47	72.69 $\pm$ 4.24
		W1	TF $_{W1\mu}$	23	33.05	-0.000	0.11	33.16 $\pm$ 0.12	42.85 $\pm$ 2.37	75.82 $\pm$ 4.43
		W2	TF $_{W2}$	23	33.18	0.001		33.18 $\pm$ 0.12	43.27 $\pm$ 2.39	75.09 $\pm$ 4.38
		W2	TF $_{W2c}$	22	33.21	0.000	0.06	33.27 $\pm$ 0.12	45.09 $\pm$ 2.49	72.06 $\pm$ 4.21
		W2	TF $_{W2\mu}$	23	33.02	0.000	0.17	33.19 $\pm$ 0.11	43.46 $\pm$ 2.20	74.76 $\pm$ 4.04
Centaurus	3645 $\pm$ 56	W1	TF $_{W1}$	22	32.63	0.012		32.64 $\pm$ 0.13	33.76 $\pm$ 2.02	107.96 $\pm$ 6.67
		W1	TF $_{W1\mu}$	22	32.62	-0.013	0.11	32.72 $\pm$ 0.13	34.94 $\pm$ 2.09	104.33 $\pm$ 6.45
		W2	TF $_{W2}$	22	32.60	0.013		32.61 $\pm$ 0.14	33.31 $\pm$ 2.15	109.44 $\pm$ 7.25
		W2	TF $_{W2\mu}$	22	32.58	-0.024	0.17	32.73 $\pm$ 0.13	35.10 $\pm$ 2.10	103.86 $\pm$ 6.42
Antlia	3103 $\pm$ 53	W1	TF $_{W1}$	17	32.78	0.009		32.79 $\pm$ 0.11	36.12 $\pm$ 1.83	85.90 $\pm$ 4.59
		W1	TF $_{W1\mu}$	17	32.72	-0.007	0.11	32.82 $\pm$ 0.10	36.69 $\pm$ 1.69	84.58 $\pm$ 4.15
		W2	TF $_{W2}$	17	32.74	0.006		32.75 $\pm$ 0.12	35.42 $\pm$ 1.96	87.60 $\pm$ 5.07
		W2	TF $_{W2\mu}$	17	32.67	-0.013	0.17	32.83 $\pm$ 0.11	36.77 $\pm$ 1.86	84.39 $\pm$ 4.51
Hydra	4084 $\pm$ 44	W1	TF $_{W1}$	44	33.66	0.008		33.67 $\pm$ 0.10	54.14 $\pm$ 2.49	75.43 $\pm$ 3.57
		W1	TF $_{W1\mu}$	44	33.59	-0.007	0.11	33.69 $\pm$ 0.09	54.79 $\pm$ 2.27	74.54 $\pm$ 3.19
		W2	TF $_{W2}$	44	33.67	0.004		33.67 $\pm$ 0.10	54.31 $\pm$ 2.50	75.19 $\pm$ 3.56
		W2	TF $_{W2\mu}$	44	33.56	-0.010	0.17	33.72 $\pm$ 0.09	55.47 $\pm$ 2.30	73.63 $\pm$ 3.15
Abell 262	4684 $\pm$ 50	W1	TF $_{W1}$	54	33.85	0.006		33.86 $\pm$ 0.13	59.03 $\pm$ 3.53	79.34 $\pm$ 4.83
		W1	TF $_{W1\mu}$	54	33.81	-0.005	0.11	33.91 $\pm$ 0.11	60.67 $\pm$ 3.07	77.21 $\pm$ 4.00
		W2	TF $_{W2}$	54	33.84	0.003		33.84 $\pm$ 0.14	58.70 $\pm$ 3.78	79.79 $\pm$ 5.21
		W2	TF $_{W2\mu}$	54	33.78	-0.009	0.17	33.94 $\pm$ 0.12	61.41 $\pm$ 3.39	76.27 $\pm$ 4.29
NGC507	4660 $\pm$ 64	u	TF $_u$	20	34.07	0.027		34.10 $\pm$ 0.15	65.98 $\pm$ 4.56	70.63 $\pm$ 4.97
		u	TF $_{uc1}$	20	33.97	0.014		33.98 $\pm$ 0.12	62.64 $\pm$ 3.46	74.40 $\pm$ 4.24
		u	TF $_{uc2}$	19	34.06	0.018		34.08 $\pm$ 0.11	65.41 $\pm$ 3.31	71.25 $\pm$ 3.74

Table 10 continued

Table 10 (continued)

Cluster	$V_{mod}$ km s <sup>-1</sup>	TFR	TFR	Ngal	DM <sub>o</sub>	Bias	$\Delta DM$	DM <sub>c</sub>	D	V <sub>mod</sub> /D
(1)	(2)	Band	Model	(5)	mag	mag	mag	mag	Mpc	km s <sup>-1</sup> Mpc <sup>-1</sup>
		(3)	(4)	(6)	(7)	(8)		(9)	(10)	(11)
A	4792±53	g	TF <sub>g</sub>	20	34.03	0.014		34.04±0.11	64.40±3.26	72.36±3.80
		g	TF <sub>gc1</sub>	20	33.99	0.019		34.01±0.12	63.37±3.50	73.54±4.19
		g	TF <sub>gc2</sub>	19	34.07	0.019		34.09±0.10	65.72±3.03	70.90±3.41
		r	TF <sub>r</sub>	20	33.98	0.014		33.99±0.11	62.93±3.19	74.05±3.89
		r	TF <sub>rc</sub>	19	34.02	0.003		34.02±0.10	63.75±2.94	73.09±3.51
		r	TF <sub>rμ</sub>	20	33.95	0.005		33.95±0.11	61.80±3.13	75.41±3.96
		i	TF <sub>i</sub>	20	33.90	0.017		33.92±0.12	60.73±3.36	76.73±4.37
		i	TF <sub>ic</sub>	19	33.97	0.021		33.99±0.09	62.84±2.60	74.15±3.24
		i	TF <sub>iμ</sub>	20	33.88	0.017		33.90±0.12	60.17±3.32	77.45±4.41
		z	TF <sub>z</sub>	20	33.93	0.018		33.95±0.10	61.60±2.84	75.65±3.64
		z	TF <sub>zc</sub>	19	33.97	0.005		33.97±0.09	62.37±2.59	74.71±3.26
		z	TF <sub>zμ</sub>	20	33.90	-0.003		33.90±0.10	60.17±2.77	77.45±3.72
		W1	TF <sub>W1</sub>	22	33.99	0.012		34.00±0.08	63.15±2.33	73.79±2.90
		W1	TF <sub>W1c</sub>	19	33.93	0.025	0.04	33.99±0.09	62.94±2.61	74.04±3.23
		W1	TF <sub>W1μ</sub>	22	33.84	-0.015	0.11	33.94±0.07	61.25±1.97	76.08±2.67
		W2	TF <sub>W2</sub>	22	34.04	0.013		34.05±0.09	64.65±2.68	72.08±3.15
		W2	TF <sub>W2c</sub>	19	33.92	0.004	0.06	33.98±0.09	62.65±2.60	74.39±3.25
		W2	TF <sub>W2μ</sub>	22	33.84	-0.023	0.17	33.99±0.08	62.73±2.31	74.28±2.92
NGC410	4792±53	u	TF <sub>u</sub>	33	34.09	0.008		34.10±0.09	66.02±2.74	72.58±3.11
		u	TF <sub>uc1</sub>	33	34.05	0.006		34.06±0.08	64.74±2.39	74.02±2.85
		u	TF <sub>uc2</sub>	31	34.05	0.006		34.06±0.08	64.76±2.39	74.00±2.85
		g	TF <sub>g</sub>	33	34.07	0.010		34.08±0.07	65.45±2.11	73.21±2.50
		g	TF <sub>gc1</sub>	33	34.06	0.013		34.07±0.08	65.26±2.40	73.43±2.82
		g	TF <sub>gc2</sub>	31	34.06	0.010		34.07±0.08	65.16±2.40	73.54±2.83
		r	TF <sub>r</sub>	33	34.03	0.007		34.04±0.08	64.19±2.36	74.65±2.87
		r	TF <sub>rc</sub>	31	34.04	-0.000		34.04±0.08	64.26±2.37	74.57±2.87
		r	TF <sub>rμ</sub>	33	34.02	0.002		34.02±0.07	63.73±2.05	75.19±2.56
		i	TF <sub>i</sub>	33	33.99	0.006		34.00±0.08	62.98±2.32	76.08±2.93
		i	TF <sub>ic</sub>	31	34.00	0.007		34.01±0.08	63.31±2.33	75.69±2.91
		i	TF <sub>iμ</sub>	33	33.97	0.005		33.98±0.08	62.38±2.30	76.82±2.95
		z	TF <sub>z</sub>	33	33.99	0.009		34.00±0.08	63.08±2.32	75.97±2.92
		z	TF <sub>zc</sub>	31	34.01	0.003		34.01±0.07	63.48±2.05	75.49±2.57
		z	TF <sub>zμ</sub>	33	33.98	-0.004		33.98±0.08	62.41±2.30	76.79±2.95
		W1	TF <sub>W1</sub>	31	33.96	0.004		33.96±0.10	62.05±2.86	77.23±3.66
		W1	TF <sub>W1c</sub>	31	33.96	0.005	0.04	34.00±0.08	63.24±2.33	75.78±2.91
		W1	TF <sub>W1μ</sub>	31	33.85	-0.004	0.11	33.96±0.09	61.84±2.56	77.49±3.32
		W2	TF <sub>W2</sub>	31	33.96	0.003		33.96±0.10	62.02±2.86	77.27±3.66
		W2	TF <sub>W2c</sub>	31	33.96	0.001	0.06	34.02±0.08	63.71±2.35	75.22±2.89
		W2	TF <sub>W2μ</sub>	31	33.82	-0.007	0.17	33.98±0.09	62.61±2.60	76.54±3.28
Cancer	5025±71	u	TF <sub>u</sub>	18	34.24	0.071		34.31±0.14	72.80±4.69	69.02±4.56
		u	TF <sub>uc1</sub>	18	34.19	0.040		34.23±0.11	70.15±3.55	71.63±3.77
		u	TF <sub>uc2</sub>	17	34.22	0.045		34.27±0.11	71.30±3.61	70.48±3.71
		g	TF <sub>g</sub>	18	34.19	0.035		34.23±0.10	69.99±3.22	71.80±3.46
		g	TF <sub>gc1</sub>	18	34.20	0.057		34.26±0.11	71.02±3.60	70.76±3.72

Table 10 continued

Table 10 (continued)

Cluster	$V_{mod}$ km s $^{-1}$	TFR	TFR	Ngal	DM $_o$ mag	Bias mag	$\Delta DM$ mag	DM $_c$ mag	D Mpc	V $_{mod}/D$ km s $^{-1}$ Mpc $^{-1}$
(1)	(2)	Band	Model	(5)	(6)	(7)	(8)	(9)	(10)	(11)
(3)	(4)									
NGC80	5499 $\pm$ 42	g	TF $_{gc2}$	17	34.21	0.056		34.27 $\pm$ 0.10	71.31 $\pm$ 3.28	70.46 $\pm$ 3.39
		r	TF $_r$	18	34.18	0.032		34.21 $\pm$ 0.11	69.56 $\pm$ 3.52	72.24 $\pm$ 3.80
		r	TF $_{rc}$	17	34.19	0.012		34.20 $\pm$ 0.11	69.25 $\pm$ 3.51	72.56 $\pm$ 3.82
		r	TF $_{r\mu}$	18	34.15	0.019		34.17 $\pm$ 0.11	68.21 $\pm$ 3.46	73.67 $\pm$ 3.87
		i	TF $_i$	18	34.14	0.030		34.17 $\pm$ 0.11	68.24 $\pm$ 3.46	73.64 $\pm$ 3.87
		i	TF $_{ic}$	17	34.16	0.038		34.20 $\pm$ 0.11	69.13 $\pm$ 3.50	72.69 $\pm$ 3.82
		i	TF $_{i\mu}$	18	34.11	0.032		34.14 $\pm$ 0.11	67.35 $\pm$ 3.41	74.61 $\pm$ 3.92
		z	TF $_z$	18	34.20	0.027		34.23 $\pm$ 0.11	70.04 $\pm$ 3.55	71.74 $\pm$ 3.77
		z	TF $_{zc}$	17	34.22	0.007		34.23 $\pm$ 0.12	70.05 $\pm$ 3.87	71.73 $\pm$ 4.09
		z	TF $_{z\mu}$	18	34.17	-0.003		34.17 $\pm$ 0.11	68.14 $\pm$ 3.45	73.74 $\pm$ 3.88
		W1	TF $_{W1}$	17	34.15	0.012		34.16 $\pm$ 0.11	67.98 $\pm$ 3.44	73.92 $\pm$ 3.89
		W1	TF $_{W1c}$	17	34.12	0.026	0.04	34.19 $\pm$ 0.11	68.73 $\pm$ 3.48	73.11 $\pm$ 3.85
		W1	TF $_{W1\mu}$	17	34.03	-0.015	0.11	34.12 $\pm$ 0.10	66.82 $\pm$ 3.08	75.20 $\pm$ 3.62
		W2	TF $_{W2}$	17	34.14	0.013		34.15 $\pm$ 0.11	67.70 $\pm$ 3.43	74.22 $\pm$ 3.90
		W2	TF $_{W2c}$	17	34.12	0.006	0.06	34.19 $\pm$ 0.11	68.73 $\pm$ 3.48	73.12 $\pm$ 3.85
		W2	TF $_{W2\mu}$	17	33.98	-0.027	0.17	34.12 $\pm$ 0.11	66.76 $\pm$ 3.38	75.26 $\pm$ 3.96
NGC70	6619 $\pm$ 80	u	TF $_u$	14	34.72	0.046		34.77 $\pm$ 0.10	89.77 $\pm$ 4.13	61.25 $\pm$ 2.86
		u	TF $_{uc1}$	14	34.61	0.024		34.63 $\pm$ 0.07	84.47 $\pm$ 2.72	65.10 $\pm$ 2.16
		u	TF $_{uc2}$	13	34.61	0.026		34.64 $\pm$ 0.09	84.57 $\pm$ 3.51	65.02 $\pm$ 2.74
		g	TF $_g$	14	34.67	0.024		34.69 $\pm$ 0.08	86.87 $\pm$ 3.20	63.30 $\pm$ 2.38
		g	TF $_{gc1}$	14	34.62	0.035		34.66 $\pm$ 0.07	85.32 $\pm$ 2.75	64.45 $\pm$ 2.14
		g	TF $_{gc2}$	13	34.62	0.032		34.65 $\pm$ 0.08	85.20 $\pm$ 3.14	64.54 $\pm$ 2.43
		r	TF $_r$	14	34.59	0.023		34.61 $\pm$ 0.08	83.67 $\pm$ 3.08	65.72 $\pm$ 2.47
		r	TF $_{rc}$	13	34.60	0.006		34.61 $\pm$ 0.08	83.42 $\pm$ 3.07	65.92 $\pm$ 2.48
		r	TF $_{r\mu}$	14	34.60	0.010		34.61 $\pm$ 0.07	83.58 $\pm$ 2.69	65.80 $\pm$ 2.18
		i	TF $_i$	14	34.53	0.023		34.55 $\pm$ 0.07	81.39 $\pm$ 2.62	67.57 $\pm$ 2.24
		i	TF $_{ic}$	13	34.55	0.027		34.58 $\pm$ 0.07	82.29 $\pm$ 2.65	66.82 $\pm$ 2.21
		i	TF $_{i\mu}$	14	34.55	0.024		34.57 $\pm$ 0.07	82.17 $\pm$ 2.65	66.92 $\pm$ 2.22
		z	TF $_z$	14	34.53	0.022		34.55 $\pm$ 0.07	81.36 $\pm$ 2.62	67.59 $\pm$ 2.24
		z	TF $_{zc}$	13	34.55	0.006		34.56 $\pm$ 0.07	81.50 $\pm$ 2.63	67.47 $\pm$ 2.24
		z	TF $_{z\mu}$	14	34.55	-0.002		34.55 $\pm$ 0.06	81.20 $\pm$ 2.24	67.72 $\pm$ 1.94
		W1	TF $_{W1}$	13	34.45	0.011		34.46 $\pm$ 0.12	78.02 $\pm$ 4.31	70.49 $\pm$ 3.93
		W1	TF $_{W1c}$	13	34.50	0.029	0.04	34.57 $\pm$ 0.07	82.01 $\pm$ 2.64	67.06 $\pm$ 2.22
		W1	TF $_{W1\mu}$	13	34.45	-0.019	0.11	34.54 $\pm$ 0.09	80.93 $\pm$ 3.35	67.94 $\pm$ 2.86
		W2	TF $_{W2}$	13	34.37	0.012		34.38 $\pm$ 0.16	75.25 $\pm$ 5.54	73.08 $\pm$ 5.41
		W2	TF $_{W2c}$	13	34.51	0.007	0.06	34.58 $\pm$ 0.07	82.29 $\pm$ 2.65	66.82 $\pm$ 2.21
		W2	TF $_{W2\mu}$	13	34.35	-0.033	0.17	34.49 $\pm$ 0.13	78.95 $\pm$ 4.73	69.66 $\pm$ 4.20

Table 10 continued

Table 10 (continued)

Cluster	$V_{mod}$ km s $^{-1}$	TFR	TFR	Ngal	DM $_o$ mag	Bias mag	$\Delta DM$ mag	DM $_c$ mag	D Mpc	V $_{mod}/D$ km s $^{-1}$ Mpc $^{-1}$
(1)	(2)	Band	Model	(5)	(6)	(7)	(8)	(9)	(10)	(11)
Abell 1367	7060 $\pm$ 61	r	TF $_{rc}$	11	34.62	0.012		34.63 $\pm$ 0.10	84.42 $\pm$ 3.89	78.41 $\pm$ 3.73
		r	TF $_{r\mu}$	11	34.62	0.022		34.64 $\pm$ 0.11	84.80 $\pm$ 4.30	78.05 $\pm$ 4.06
		i	TF $_i$	11	34.56	0.028		34.59 $\pm$ 0.10	82.73 $\pm$ 3.81	80.01 $\pm$ 3.81
		i	TF $_{ic}$	11	34.56	0.040		34.60 $\pm$ 0.10	83.18 $\pm$ 3.83	79.57 $\pm$ 3.79
		i	TF $_{i\mu}$	11	34.56	0.031		34.59 $\pm$ 0.11	82.82 $\pm$ 4.20	79.92 $\pm$ 4.16
		z	TF $_z$	11	34.56	0.022		34.58 $\pm$ 0.10	82.49 $\pm$ 3.80	80.24 $\pm$ 3.82
		z	TF $_{zc}$	11	34.56	0.007		34.57 $\pm$ 0.10	81.92 $\pm$ 3.77	80.80 $\pm$ 3.85
		z	TF $_{z\mu}$	11	34.57	-0.010		34.56 $\pm$ 0.11	81.67 $\pm$ 4.14	81.04 $\pm$ 4.22
		W1	TF $_{W1}$	11	34.52	0.002		34.52 $\pm$ 0.12	80.23 $\pm$ 4.43	82.50 $\pm$ 4.67
		W1	TF $_{W1c}$	11	34.50	0.037	0.04	34.58 $\pm$ 0.10	82.31 $\pm$ 3.79	80.42 $\pm$ 3.83
		W1	TF $_{W1\mu}$	11	34.48	-0.031	0.11	34.56 $\pm$ 0.12	81.61 $\pm$ 4.51	81.11 $\pm$ 4.59
		W2	TF $_{W2}$	11	34.51	0.004		34.51 $\pm$ 0.12	79.96 $\pm$ 4.42	82.78 $\pm$ 4.68
		W2	TF $_{W2c}$	11	34.50	0.009	0.06	34.57 $\pm$ 0.10	81.98 $\pm$ 3.78	80.74 $\pm$ 3.84
		W2	TF $_{W2\mu}$	11	34.45	-0.051	0.17	34.57 $\pm$ 0.13	82.01 $\pm$ 4.91	80.71 $\pm$ 4.93
		u	TF $_u$	68	34.67	0.008		34.68 $\pm$ 0.07	86.20 $\pm$ 2.78	81.90 $\pm$ 2.73
		u	TF $_{uc1}$	68	34.77	0.008		34.78 $\pm$ 0.06	90.28 $\pm$ 2.49	78.21 $\pm$ 2.26
		u	TF $_{uc2}$	62	34.78	0.009		34.79 $\pm$ 0.06	90.74 $\pm$ 2.51	77.81 $\pm$ 2.25
		g	TF $_g$	68	34.75	0.012		34.76 $\pm$ 0.06	89.61 $\pm$ 2.48	78.78 $\pm$ 2.28
		g	TF $_{gc1}$	68	34.81	0.019		34.83 $\pm$ 0.06	92.41 $\pm$ 2.55	76.40 $\pm$ 2.21
		g	TF $_{gc2}$	62	34.81	0.015		34.83 $\pm$ 0.06	92.26 $\pm$ 2.55	76.52 $\pm$ 2.22
		r	TF $_r$	68	34.76	0.010		34.77 $\pm$ 0.06	89.97 $\pm$ 2.49	78.47 $\pm$ 2.27
		r	TF $_{rc}$	62	34.76	0.001		34.76 $\pm$ 0.06	89.57 $\pm$ 2.47	78.82 $\pm$ 2.28
		r	TF $_{r\mu}$	68	34.75	0.003		34.75 $\pm$ 0.06	89.25 $\pm$ 2.47	79.10 $\pm$ 2.29
		i	TF $_i$	68	34.76	0.013		34.77 $\pm$ 0.06	90.08 $\pm$ 2.49	78.37 $\pm$ 2.27
		i	TF $_{ic}$	62	34.76	0.015		34.78 $\pm$ 0.06	90.18 $\pm$ 2.49	78.29 $\pm$ 2.27
		i	TF $_{i\mu}$	68	34.74	0.013		34.75 $\pm$ 0.06	89.23 $\pm$ 2.47	79.12 $\pm$ 2.29
		z	TF $_z$	68	34.80	0.011		34.81 $\pm$ 0.06	91.64 $\pm$ 2.53	77.04 $\pm$ 2.23
		z	TF $_{zc}$	62	34.78	0.003		34.78 $\pm$ 0.06	90.50 $\pm$ 2.50	78.01 $\pm$ 2.26
		z	TF $_{z\mu}$	68	34.78	-0.004		34.78 $\pm$ 0.06	90.20 $\pm$ 2.49	78.27 $\pm$ 2.27
		W1	TF $_{W1}$	62	34.85	0.011		34.86 $\pm$ 0.06	93.80 $\pm$ 2.59	75.26 $\pm$ 2.18
		W1	TF $_{W1c}$	62	34.73	0.015	0.04	34.79 $\pm$ 0.06	90.58 $\pm$ 2.50	77.94 $\pm$ 2.26
		W1	TF $_{W1\mu}$	62	34.73	-0.009	0.11	34.83 $\pm$ 0.06	92.50 $\pm$ 2.56	76.32 $\pm$ 2.21
		W2	TF $_{W2}$	62	34.83	0.010		34.84 $\pm$ 0.07	92.88 $\pm$ 2.99	76.01 $\pm$ 2.54
		W2	TF $_{W2c}$	62	34.73	0.003	0.06	34.79 $\pm$ 0.06	90.90 $\pm$ 2.51	77.67 $\pm$ 2.25
		W2	TF $_{W2\mu}$	62	34.67	-0.016	0.17	34.82 $\pm$ 0.06	92.23 $\pm$ 2.55	76.55 $\pm$ 2.22
Coma	7352 $\pm$ 70	u	TF $_u$	79	34.68	0.027		34.71 $\pm$ 0.07	87.40 $\pm$ 2.82	84.12 $\pm$ 2.83
		u	TF $_{uc1}$	79	34.80	0.020		34.82 $\pm$ 0.06	92.05 $\pm$ 2.54	79.87 $\pm$ 2.33
		u	TF $_{uc2}$	75	34.79	0.022		34.81 $\pm$ 0.06	91.70 $\pm$ 2.53	80.17 $\pm$ 2.34
		g	TF $_g$	79	34.78	0.012		34.79 $\pm$ 0.06	90.87 $\pm$ 2.51	80.91 $\pm$ 2.36
		g	TF $_{gc1}$	79	34.84	0.019		34.86 $\pm$ 0.06	93.70 $\pm$ 2.59	78.46 $\pm$ 2.29
		g	TF $_{gc2}$	75	34.83	0.015		34.85 $\pm$ 0.06	93.12 $\pm$ 2.57	78.95 $\pm$ 2.31
		r	TF $_r$	79	34.80	0.010		34.81 $\pm$ 0.06	91.64 $\pm$ 2.53	80.23 $\pm$ 2.34
		r	TF $_{rc}$	75	34.78	0.001		34.78 $\pm$ 0.06	90.39 $\pm$ 2.50	81.34 $\pm$ 2.38

Table 10 continued

Table 10 (continued)

Cluster	$V_{mod}$ km s $^{-1}$	TFR	TFR	Ngal	DM $_o$ mag	Bias mag	$\Delta DM$ mag	DM $_c$ mag	D Mpc	V $_{mod}/D$ km s $^{-1}$ Mpc $^{-1}$
(1)	(2)	Band	Model	(5)	(6)	(7)	(8)	(9)	(10)	(11)
		i	TF $_i$	79	34.79	0.009		34.80 $\pm$ 0.06	91.16 $\pm$ 2.52	80.65 $\pm$ 2.36
		i	TF $_{ic}$	75	34.77	0.010		34.78 $\pm$ 0.06	90.38 $\pm$ 2.50	81.34 $\pm$ 2.38
		i	TF $_{i\mu}$	79	34.74	0.008		34.75 $\pm$ 0.06	89.04 $\pm$ 2.46	82.57 $\pm$ 2.41
		z	TF $_z$	79	34.82	0.008		34.83 $\pm$ 0.06	92.38 $\pm$ 2.55	79.58 $\pm$ 2.33
		z	TF $_{zc}$	75	34.80	0.003		34.80 $\pm$ 0.06	91.31 $\pm$ 2.52	80.52 $\pm$ 2.35
		z	TF $_{z\mu}$	79	34.77	-0.004		34.77 $\pm$ 0.06	89.80 $\pm$ 2.48	81.87 $\pm$ 2.39
		W1	TF $_{W1}$	75	34.85	0.004		34.85 $\pm$ 0.06	93.49 $\pm$ 2.58	78.64 $\pm$ 2.30
		W1	TF $_{W1c}$	75	34.74	0.004	0.04	34.78 $\pm$ 0.06	90.54 $\pm$ 2.50	81.20 $\pm$ 2.37
		W1	TF $_{W1\mu}$	75	34.69	-0.004	0.11	34.80 $\pm$ 0.06	91.05 $\pm$ 2.52	80.74 $\pm$ 2.36
		W2	TF $_{W2}$	75	34.86	0.002		34.86 $\pm$ 0.07	93.86 $\pm$ 3.03	78.33 $\pm$ 2.63
		W2	TF $_{W2c}$	75	34.74	0.001	0.06	34.80 $\pm$ 0.06	91.23 $\pm$ 2.52	80.59 $\pm$ 2.36
		W2	TF $_{W2\mu}$	75	34.64	-0.005	0.17	34.80 $\pm$ 0.06	91.40 $\pm$ 2.53	80.44 $\pm$ 2.35
Abell 400	7357 $\pm$ 85	u	TF $_u$	21	34.72	0.048		34.77 $\pm$ 0.10	89.88 $\pm$ 4.14	81.85 $\pm$ 3.89
		u	TF $_{uc1}$	21	34.84	0.032		34.87 $\pm$ 0.06	94.26 $\pm$ 2.60	78.05 $\pm$ 2.34
		u	TF $_{uc2}$	20	34.82	0.034		34.85 $\pm$ 0.07	93.51 $\pm$ 3.01	78.68 $\pm$ 2.69
		g	TF $_g$	21	34.82	0.031		34.85 $\pm$ 0.07	93.36 $\pm$ 3.01	78.81 $\pm$ 2.70
		g	TF $_{gc1}$	21	34.88	0.049		34.93 $\pm$ 0.06	96.80 $\pm$ 2.67	76.00 $\pm$ 2.28
		g	TF $_{gc2}$	20	34.86	0.047		34.91 $\pm$ 0.07	95.81 $\pm$ 3.09	76.79 $\pm$ 2.63
		r	TF $_r$	21	34.85	0.030		34.88 $\pm$ 0.06	94.63 $\pm$ 2.61	77.74 $\pm$ 2.33
		r	TF $_{rc}$	20	34.85	0.010		34.86 $\pm$ 0.06	93.78 $\pm$ 2.59	78.45 $\pm$ 2.35
		r	TF $_{r\mu}$	21	34.84	0.016		34.86 $\pm$ 0.06	93.60 $\pm$ 2.59	78.60 $\pm$ 2.35
		i	TF $_i$	21	34.84	0.029		34.87 $\pm$ 0.06	94.15 $\pm$ 2.60	78.14 $\pm$ 2.34
		i	TF $_{ic}$	20	34.83	0.035		34.86 $\pm$ 0.06	93.97 $\pm$ 2.60	78.29 $\pm$ 2.34
		i	TF $_{i\mu}$	21	34.82	0.030		34.85 $\pm$ 0.06	93.33 $\pm$ 2.58	78.83 $\pm$ 2.36
		z	TF $_z$	21	34.85	0.027		34.88 $\pm$ 0.06	94.48 $\pm$ 2.61	77.87 $\pm$ 2.33
		z	TF $_{zc}$	20	34.84	0.007		34.85 $\pm$ 0.06	93.19 $\pm$ 2.57	78.95 $\pm$ 2.36
		z	TF $_{z\mu}$	21	34.84	-0.002		34.84 $\pm$ 0.06	92.80 $\pm$ 2.56	79.28 $\pm$ 2.37
		W1	TF $_{W1}$	23	34.90	0.011		34.91 $\pm$ 0.08	96.00 $\pm$ 3.54	76.63 $\pm$ 2.96
		W1	TF $_{W1c}$	20	34.80	0.016	0.04	34.86 $\pm$ 0.06	93.60 $\pm$ 2.59	78.60 $\pm$ 2.35
		W1	TF $_{W1\mu}$	23	34.75	-0.009	0.11	34.85 $\pm$ 0.07	93.35 $\pm$ 3.01	78.81 $\pm$ 2.70
		W2	TF $_{W2}$	23	34.90	0.011		34.91 $\pm$ 0.09	95.97 $\pm$ 3.98	76.66 $\pm$ 3.30
		W2	TF $_{W2c}$	20	34.79	0.003	0.06	34.85 $\pm$ 0.06	93.46 $\pm$ 2.58	78.72 $\pm$ 2.36
		W2	TF $_{W2\mu}$	23	34.70	-0.017	0.17	34.85 $\pm$ 0.08	93.47 $\pm$ 3.44	78.71 $\pm$ 3.04
NGC4065	7501 $\pm$ 63	u	TF $_u$	14	35.11	0.055		35.16 $\pm$ 0.10	107.89 $\pm$ 4.97	69.52 $\pm$ 3.25
		u	TF $_{uc1}$	14	35.15	0.033		35.18 $\pm$ 0.08	108.80 $\pm$ 4.01	68.95 $\pm$ 2.61
		u	TF $_{uc2}$	12	35.11	0.035		35.15 $\pm$ 0.10	106.91 $\pm$ 4.92	70.16 $\pm$ 3.28
		g	TF $_g$	14	35.12	0.028		35.15 $\pm$ 0.07	107.04 $\pm$ 3.45	70.08 $\pm$ 2.33
		g	TF $_{gc1}$	14	35.16	0.044		35.20 $\pm$ 0.07	109.83 $\pm$ 3.54	68.30 $\pm$ 2.28
		g	TF $_{gc2}$	12	35.12	0.040		35.16 $\pm$ 0.09	107.65 $\pm$ 4.46	69.68 $\pm$ 2.95
		r	TF $_r$	14	35.12	0.026		35.15 $\pm$ 0.07	106.97 $\pm$ 3.45	70.12 $\pm$ 2.34
		r	TF $_{rc}$	12	35.10	0.008		35.11 $\pm$ 0.08	105.09 $\pm$ 3.87	71.37 $\pm$ 2.70
		r	TF $_{r\mu}$	14	35.10	0.013		35.11 $\pm$ 0.07	105.32 $\pm$ 3.40	71.22 $\pm$ 2.37
		i	TF $_i$	14	35.11	0.025		35.14 $\pm$ 0.08	106.43 $\pm$ 3.92	70.48 $\pm$ 2.66
		i	TF $_{ic}$	12	35.08	0.029		35.11 $\pm$ 0.08	105.16 $\pm$ 3.87	71.33 $\pm$ 2.70

Table 10 continued

Table 10 (continued)

Cluster	$V_{mod}$ km s $^{-1}$	TFR	TFR	Ngal	DM $_o$ mag	Bias mag	$\Delta DM$ mag	DM $_c$ mag	D Mpc	V $_{mod}/D$ km s $^{-1}$ Mpc $^{-1}$
(1)	(2)	Band	Model	(5)	(6)	(7)	(8)	(9)	(10)	(11)
Abell 539	8995 $\pm$ 87	i	TF $_{i\mu}$	14	35.08	0.026		35.11 $\pm$ 0.08	104.99 $\pm$ 3.87	71.45 $\pm$ 2.70
		z	TF $_z$	14	35.13	0.024		35.15 $\pm$ 0.08	107.35 $\pm$ 3.95	69.87 $\pm$ 2.64
		z	TF $_{zc}$	12	35.09	0.006		35.10 $\pm$ 0.08	104.52 $\pm$ 3.85	71.77 $\pm$ 2.71
		z	TF $_{z\mu}$	14	35.11	-0.002		35.11 $\pm$ 0.08	105.11 $\pm$ 3.87	71.37 $\pm$ 2.70
		W1	TF $_{W1}$	12	35.06	0.012		35.07 $\pm$ 0.11	103.38 $\pm$ 5.24	72.56 $\pm$ 3.73
		W1	TF $_{W1c}$	12	35.04	0.022	0.04	35.10 $\pm$ 0.08	104.82 $\pm$ 3.86	71.56 $\pm$ 2.70
		W1	TF $_{W1\mu}$	12	34.98	-0.013	0.11	35.08 $\pm$ 0.10	103.61 $\pm$ 4.77	72.40 $\pm$ 3.39
		W2	TF $_{W2}$	12	35.08	0.012		35.09 $\pm$ 0.12	104.33 $\pm$ 5.77	71.90 $\pm$ 4.02
		W2	TF $_{W2c}$	12	35.04	0.004	0.06	35.10 $\pm$ 0.08	104.91 $\pm$ 3.86	71.50 $\pm$ 2.70
		W2	TF $_{W2\mu}$	12	34.95	-0.020	0.17	35.10 $\pm$ 0.10	104.69 $\pm$ 4.82	71.65 $\pm$ 3.35
Abell 2634/66	8954 $\pm$ 98	W1	TF $_{W1}$	22	35.22	-0.004		35.22 $\pm$ 0.08	110.48 $\pm$ 4.07	81.41 $\pm$ 3.10
		W1	TF $_{W1\mu}$	22	35.17	-0.037	0.11	35.24 $\pm$ 0.06	111.86 $\pm$ 3.09	80.41 $\pm$ 2.35
		W2	TF $_{W2}$	22	35.14	0.002		35.14 $\pm$ 0.09	106.77 $\pm$ 4.43	84.24 $\pm$ 3.59
		W2	TF $_{W2\mu}$	22	35.07	-0.053	0.17	35.19 $\pm$ 0.07	108.97 $\pm$ 3.51	82.54 $\pm$ 2.78
Abell 2151 (Hercules)	11353 $\pm$ 121	u	TF $_u$	29	35.45	0.061		35.51 $\pm$ 0.08	126.53 $\pm$ 4.66	70.77 $\pm$ 2.72
		u	TF $_{uc1}$	29	35.33	0.032		35.36 $\pm$ 0.06	118.13 $\pm$ 3.26	75.80 $\pm$ 2.25
		u	TF $_{uc2}$	26	35.36	0.036		35.40 $\pm$ 0.07	120.01 $\pm$ 3.87	74.61 $\pm$ 2.54
		g	TF $_g$	29	35.34	0.033		35.37 $\pm$ 0.07	118.75 $\pm$ 3.83	75.40 $\pm$ 2.57
		g	TF $_{gc1}$	29	35.33	0.052		35.38 $\pm$ 0.06	119.24 $\pm$ 3.29	75.09 $\pm$ 2.23
		g	TF $_{gc2}$	26	35.34	0.051		35.39 $\pm$ 0.06	119.72 $\pm$ 3.31	74.79 $\pm$ 2.22
		r	TF $_r$	29	35.31	0.031		35.34 $\pm$ 0.06	117.02 $\pm$ 3.23	76.52 $\pm$ 2.27
		r	TF $_{rc}$	26	35.31	0.011		35.32 $\pm$ 0.06	115.95 $\pm$ 3.20	77.22 $\pm$ 2.30
		r	TF $_{r\mu}$	29	35.29	0.018		35.31 $\pm$ 0.06	115.23 $\pm$ 3.18	77.71 $\pm$ 2.31
		i	TF $_i$	29	35.26	0.030		35.29 $\pm$ 0.06	114.27 $\pm$ 3.16	78.36 $\pm$ 2.33
		i	TF $_{ic}$	26	35.26	0.036		35.30 $\pm$ 0.06	114.62 $\pm$ 3.17	78.12 $\pm$ 2.32
		i	TF $_{i\mu}$	29	35.24	0.031		35.27 $\pm$ 0.06	113.29 $\pm$ 3.13	79.04 $\pm$ 2.35
		z	TF $_z$	29	35.24	0.027		35.27 $\pm$ 0.06	113.08 $\pm$ 3.12	79.19 $\pm$ 2.35
		z	TF $_{zc}$	26	35.23	0.007		35.24 $\pm$ 0.06	111.53 $\pm$ 3.08	80.29 $\pm$ 2.39
		z	TF $_{z\mu}$	29	35.23	-0.002		35.23 $\pm$ 0.06	111.06 $\pm$ 3.07	80.63 $\pm$ 2.40
		W1	TF $_{W1}$	26	35.28	0.011		35.29 $\pm$ 0.08	114.34 $\pm$ 4.21	78.31 $\pm$ 3.01
		W1	TF $_{W1c}$	26	35.21	0.027	0.04	35.28 $\pm$ 0.06	113.62 $\pm$ 3.14	78.81 $\pm$ 2.34
		W1	TF $_{W1\mu}$	26	35.13	-0.017	0.11	35.22 $\pm$ 0.07	110.82 $\pm$ 3.57	80.80 $\pm$ 2.75
		W2	TF $_{W2}$	26	35.27	0.013		35.28 $\pm$ 0.09	113.92 $\pm$ 4.72	78.60 $\pm$ 3.37
		W2	TF $_{W2c}$	26	35.21	0.006	0.06	35.28 $\pm$ 0.06	113.53 $\pm$ 3.14	78.87 $\pm$ 2.34
		W2	TF $_{W2\mu}$	26	35.07	-0.027	0.17	35.21 $\pm$ 0.08	110.33 $\pm$ 4.06	81.16 $\pm$ 3.12

Table 10 continued

**Table 10** (*continued*)

Cluster (1)	$V_{mod}$ km s $^{-1}$ (2)	TFR Band (3)	TFR Model (4)	Ngal (5)	$DM_o$ mag (6)	Bias mag (7)	$\Delta DM$ mag (8)	$DM_c$ mag (9)	D Mpc (10)	$V_{mod}/D$ km s $^{-1}$ Mpc $^{-1}$ (11)
		i	TF $_i$	39	35.91	0.028		35.94 $\pm$ 0.06	154.04 $\pm$ 4.26	73.70 $\pm$ 2.18
		i	TF $_{ic}$	33	35.89	0.033		35.92 $\pm$ 0.07	153.00 $\pm$ 4.93	74.20 $\pm$ 2.52
		i	TF $_{i\mu}$	39	35.87	0.029		35.90 $\pm$ 0.06	151.28 $\pm$ 4.18	75.05 $\pm$ 2.22
		z	TF $_z$	39	35.95	0.025		35.97 $\pm$ 0.06	156.67 $\pm$ 4.33	72.47 $\pm$ 2.15
		z	TF $_{zc}$	33	35.92	0.006		35.93 $\pm$ 0.07	153.20 $\pm$ 4.94	74.11 $\pm$ 2.52
		z	TF $_{z\mu}$	39	35.90	-0.002		35.90 $\pm$ 0.06	151.23 $\pm$ 4.18	75.07 $\pm$ 2.22
		W1	TF $_{W1}$	33	36.04	0.011		36.05 $\pm$ 0.09	162.28 $\pm$ 6.73	69.96 $\pm$ 2.99
		W1	TF $_{W1c}$	33	35.85	0.025	0.04	35.91 $\pm$ 0.07	152.40 $\pm$ 4.91	74.49 $\pm$ 2.53
		W1	TF $_{W1\mu}$	33	35.88	-0.016	0.11	35.97 $\pm$ 0.08	156.59 $\pm$ 5.77	72.50 $\pm$ 2.78
		W2	TF $_{W2}$	33	36.04	0.013		36.05 $\pm$ 0.09	162.40 $\pm$ 6.73	69.91 $\pm$ 2.99
		W2	TF $_{W2c}$	33	35.85	0.005	0.06	35.92 $\pm$ 0.07	152.42 $\pm$ 4.91	74.49 $\pm$ 2.53
		W2	TF $_{W2\mu}$	33	35.82	-0.027	0.17	35.96 $\pm$ 0.08	155.83 $\pm$ 5.74	72.85 $\pm$ 2.79

## REFERENCES

Aaronson, M., Bothun, G., Mould, J., et al. 1986, ApJ, 302, 536, doi: [10.1086/164014](https://doi.org/10.1086/164014)

Aaronson, M., Huchra, J., & Mould, J. 1979, ApJ, 229, 1, doi: [10.1086/156923](https://doi.org/10.1086/156923)

Alam, S., Albareti, F. D., Allende Prieto, C., et al. 2015, ApJS, 219, 12, doi: [10.1088/0067-0049/219/1/12](https://doi.org/10.1088/0067-0049/219/1/12)

Beers, T. C., Flynn, K., & Gebhardt, K. 1990, AJ, 100, 32, doi: [10.1086/115487](https://doi.org/10.1086/115487)

Bhardwaj, A., Kanbur, S. M., Macri, L. M., et al. 2016, AJ, 151, 88, doi: [10.3847/0004-6256/151/4/88](https://doi.org/10.3847/0004-6256/151/4/88)

Courtois, H. M., Tully, R. B., Fisher, J. R., et al. 2009, AJ, 138, 1938, doi: [10.1088/0004-6256/138/6/1938](https://doi.org/10.1088/0004-6256/138/6/1938)

Courtois, H. M., Tully, R. B., Makarov, D. I., et al. 2011, MNRAS, 414, 2005, doi: [10.1111/j.1365-2966.2011.18515.x](https://doi.org/10.1111/j.1365-2966.2011.18515.x)

Djorgovski, S., & Davis, M. 1987, ApJ, 313, 59, doi: [10.1086/164948](https://doi.org/10.1086/164948)

Dressler, A., Lynden-Bell, D., Burstein, D., et al. 1987, ApJ, 313, 42, doi: [10.1086/164947](https://doi.org/10.1086/164947)

Du, W., Cheng, C., Zheng, Z., & Wu, H. 2020, AJ, 159, 138, doi: [10.3847/1538-3881/ab6efb](https://doi.org/10.3847/1538-3881/ab6efb)

Fisher, J. R., & Tully, R. B. 1981, ApJS, 47, 139, doi: [10.1086/190755](https://doi.org/10.1086/190755)

Freedman, W. L., Madore, B. F., Gibson, B. K., et al. 2001, ApJ, 553, 47, doi: [10.1086/320638](https://doi.org/10.1086/320638)

Freedman, W. L., Madore, B. F., Hatt, D., et al. 2019, ApJ, 882, 34, doi: [10.3847/1538-4357/ab2f73](https://doi.org/10.3847/1538-4357/ab2f73)

Gieren, W., Górski, M., Pietrzyński, G., et al. 2013, ApJ, 773, 69, doi: [10.1088/0004-637X/773/1/69](https://doi.org/10.1088/0004-637X/773/1/69)

Giovanelli, R., Haynes, M. P., Herter, T., et al. 1997, AJ, 113, 53, doi: [10.1086/118234](https://doi.org/10.1086/118234)

Haynes, M. P., Giovanelli, R., Martin, A. M., et al. 2011, AJ, 142, 170, doi: [10.1088/0004-6256/142/5/170](https://doi.org/10.1088/0004-6256/142/5/170)

Haynes, M. P., Giovanelli, R., Kent, B. R., et al. 2018, ApJ, 861, 49, doi: [10.3847/1538-4357/aac956](https://doi.org/10.3847/1538-4357/aac956)

Huchra, J. P., Macri, L. M., Masters, K. L., et al. 2012, ApJS, 199, 26, doi: [10.1088/0067-0049/199/2/26](https://doi.org/10.1088/0067-0049/199/2/26)

Huchtmeier, W. K., & Richter, O. G. 1989, A General Catalog of HI Observations of Galaxies. The Reference Catalog.

Humphreys, E. M. L., Reid, M. J., Moran, J. M., Greenhill, L. J., & Argon, A. L. 2013, ApJ, 775, 13, doi: [10.1088/0004-637X/775/1/13](https://doi.org/10.1088/0004-637X/775/1/13)

Jacobs, B. A., Rizzi, L., Tully, R. B., et al. 2009, AJ, 138, 332, doi: [10.1088/0004-6256/138/2/332](https://doi.org/10.1088/0004-6256/138/2/332)

Jang, I. S., & Lee, M. G. 2015, ApJ, 807, 133, doi: [10.1088/0004-637X/807/2/133](https://doi.org/10.1088/0004-637X/807/2/133)

—. 2017, *ApJ*, 836, 74,  
doi: [10.3847/1538-4357/836/1/74](https://doi.org/10.3847/1538-4357/836/1/74)

Kourkchi, E., & Tully, R. B. 2017, *ApJ*, 843, 16,  
doi: [10.3847/1538-4357/aa76db](https://doi.org/10.3847/1538-4357/aa76db)

Kourkchi, E., Tully, R. B., Neill, J. D., et al. 2019,  
*ApJ*, 884, 82, doi: [10.3847/1538-4357/ab4192](https://doi.org/10.3847/1538-4357/ab4192)

Leavitt, H. S., & Pickering, E. C. 1912, *Harvard College Observatory Circular*, 173, 1

Lee, M. G., Freedman, W. L., & Madore, B. F. 1993, *ApJ*, 417, 553, doi: [10.1086/173334](https://doi.org/10.1086/173334)

Lelli, F., McGaugh, S. S., & Schombert, J. M. 2016, *ApJL*, 816, L14,  
doi: [10.3847/2041-8205/816/1/L14](https://doi.org/10.3847/2041-8205/816/1/L14)

Lelli, F., McGaugh, S. S., Schombert, J. M., Desmond, H., & Katz, H. 2019, *MNRAS*, 484, 3267, doi: [10.1093/mnras/stz205](https://doi.org/10.1093/mnras/stz205)

Magoulas, C., Springob, C. M., Colless, M., et al. 2012, *MNRAS*, 427, 245,  
doi: [10.1111/j.1365-2966.2012.21421.x](https://doi.org/10.1111/j.1365-2966.2012.21421.x)

Makarov, D., Prugniel, P., Terekhova, N., Courtois, H., & Vauglin, I. 2014, *A&A*, 570, A13, doi: [10.1051/0004-6361/201423496](https://doi.org/10.1051/0004-6361/201423496)

Makarov, D. I., Zaitseva, N. A., & Bizyaev, D. V. 2018, *MNRAS*, 479, 3373,  
doi: [10.1093/mnras/sty1629](https://doi.org/10.1093/mnras/sty1629)

Masters, K. L., Springob, C. M., Haynes, M. P., & Giovanelli, R. 2006, *ApJ*, 653, 861,  
doi: [10.1086/508924](https://doi.org/10.1086/508924)

McGaugh, S. S. 2005, *ApJ*, 632, 859,  
doi: [10.1086/432968](https://doi.org/10.1086/432968)

McGaugh, S. S., Schombert, J. M., Bothun, G. D., & de Blok, W. J. G. 2000, *ApJL*, 533, L99,  
doi: [10.1086/312628](https://doi.org/10.1086/312628)

Monson, A. J., Freedman, W. L., Madore, B. F., et al. 2012, *ApJ*, 759, 146,  
doi: [10.1088/0004-637X/759/2/146](https://doi.org/10.1088/0004-637X/759/2/146)

Neill, J. D., Seibert, M., Tully, R. B., et al. 2014,  
*ApJ*, 792, 129,  
doi: [10.1088/0004-637X/792/2/129](https://doi.org/10.1088/0004-637X/792/2/129)

Noordermeer, E., & Verheijen, M. A. W. 2007,  
*MNRAS*, 381, 1463,  
doi: [10.1111/j.1365-2966.2007.12369.x](https://doi.org/10.1111/j.1365-2966.2007.12369.x)

Phillips, M. M. 1993, *ApJL*, 413, L105,  
doi: [10.1086/186970](https://doi.org/10.1086/186970)

Pietrzyński, G., Graczyk, D., Gallenne, A., et al. 2019, *Nature*, 567, 200,  
doi: [10.1038/s41586-019-0999-4](https://doi.org/10.1038/s41586-019-0999-4)

Planck Collaboration, Aghanim, N., Akrami, Y., et al. 2018, arXiv e-prints.  
<https://arxiv.org/abs/1807.06209>

Ponomareva, A. A., Verheijen, M. A. W., & Bosma, A. 2016, *MNRAS*, 463, 4052,  
doi: [10.1093/mnras/stw2213](https://doi.org/10.1093/mnras/stw2213)

Ponomareva, A. A., Verheijen, M. A. W., Peletier, R. F., & Bosma, A. 2017, *MNRAS*, 469, 2387,  
doi: [10.1093/mnras/stx1018](https://doi.org/10.1093/mnras/stx1018)

Querejeta, M., Meidt, S. E., Schinnerer, E., et al. 2015, *ApJS*, 219, 5,  
doi: [10.1088/0067-0049/219/1/5](https://doi.org/10.1088/0067-0049/219/1/5)

Riess, A. G., Casertano, S., Yuan, W., Macri, L. M., & Scolnic, D. 2019, *ApJ*, 876, 85,  
doi: [10.3847/1538-4357/ab1422](https://doi.org/10.3847/1538-4357/ab1422)

Riess, A. G., Macri, L. M., Hoffmann, S. L., et al. 2016, *ApJ*, 826, 56,  
doi: [10.3847/0004-637X/826/1/56](https://doi.org/10.3847/0004-637X/826/1/56)

Rizzi, L., Tully, R. B., Makarov, D., et al. 2007,  
*ApJ*, 661, 815, doi: [10.1086/516566](https://doi.org/10.1086/516566)

Rubin, V. C., Burstein, D., Ford, W. K., J., & Thonnard, N. 1985, *ApJ*, 289, 81,  
doi: [10.1086/162866](https://doi.org/10.1086/162866)

Sakai, S., Mould, J. R., Hughes, S. M. G., et al. 2000, *ApJ*, 529, 698, doi: [10.1086/308305](https://doi.org/10.1086/308305)

Schechter, P. 1976, *ApJ*, 203, 297

Schechter, P. L. 1980, *AJ*, 85, 801,  
doi: [10.1086/112742](https://doi.org/10.1086/112742)

Scowcroft, V., Freedman, W. L., Madore, B. F., et al. 2011, *ApJ*, 743, 76,  
doi: [10.1088/0004-637X/743/1/76](https://doi.org/10.1088/0004-637X/743/1/76)

Sorce, J. G., Courtois, H. M., Tully, R. B., et al. 2013, *ApJ*, 765, 94,  
doi: [10.1088/0004-637X/765/2/94](https://doi.org/10.1088/0004-637X/765/2/94)

Springob, C. M., Haynes, M. P., Giovanelli, R., & Kent, B. R. 2005, *ApJS*, 160, 149,  
doi: [10.1086/431550](https://doi.org/10.1086/431550)

Springob, C. M., Masters, K. L., Haynes, M. P., Giovanelli, R., & Marinoni, C. 2007, *ApJS*, 172, 599, doi: [10.1086/519527](https://doi.org/10.1086/519527)

Springob, C. M., Magoulas, C., Colless, M., et al. 2014, *MNRAS*, 445, 2677,  
doi: [10.1093/mnras/stu1743](https://doi.org/10.1093/mnras/stu1743)

Tonry, J., & Schneider, D. P. 1988, *AJ*, 96, 807,  
doi: [10.1086/114847](https://doi.org/10.1086/114847)

Tully, R. B. 1988, *Nature*, 334, 209,  
doi: [10.1038/334209a0](https://doi.org/10.1038/334209a0)

—. 2015, *AJ*, 149, 171,  
doi: [10.1088/0004-6256/149/5/171](https://doi.org/10.1088/0004-6256/149/5/171)

Tully, R. B., & Courtois, H. M. 2012, *ApJ*, 749, 78, doi: [10.1088/0004-637X/749/1/78](https://doi.org/10.1088/0004-637X/749/1/78)

Tully, R. B., Courtois, H. M., & Sorce, J. G. 2016,  
*AJ*, 152, 50, doi: [10.3847/0004-6256/152/2/50](https://doi.org/10.3847/0004-6256/152/2/50)

Tully, R. B., & Fisher, J. R. 1977, A&A, 54, 661

Tully, R. B., Mould, J. R., & Aaronson, M. 1982, ApJ, 257, 527, doi: [10.1086/160009](https://doi.org/10.1086/160009)

Tully, R. B., & Pierce, M. J. 2000, ApJ, 533, 744, doi: [10.1086/308700](https://doi.org/10.1086/308700)

Tully, R. B., Shaya, E. J., Karachentsev, I. D., et al. 2008, ApJ, 676, 184, doi: [10.1086/527428](https://doi.org/10.1086/527428)

Tully, R. B., Verheijen, M. A. W., Pierce, M. J., Huang, J.-S., & Wainscoat, R. J. 1996, AJ, 112, 2471, doi: [10.1086/118196](https://doi.org/10.1086/118196)

Tully, R. B., Courtois, H. M., Dolphin, A. E., et al. 2013, AJ, 146, 86, doi: [10.1088/0004-6256/146/4/86](https://doi.org/10.1088/0004-6256/146/4/86)

Ulaczyk, K., Szymański, M. K., Udalski, A., et al. 2012, AcA, 62, 247. <https://arxiv.org/abs/1210.4702>

Verheijen, M. A. W. 2001, ApJ, 563, 694, doi: [10.1086/323887](https://doi.org/10.1086/323887)

Willlick, J. A. 1994, ApJS, 92, 1, doi: [10.1086/191957](https://doi.org/10.1086/191957)

Willlick, J. A., Courteau, S., Faber, S. M., et al. 1996, ApJ, 457, 460, doi: [10.1086/176746](https://doi.org/10.1086/176746)

Wright, E. L., Eisenhardt, P. R. M., Mainzer, A. K., et al. 2010, AJ, 140, 1868, doi: [10.1088/0004-6256/140/6/1868](https://doi.org/10.1088/0004-6256/140/6/1868)

Yuan, W., Riess, A. G., Macri, L. M., Casertano, S., & Scolnic, D. M. 2019, ApJ, 886, 61, doi: [10.3847/1538-4357/ab4bc9](https://doi.org/10.3847/1538-4357/ab4bc9)

Zgirski, B., Gieren, W., Pietrzynski, G., et al. 2017, ApJ, 847, 88, doi: [10.3847/1538-4357/aa88c4](https://doi.org/10.3847/1538-4357/aa88c4)